UNIVERSITE PARIS VII - DENIS DIDEROT
UFR de Physique

MEMOIRE

pour l'obtention de

L'HABILITATION A DIRIGER DES RECHERCHES

présentée par

Frédéric Déliot

Towards the Top with DØ

soutenue le 22 juin 2012 devant le jury composé de

Mme	M.	Bosman	
M.	T.	Liss	(rapporteur)
M.	M.	Mangano	(rapporteur)
M.	Ph.	Schwemling	(rapporteur)
M.	R.	Tenchini	
M.	D.	Vilanova	
M.	T.	Wyatt	

Frédéric DELIOT
Date of birth : 21 July 1973
Place of birth : Besançon, France

Education :

1999-2002 : PhD in experimental particle physics, CEA-Saclay, France
Muon Reconstruction and Identification in the DØ experiment, Study of Resonant Production of Sleptons at Tevatron
1997-1998 : D.E.A. *Champs, Particules, Matière*, University Paris 7
1996-1997 : 3rd year study at the Technische Universität Berlin
1994-1997 : Ecole Nationale Supérieure des Mines (Saint-Etienne)
1991-1994 : Preparatory classes to the "Grandes Ecoles"
1991 : High School Diploma (very good with congratulations)

Employment :

2003 : 1 year stay as research scientist at Fermilab (DØ experiment)
Since 2002 : Physicist at the Commissariat à l'Energie Atomique (CEA-Saclay) in the particle physics division (IRFU/SPP) - permanent position
1998-1999 : Military service as scientist at the detector, electronic and computing division (SEDI) of CEA-Saclay, *Study of ionization-heat bolometers for the EDELWEISS experiment*

Responsibilities within the DØ Collaboration :

Since 2011 : Representative in the Tevatron top combination group
2008-2011 : Convener of the DØ top quark physics group
2008 : Member of the review committee for the analyses searching for high mass Higgs boson at DØ
Since 2007 : Member of the DØ authorship committee
2007-2008 : Convener of the DØ dilepton top quark subgroup
2006 : Member of the DØ spokesperson election committee
2003-2005 : Convener of the DØ common sample group
2002-2003 : Convener of the DØ muon reconstruction and identification group

Supervision and Teaching Experience :

Since 2005 : Supervisor of 4 PhD students :

- Marion Arthaud : *Measurement of the top-quark mass in the electron-muon channel with the D0 detector at the Tevatron*, FERMILAB-THESIS-2008-73 (2008)
- Solène Théry : *Measurement of cross section of quark pair production top with the D0 experiment at the Tevatron and determination the top quark mass using this measure*, FERMILAB-THESIS-2010-26 (2010)
- Cécile Deterre : *Measurement of the top quark properties in the the dilepton channel*

with the D0 and ATLAS detectors, CERN-THESIS-2012-103 (2012)

- Antoine Chapelain : *Measurement of the top quark properties in the the dilepton channel with the D0 and ATLAS detectors*, in progress

2011 : Lecturer in the 3rd French-Asian Particle Physics School, October 9-21, 2011, Les Houches, France
2005-2008 : Lecturer in the Master : "Nuclei, Particles, Astroparticles and Cosmology" (M2-NPAC), Universities Paris VI, VII, IX, and CEA in charge of the lecture on "Particles and Symmetries"
2004 : Supervision of the laboratory work of the Master "Nuclei, Particles, Astroparticle and Cosmology"
2003 : Lecturer at the French Young Scientist Forum organized by the French Physics Society

Other Responsibilities :

2011 : Member of the advisory committee of the 4th International Workshop on Top Quark Physics, Top2011, September 25-30, 2011 in Spain
2011 : referee for Physics Letters B.
2011 : Editor of the $t\bar{t}$ charge asymmetry ATLAS conference note and paper
Since 2009 : Elected member of the scientific committee of the particle physics division at CEA
2010 : referee for the ANR (National Research Agency)
2005 : Convener of the session "Tests of Standard Model" at the HEP2005 Conference in Lisbon
2005 : Coordinator of the "Standard Model and beyond" at the Young Scientist Forum organized by the French Physics Society
2004 : Co-organizer of an exhibition on accelerator and particle physics at the Paris scientific museum (Palais de la découverte)

Publications :

I have co-authored about 260 papers in high impact peer reviewed journals mainly as member of the DØ experiment. Apart from these publications, I wrote 50 DØ internal notes.
I have listed below selected publications that best summarize my research work and in particular the publications which I signed without the full DØ collaboration.
The full list of my publications can be find at :

`http://inspirebeta.net/search?ln=fr&p=find+a+deliot+&action_search=Recherche`

1. F. Déliot and D. Glenzinski, *Top Quark Physics at the Tevatron*
   arXiv :1010.1202, accepted by Rev. Mod. Phys.
2. The D0 Collaboration, V.M. Abazov et al., *Precise measurement of the top quark mass in the dilepton channel at D0*
   Phys. Rev. Lett. 107, 082004 (2011)
3. The D0 Collaboration, V.M. Abazov et al., *Determination of the pole and* $\overline{\mathrm{MS}}$ *mass values of the top quark from the inclusive ttbar production cross section*
   Phys. Lett. **B 703**, 422 (2011)
4. The D0 Collaboration, V.M. Abazov et al., *Measurement of the* $t\bar{t}$ *production cross section using dilepton events in* $p\overline{p}$ *collisions*
   Phys. Lett. **B704**, 403 (2011)
5. The D0 Collaboration, V.M. Abazov et al., *Precision Measurement of the Ratio* $B(t \to Wb)/B(t \to Wq)$ *and Extraction of* V_{tb}
   Phys. Rev. Lett. 107, 121802 (2011)
6. The Tevatron Electroweak Working Group and CDF Collaboration and D0 Collaboration, *Combination of CDF and D0 results on the mass of the top quark using up to 5.8* fb^{-1} *of data*
   FERMILAB-TM-2504-E, arXiv :1107.5255
7. The D0 Collaboration, V.M. Abazov et al., *Measurement of the t anti-t production cross section and top quark mass extraction using dilepton events in p anti-p collisions*
   Phys. Lett. **B679**, 177 (2009)
8. The D0 Collaboration, V.M. Abazov et al., *Measurement of the t anti-t production cross-section in p anti-p collisions using dilepton events, the D0 Collaboration*
   Phys. Rev. **D76**, 052006 (2007)
9. F. Déliot, G. Moreau, C. Royon, *Single superpartner production at Tevatron Run II*
   Eur. Phys. J. **C19**, 155 (2001)
10. G. Moreau, M. Chemtob, F. Déliot, C. Royon, E. Perez *Resonant sneutrino production at Tevatron Run II*
    Phys. Lett. **B475**, 184 (2000)
11. X.F. Navick, M. Chapellier, F. Déliot, S. Hervé, L. Miramonti *320-g ionization-heat bolometers design for the EDELWEISS experiment*
    Nucl. Instrum. Meth. **A444**, 361 (2000)

Invited presentations :

I have listed below the talks that I gave on behalf of the Tevatron or LHC collaborations. In addition I gave about 100 presentations within the DØ or ATLAS collaborations.

2012 : *Tevatron and LHC top-quark mass combinations*
Presented at the 36th International Conference on High Energy Physics,
Melbourne, 4-11 July 2012.

2011 : *$t\bar{t}$ Charge Asymmetry at Hadron Colliders*
seminar talk at Bergische Universität Wuppertal, December 2011.

2011 : *Top Quark Physics*
Frédéric Déliot for the CDF, DØ, ATLAS and CMS collaborations,
Plenary talk presented at the EPS-HEPP Conference in Grenoble, France, July 21-27, 2011.

2010 : *$t\bar{t}$ Cross Section Measurements at Tevatron*
Frédéric Déliot for the CDF and DØ collaborations,
Presented at 3rd International Workshop on Top Quark Physics, May 31- June 4 2010.

2008 : *Top Quark Cross Sections*
Frédéric Déliot for the CDF and DØ collaborations,
Presented at 28th Physics in Collision (PIC 2008), Perugia, Italy, 25-28 June 2008.

2008 : *Top Results from Tevatron*
Presented at Physics CMS-France, 18-19 March 2008.

2007 : several seminar talks on top quark physics at Tevatron
CEA-Saclay, LAL-Orsay, LPNHE-Paris

2005 : *Electroweak measurements at Tevatron*
Frédéric Déliot for the CDF and DØ collaborations,
Presented at 40th Rencontres de Moriond on Electroweak Interactions and Unified Theories,
La Thuile, Aosta Valley,Italy, 5-12 March 2005.

2003 : *Latest DØ Results for DPF*
Frédéric Déliot for the DØ collaboration,
Fermilab Wine and Cheese Seminar, 11 April 2003.

2001 : *Search for R-parity violation at DØ*
Frédéric Déliot for the DØ collaboration,
Presented at 9th International Conference on Supersymmetry and Unification of Fundamental Interactions (SUSY01), Dubna, Russia, 11-17 June 2001.

Summary of my scientific path and perspectives :

I started my career in high-energy physics in 1998 in the division for detector development of the Commissariat à l'Energie Atomique (CEA) during my military service in Saclay working on a new type of ionization-heat bolometers for the EDELWEISS experiment.
I carried out my PhD studies at CEA-Saclay under the supervision of Claude Guyot within the DØ collaboration starting in 1999. DØ is an international high-energy physics experiment gathering 600 physicists at the Tevatron accelator in Fermilab near Chicago. I took over the responsiblity for the development of the last steps of the muon reconstruction software and implemented the pattern recognition algorithm associating the muon hits, fitting the muon tracks as well as further matching these muon tracks with the tracks of the central tracker. This pattern recognition turned out to be challenging due to the difficult environment of the muon spectrometer and calorimeter taking into account multiple scattering and the inhomogeneous magnetic field in the detector. This software program is still used to reconstruct muons for all the DØ analyses. I used this algorithm to reconstruct the first J/ψ signal at the beginning of the DØ Run II data taking in 2001.
During my PhD, I also studied the possibility to observe a specific New Physics signature at the Tevatron. I examined for the first time at the Tevatron the possible resonant production of R-parity violating supersymmetric particles. This work was performed in association with theoreticians and published in 2000 and 2001.
In 2002, I was hired at CEA-Saclay and spent one year at Fermilab where I became co-convener of the muon reconstruction and identification group. I developed new muon identification criteria that allowed to increase the muon selection efficiency.
In 2003, I became co-convener of the newly formed group responsible for the definitions and preparation of common data and MC samples for all the physics analyses in the collaboration. This group at the interface of the different physics groups was created to increase the collaboration productivity by centralizing the standard object definitions to be used in the analyses and by producing common data skimmed samples as well as common MC. At that time using my expertise in muon reconstruction, I also worked, together with colleagues from Saclay and Manchester, on the measurement of the W boson production cross section in the muon channel which was a good test of the Standard Model still at an early state of the experiment.
In 2004, using my expertise in muon reconstruction and common software and samples, I switched to top quark physics taking the opportunity that the analysis of one important top quark decay channel was becoming uncovered (the electron-muon channel). Together with three students under my supervision and with some of my Saclay colleagues, we carried out the measurement of the top-antitop cross section in the dilepton channel as well as the mass measurement in the same channel both with an unprecedented precision at that time allowing for further important tests of the Standard Model in the top quark sector. In 2005, I became convener of the top dilepton subgroup in DØ.
In 2007 and since 2011, I was appointed co-convener of the whole DØ top group. Hence I was responsible for managing the DØ top group, in particular to review the top quark analyses before publication and to interact with the other high-energy experiments performing top quark measurements as well as with theoreticians working in the field. Since 2007, the DØ top group has published in average 10 papers per year in scientific journals, which include

the observation of top quark electroweak production and the measurement of the $t\bar{t}$ forward-backward asymmetry.
Since 2009, I am responsible for the combination of DØ and CDF top-quark mass measurements to produce the official world average value updated every year. In 2008 together with theoreticians and DØ colleagues, we also developed a new technique to extract the top quark mass from the top production cross section by combining theoretical and experimental inputs.
Since late 2010, I have joined the ATLAS collaboration in order to continue to study the top quark properties at the world highest energy collider, the LHC at CERN near Geneva. I first worked on the top quark mass extraction from the $t\bar{t}$ cross section using ATLAS measurement in the lepton+jets channel with 35 pb^{-1}. Since spring 2011, I am co-editor for the public conference note and the journal publication that describes the ATLAS measurement of the $t\bar{t}$ charge asymmetry in the lepton+jets channel.

In the years to come, I would like to participate to the analysis of the full Tevatron dataset of 10 fb^{-1} and in particular to work on some of the top quark legacy measurements of the Tevatron (measurements of the top quark mass and $t\bar{t}$ forward-backward asymmetry both in the dilepton channel). I also plan to participate in the measurement of the $t\bar{t}$ charge asymmetry with the full 2012 ATLAS dataset in order to give a final statement about the current Tevatron anomaly.

Table of contents

Introduction **11**

1 Muon Identification and Common Analysis Tools at DØ **13**
1.1 Muon Identification at DØ . . . 14
1.1.1 Muon Reconstruction Overview . . . 14
1.1.2 Muon Identification . . . 15
1.1.3 Muon Efficiency Measurement and Muon Certification . . . 20
1.1.4 Muon Momentum Oversmearing . . . 23
1.2 Common Analysis Tools . . . 24
1.2.1 Overview of the DØ data processing chain . . . 25
1.2.2 Common analysis format : CAF . . . 26
1.2.3 Common corrections on reconstructed objects . . . 26
1.3 Conclusion . . . 27

2 Measurement of the inclusive production of W boson into muon at DØ **29**
2.1 Physics Motivations . . . 30
2.2 Data Samples and Selection of the $W \to \mu\nu$ Events . . . 31
2.3 Efficiency Computation and Fast Simulation . . . 33
2.3.1 Trigger, Muon and Tracking Efficiency . . . 33
2.3.2 Isolation Efficiency . . . 36
2.3.3 Fast Simulation . . . 37
2.4 Background Estimation . . . 38
2.5 Results . . . 40
2.6 Conclusion . . . 43

3 A Partial Top View **45**
3.1 Top Quark Physics Using $t\bar{t}$ Events . . . 46
3.1.1 Introduction to Top Quark Physics at the Tevatron . . . 46
3.1.2 $t\bar{t}$ Event Selection Criteria . . . 48
3.1.3 Background Processes . . . 48
3.1.4 Sources of Systematic Uncertainty . . . 49
3.2 Top Quark as Window to New Physics . . . 52
3.3 $t\bar{t}$ Production Cross Section . . . 53
3.3.1 Theoretical Computations . . . 53
3.3.2 $t\bar{t}$ Cross Section Measurements in the Dilepton Channel . . . 54

3.3.3 $t\bar{t}$ Cross Section Combination 65
3.3.4 Ratio of $t\bar{t}$ Cross Sections 66
3.4 Some Top Quark Properties 69
3.4.1 Top Quark Mass 69
3.4.2 $t\bar{t}$ Charge Asymmetry 86
3.5 Conclusion and Perspectives 92

Conclusion **95**

Introduction

The top quark was the last quark discovered in 1995 by the CDF and DØ experiments at the Fermilab Tevatron and it happens to have a surprisingly large mass. It is the weak-isospin partner to the bottom quark, and both the top and the bottom quarks constitute the third generation of quarks. All the known elementary particles and their interactions are described by the so-called Standard Model of particle physics. The Standard Model has been extensively tested over the past decades at colliders without any hints indicating deviations from its predictions. However we know that the Standard Model is not the ultimate theory as some fundamental questions remain unanswered. Among these questions lies the origin of the particle masses or why there are exactly three generations of quarks and leptons. The precise mechanism that gives the mass of the particles supposedly through the Higgs mechanism has also to be confirmed and understood. So the Standard Model has several shortcomings and is widely regarded to be a low energy approximation of a more complete description of particle physics. There are numerous hypothesized theories beyond the Standard Model called new physics models that address these shortcomings and offer a more complete description. The search for a discovery and a description of the physics that breaks electroweak symmetry is among the most ardently pursued one by high-energy physicists.

Due to its large mass, the top quark Yukawa coupling to the Higgs boson is of order unity. So the top quark strongly couples to the dynamics of electroweak symmetry breaking and is thus expected to be a unique place to test this dynamics and probe for new physics effects. In addition, because of its large mass, quantum loop corrections to top quark observables from possible new particle contributions can be large - significantly larger than for the lighter quarks and leptons. For all these reasons, the top quark is a special quark and top quark physics is a promising field to search for new physics. After having been pioneered at the Tevatron experiments during the past 15 years, the LHC is now taking over the leading role in the top quark study.

The plan of this manuscript follows my research path over the past 10 years : the muon identification and common analysis tools at DØ, the measurement of the inclusive production of W boson decaying into muon and top quark studies.

In the first section, I describe my work about muon identification, certification of the standard muon identification criteria, measurement of the muon selection efficiency and about the development of common analysis format and tools. In the second section, I explain how these efficiency measurements can be used to measure the inclusive W boson production cross section in the muon channel. The $W \to \mu\nu$ cross section measurement can be seen as a standard candle to establish several analysis pieces that have to be put in place to perform more complex measurements like top quark analyses. In the last section I introduce more extensively the top quark physics at the Tevatron and describe in more details the main analyses in the dilepton channel I was involved in : the measurement of the $t\bar{t}$ inclusive cross section in the dilepton channel as well as the ratio of cross sections, the measurement of the top quark mass in the dilepton channel, the extraction of the mass from the $t\bar{t}$ cross section and the Tevatron top quark mass combination. Before concluding, I finish the section with the description of the latest results on the $t\bar{t}$ charge asymmetry both at the Tevatron and at the LHC.

Chapter 1

Muon Identification and Common Analysis Tools at DØ

Contents

1.1 Muon Identification at DØ **14**
1.1.1 Muon Reconstruction Overview 14
1.1.2 Muon Identification 15
1.1.3 Muon Efficiency Measurement and Muon Certification 20
1.1.4 Muon Momentum Oversmearing 23
1.2 Common Analysis Tools **24**
1.2.1 Overview of the DØ data processing chain 25
1.2.2 Common analysis format : CAF 26
1.2.3 Common corrections on reconstructed objects 26
1.3 Conclusion **27**

After my PhD during which I developped the final steps of the DØ muon reconstruction algorithm [1], I have been convener of the DØ muon reconstruction and identification group from 2002 to 2003. During that period, I worked on optimizing the muon identification criteria and the tools for measuring the muon efficiencies. Later on, I worked with my student on the offline smearing of the muon momentum. In the first part of this chapter, after a brief overview of the muon reconstruction algorithms at DØ, I will describe these different activities.

From 2003 to 2005, I was convener of the newly formed DØ common sample group. This group is aiming at centrally producing skimmed data samples for the different analyses, developping a common ROOT based analysis format and centralizing the application of the post-reconstruction corrections on the physics objects. In the second part of this chapter, I will shortly describe some of my activities in this group.

The DØ detector will not be described in this chapter apart from a few lines on the muon spectrometer. Some extensive description of the detector can be found in [1, 2, 3]. As this will be used in this section, we just state here that the DØ central tracker consists of two parts : the vertex detector (Silicon Microstrip Tracker : SMT) and the fiber tracker (Central Fiber Tracker : CFT) both inside the solenoid magnet.

1.1 Muon Identification at DØ

1.1.1 Muon Reconstruction Overview

A brief description of the muon reconstruction is given here. More details can be found in [1, 4].

The muon spectrometer consists of scintillator and drift chambers separated into the central (within approximately $|\eta| < 1$) and forward regions (up to $|\eta| \approx 2$) [5]. Each of these sub-systems has 3 layers labelled A (before the iron toroid) and B and C (after the toroid) more than 1 m away from each other. The toroid provides a magnetic field of 1.8 T.

The first step of the muon recontruction algorithm relies on associating the hits within each layer of the drift chambers. The hits are connected using straight lines called segments within layer A and together within layers B and C since there is no magnetic field between the B and C layers. As the drift time to distance relation in the chambers depends on the muon incident angle, the segment algorithm is iteratively adding the hits that are compatible using a χ^2 fit. The typical position and angle resolutions of the obtained segment is $\sigma(y) \approx 0.7$ mm for all the layers, $\sigma(\theta) \approx 10$ mrad for the A layer and $\sigma(\theta) \approx 0.5$ mrad for the BC layer.

The next step consists of the association of a A segment with a BC segment outside the toroid within the same region (central or forward/backward) and the same or adjacent octant. Uncoupled segments could be used later in the matching procedure with central tracks. Compatible segments are used as input to fit the track parameters (position and angle at the A layer, curvature at the layer A in the bending plane). Since the muon has to go through the iron toroid to reach the B and C layers, multiple scattering has to be taken into account in the fit. The track parameters are fitted using a χ^2 method by propagating the A layer track linearly by small steps taking into account both the magnetic field and the energy loss. The typical resolution on the reconstructed local tracks is : $\sigma(p_T)/p_T = (27 \oplus 0.44\ p_T)\%$ for the central part and $\sigma(p_T)/p_T = (23 \oplus 0.42\ p_T)\%$ for the forward/backward regions.

The typical local reconstruction efficiency for muon with a converged fit is around 80%. The limited local muon momentum resolution is improved by the matching with central tracks as discussed below. Local muon informations are rather used for muon identification than for actual muon momentum measurements. Local momentum measurements however are important to select pure $Z \to \mu\mu$ events for track efficiency measurements as described in section 1.1.3.

The last step of the muon reconstruction aims at matching the local tracks in the spectrometer with a track reconstructed in the DØ central tracking system. This step is based on the propagation of the track parameters and its error matrix through the calorimeter taking into account both the magnetic field, the multiple scattering and the energy loss. If the local fit has converged, the track and error matrix at the A layer is back-propagated through the calorimeter and preshower to the distance of closest approach (dca) where the central tracks are defined. In case of unmatched segments or non-converged local fit, central tracks and error matrices that could be compatible with the muon segments are propagated forward up to the A layer. A χ^2 can then be constructed between the propagated track and errors matrices and either the muon $(P_{\text{muon}}, E_{\text{muon}})$ or the central track $(P_{\text{track}}, E_{\text{track}})$ parameters to evaluate the goodness of the matching : $\chi^2 =^t (P_{\text{muon}} - P_{\text{track}}).(E_{\text{muon}} + E_{\text{track}})^{-1}(P_{\text{muon}} - P_{\text{track}})$. Depending on the analyses, either a tight cut is applied on this χ^2 to select the good matches (typically $\chi^2 < 10$ when using low p_T muons), or a loose cut : $\chi^2 < 10^3$ when using high p_T muons (Higgs, top and electroweak physics).

1.1.2 Muon Identification

In order to simplify the physics analyses and the efficiency computations specific sets of cuts have been established to define standard muon types that can be used in the analyses. These muon types are then called certified muons. Certified muon candidates are classified according to their informations in the muon spectrometer, to the quality of the central track matched to it if any and to its isolation both in the tracker and the calorimeter.

Reconstructed muons are classified using two parameters : muon *type* and muon *quality*. The *type* of muon is given by the parameter *nseg*. A positive value of *nseg* indicates that the muon reconstructed in the muon system ("local muon") was matched to a track in the central tracking system. A negative value of *nseg* tells that the local muon could not be matched to a central track. The absolute value $|nseg| = 1$, 2, or 3 respectively indicates that the local muon is made up of A-layer only hits, B or C-layer only hits, or both A- and B- or C-layers hits. The different muon types with their respective values of *nseg* are listed in Table 1.1.

The second parameter used to classify muons is the *quality*. The muon quality can be "Loose", "Medium" or "Tight". Part of my work during my convenorship was to optimize this quality definition by loosening the requirements on the local muon in regions with reduced acceptance and by requiring in these regions a confirmation from the central tracking system. This allowed the muon criteria to be less sensitive to the detailed geometry of the muon detector with a moderate increase of background or fake rates.

nseg	Muon Type	Central track matching algorithm
3	Central track + local muon track (A and BC layer)	Muon to central if local muon track fit converged. Central to muon otherwise
2	Central track + BC only	central to muon
1	Central track + A only	central to muon
0	Central track + muon hit or central track + MTC	central to muon central to calorimeter
-1	A segment only	no match
-2	BC segment only	no match
-3	local muon track (A + BC)	no match

TABLE 1.1 – Overview of the different muon types at DØ.

Muon identification criteria

The definitions for Tight, Medium and Loose are given below.

- **Tight muons**
  Only $|nseg| = 3$ muons can be Tight. A muon is Tight if it has :
  – at least two A layer wire hits and at least one A layer scintillator hit ;
  – at least three BC layer wire hits and at least one BC scintillator hit ;
  – a converged local fit (χ^2_{loc} >0).
- **$|nseg|$=3 Medium/Loose muons**
  When a $|nseg|$=3 muon candidate fails the Tight criteria it might still be Medium or Loose. A $|nseg| = 3$ muon is Medium if it has :
  – at least two A layer wire hits and at least one A layer scintillator hit ;
  – at least two BC layer wire hits and at least one BC scintillator hit (except for central muons with less than four BC wire hits).
  A $|nseg| = 3$ Loose muon is defined as a Medium muon but allowing one of the above tests to fail, with the A wire and scintillator requirement treated as one test and requiring always at least one scintillator hit.

- *nseg*=+2 **Loose/Medium muons**
  Muons with $|nseg| < 3$ can only be Loose or Medium if they are matched to a central track. *nseg*=2 muons are muons with a BC segment matched with a central track.
  A *nseg*=2 muon is defined as Medium if it fulfills the above requirements and if it is located in the bottom part of the detector (octant 5 and 6 with $|\eta^{detector}|$ <1.6) with limited coverage of the muon chambers due to the calorimeter feet.
- *nseg*=+1 **Loose/Medium muons**
  Muons with *nseg*=1 are muons with an A segment matched with a central track. A *nseg*=1 muon is Loose if it has at least one scintillator hit and at least two A layer wire hits. A *nseg*=1 muon is defined as Medium if it fulfills the above requirements and if it is located in the bottom part of the detector (octant 5 and 6 with $|\eta^{detector}|$ <1.6). If a low momentum *nseg*=1 muon has less than 70% probability to go through the toroid, it is also promoted as Medium. For this condition, probability maps as a function of the muon momentum and $|\eta|$ have been established using simulation. Figure 1.1 shows the probability curves (markers) computed with generated muons with 3<p<4 GeV, 4<p<5 GeV and 5<p<6 GeV.

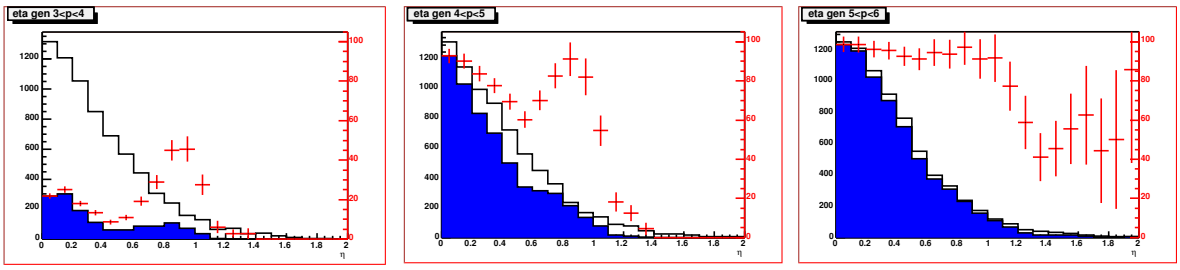

FIGURE 1.1 – Fraction of muons reaching the BC layer as a function of η (markers), determined from simulation, for different bins of generated momentum : 3<p<4 GeV (left), 4<p<5 GeV (middle) and 5<p<6 GeV (right). The open (shaded) histograms show the η distribution of the generated muons before (after) reaching the BC layer.

Cosmic veto

In addition to these muon identification criteria described above, the precise scintillator timing information is used to veto cosmic muons. After calibration, muons coming from the collisions for which scintillator informations exist are requested to have : $|t_A|, |t_B|$ and $|t_C| < 10$ ns. It is worthwhile to notice that the loose medium and tight tracking criteria defined below have dca cuts also suppressing cosmic muons.

In 2009 with one of my student, we have performed a specific study of these cosmic cuts [6]. The goal of the study was to verify the performance of the cuts that were established at the beginning of DØ Run II. A sample enriched in cosmic muons have been selected without trigger or scintillator requirements asking for two back-to-back muons ($A_\eta = |\eta_{\text{control}} + \eta_{\text{probe}}| < 0.02$ and $\Delta\phi = |\phi_{\text{control}} - \phi_{\text{probe}}| > 3.135$). This sample did not show any contamination in Z events and was used to compute the cosmic cut rejection.

The cosmic cut efficiency was measured using the standard tag and probe sample used to compute the muon efficiencies (see next section). This study shows that the current scintillator timing cuts ($|\Delta t| < 10$ ns) was close to be optimal (see for instance Figure 1.2) with an efficiency of $\epsilon = 98.19 \pm 0.05\%$ and a fake rate of : $f = 42.9 \pm 0.6\%$.

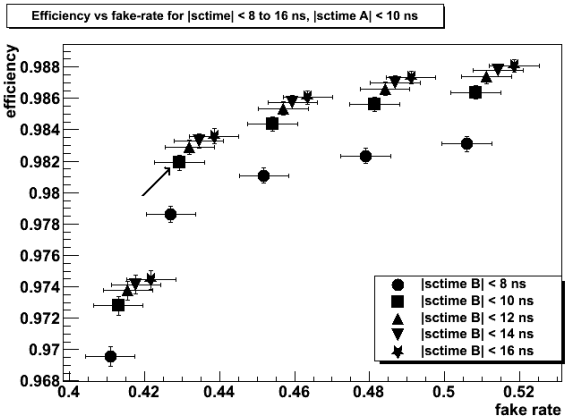

FIGURE 1.2 – Efficiency as a function of the fake rate with a fixed A timing cut ($|\Delta t| < 10$ ns) when B and C timing cuts are varying. The arrow represents the current cuts.

Historically the local muon criteria defined above have been the first that have been defined. Afterwards, standard quality on the matched central tracks and on the muon isolation have been set by the muon identification conveners following my term, as described below.

Track quality criteria

To control the purity of muons matched to central track, three qualities of track have been defined. They rely on the following track characteristics :

- number of hits either in the SMT or CFT system (central tracker) ;
- χ^2 per degrees of freedom of the central track fit ;
- distance of closest approach in the (x,y) plane : *dca* with respect to the primary vertex of the event.

The track quality definitions are the following :

- **loose track**
  A track is loose if $|dca| < 0.2$ cm. If the track has at least one SMT hit the cut is tighten to $|dca| < 0.02$ cm. Note that, for muons from Z decays, the typical resolution observed in the data are 20 μm and 500 μm for respectively tracks with and without SMT hits.
- **medium track**
  A track is medium if it fulfills the loose requirements and if the χ^2 per degrees of freedom of the fit in the tracking system is smaller than 4 : $\chi^2/d.o.f. < 4$.
- **tight track**
  A track is tight if it fulfills the medium requirements and if it has SMT hits.

In 2009 with one of my student, we have studied the performance of the track χ^2 cut that is used in the medium and tight track definitions [6]. The purpose of this study was in particular to look at the impact of the Tevatron instantaneous luminosity increase on this requirement. The efficiency of this cut was measured using dimuon high p_T isolated events. The selection of the sample to evaluate the fake track rejection was based on the fact that tracks with high transverse momentum coming from minimum bias interactions may have a higher chance to be fakes. This kind of track should be at high distance from the primary vertex along the beam axis (z axis). So this sample was selected requiring one muon matched to a track close to the primary vertex and another unmatched probe track away from it. In this sample, we saw a clear correlation between the χ^2 of the probe track and the number of SMT hits of this track. Such a fake track sample was not aimed at giving an absolute value for the tracking fake rate but rather a benchmark to study the relative fake rate variation as a function of the $\chi^2/d.o.f.$ cut. Figure 1.3 shows that the current cut is close to be optimal with an efficiency of $\epsilon = 96.71 \pm 0.03\%$ and a fake rate of $f = 10.7 \pm 0.4\%$ even if a cut at $\chi^2/d.o.f. < 5$ would increase the efficiency by 1.1 % and the fake rate by 6 %.

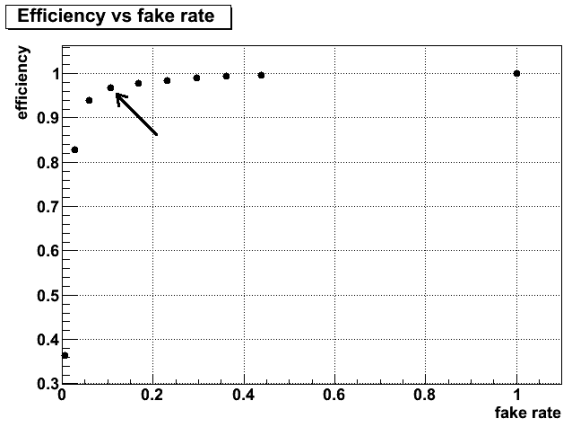

FIGURE 1.3 – Efficiency as a function of the fake rate for different cuts on $\chi^2/d.o.f.$. The current cut is shown by the arrow.

The tracker χ^2 cut efficiency depends linearly on the instantaneous luminosity as shown in Figure 1.4 where we can see that a looser cut leads to a flatter luminosity dependence. The efficiency also depends strongly on the number of SMT hits but both the integrated efficiency and the luminosity dependence is rather independent of the number of CFT hits. This study was recently at the origin for the creation of an additional track quality definition (called : newMedium) for which the luminosity dependence is much reduced ($\chi^2/d.o.f. < 9.5$, the default value for the $\chi^2/d.o.f.$ variable is 10).

Isolation criteria

Muon isolation cut variables are designed to separate high p_T muons from W or Z decays from heavy flavor background ($B \to \mu$). Because muons from heavy flavor decays tend to be embedded inside a jet, these variables are either defined in terms of the tracks near the muon track or calorimeter energy surrounding the muon momentum vector. Several

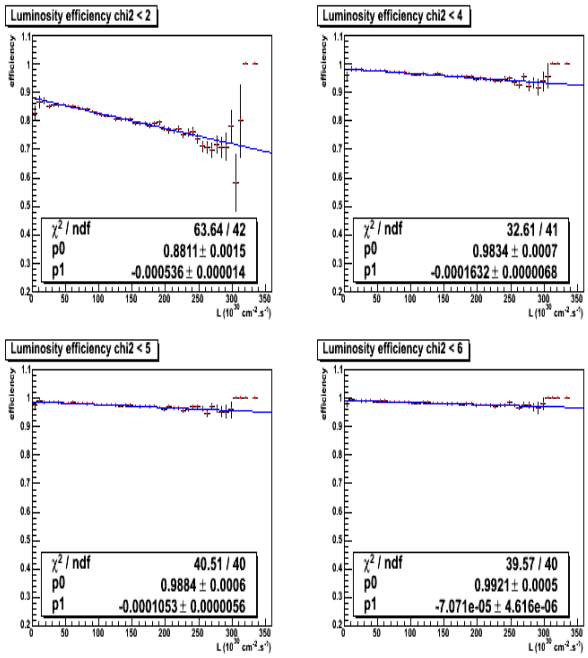

FIGURE 1.4 – Efficiency as a function of the instantaneous luminosity for different $\chi^2/d.o.f.$ cuts : 2, 4, 5 and 6.

standard isolation working points have been defined (not listed here) based on the following five variables :

- tracker halo isolation : $|\sum^{\text{tracks}} p_T|$ in ΔR(track, muon track)< 0.5 cone ;
- Calorimeter halo isolation : $|\sum^{\text{cells}} E_T|$ in $0.1 < \Delta R$(cal-cells, muon cal-track) < 0.4 ;
- $\Delta R(\mu, jet)$ = Distance to closest jet in $\eta - \phi$ space ;
- Scaled calorimeter isolation : $\mathcal{E}^{\text{cal}}_{\text{halo}} = |\sum^{\text{cells}} E_T/p_T(\mu)|$ in $0.1 < \Delta R$(cal-cells, muon cal-track)< 0.4 ;
- Scaled tracker isolation : $\mathcal{E}^{\text{trk}}_{\text{cone}} = |\sum^{\text{tracks}} p_T/p_T(\mu)|$ in ΔR(track, muon track)< 0.5 cone.

1.1.3 Muon Efficiency Measurement and Muon Certification

The muon identification group is in charge of centrally measuring the muon efficiencies in MC and in data for the standard muon definitions that have been described in the previous section. Any significant discrepancies between these two efficiencies should be corrected for in analyses with muons in the final state. The number of certified local muons, track quality or muon isolation categories has been limited to the ones above so that the efficiency measurements can be manageable. The muon trigger efficiencies for the three levels of the DØ trigger system have also to be computed.

During the time I was in charge of the muon id group, we have developped together with people from Manchester, the concept and tools to measure the muon high p_T muon efficiencies based on the work performed in the $Z \to \mu\mu$ and $W \to \mu\nu$ cross section analyses

(see chapter 2).

The efficiency computation is based on the so-called *tag and probe* method. The tag and probe method relies on the fact that a pure dimuon $Z \to \mu\mu$ event sample can be extracted without requiring tight criteria on both muons. More precisely, one of the muon (the probe muon) is required to be fully reconstructed (i.e. with trigger, local, isolation and tracking informations) to ensure the purity of the sample. The second muon (the tag muon) is selected with relaxed informations on one of the sub-systems (muon spectrometer, calorimeter or tracker) which will allow to test if it meets the criteria for which we want to compute the efficiency. This method is schematized in Figure 1.5. In the dimuon sample, the role of the two muons could be symmetrized, i.e. one muon could be used alternatively as a probe and as a tag.

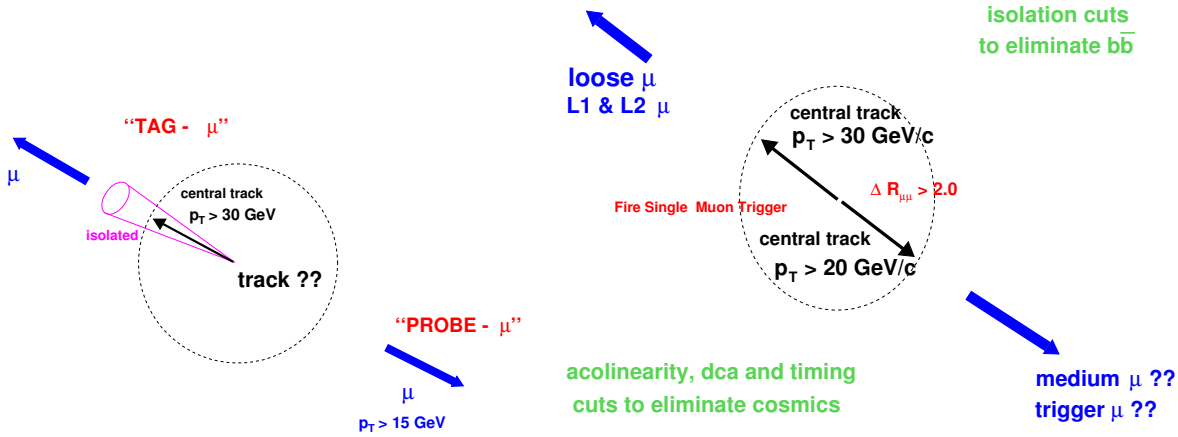

FIGURE 1.5 – Schematic view of the event selection for the tag and probe method to compute the tracking (left) or muon identification and muon trigger (right) efficiencies.

Note that this method using $Z \to \mu\mu$ events is only suitable to measure the efficiencies of high p_T muons ($p_T > 15$ GeV). Lower p_T resonances like J/ψ or Υ are not used due to their background contamination, trigger and reconstruction challenges.

In order to properly measure the efficiencies, special care should be taken for any potential bias in the selected events or any potential correlations between the two muons. For instance in order to compute the muon trigger efficiency, one should require that the selected events have triggered a single muon trigger for instance and that the tag muon was the muon responsible for this trigger. Possible bias could also appear if the measured efficiencies are not parametrized as a function of the right variables (see one example in the $W \to \mu\nu$ analysis in section 2.3.1). Correlations between the two muons could also be avoided by computing the efficiencies as a function of the right variables. For instance, as the muon spectrometer has a reduce coverage in the bottom part of the DØ detector, the tag muon can not point to that region. As in $Z \to \mu\mu$ events, the two muons are mostly back-to-back, in the tag and probe sample there are more probe muons pointed to the bottom part than to the upper part of the detector. Hence in order to avoid any bias, the muon efficiencies should be at least parametrized as a function of ϕ.

To compute the muon identification or muon trigger efficiencies, the tag and probe sample is selected by requiring an isolated matched medium probe muon with $p_T > 30$ GeV responsible for a single muon trigger and an medium isolated tag track (or loose track for the muon trigger efficiences) with $p_T > 20$ GeV acolinear with the probe muon. To measure the tracking and track trigger efficiencies, we require dimuon triggered events with an isolated matched loose probe muon with $p_T > 30$ GeV with a small dca together with a loose tag local muon with $p_{T\mathrm{loc}} > 15$ GeV acolinear with the probe muon. Finally to compute the isolation both tag and probe muons are loose and matched with $p_T > 15$ GeV. The tag muon should be responsible for a single muon trigger and should be isolated.

In 2004 using the tag and probe method on 150 pb^{-1}of data, the muon identification efficiency was measured as a function of the muon detector η or ϕ as can be seen in Figure 1.6. Later on in 2007, the amount of data available (1 fb^{-1}) allowed to better handle the efficiency computations by studying the luminosity dependence (as seen in the previous section), by performing two dimensional parametrization (as shown for instance in Figure 1.6) and by estimating different sources of systematic uncertainties.

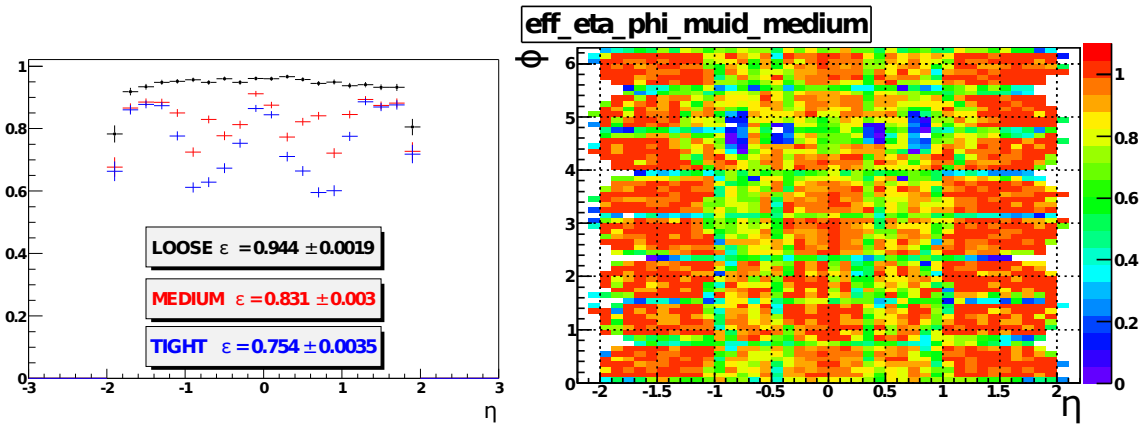

FIGURE 1.6 – Muon identification efficiency measured in 2004 (left) as a function of the muon detector η and in 2007 (right) as a function both η and ϕ.

The typical muon efficiency for loose muon is $95 \pm 0.5\%$ and $83 \pm 0.7\%$ for medium muon where the dominant sources of systematic uncertainty come from the presence of background evaluated by varying the selection cuts and from the bias of the tag and probe method (see its evaluatation in section 2.3.1). The data/MC corrections for these muons are around $0.995 \pm 0.004\%$ for loose muons and $0.98 \pm 0.007\%$ for medium muons. The tracking efficiency is around $94 \pm 2\%$ for loose tracks and $91 \pm 2\%$ for medium track with a data/MC scale factor of $0.96 \pm 0.02\%$ and 0.93 ± 0.02 respectively. The main uncertainty comes from the modeling of the z luminous region that was not correctly simulated at the time of the 2007 certification. The isolation MC/Data scale factors are compatible with 1.

As we have seen, after the first developments of the tools to compute the muon related efficiencies using the tag and probe and after the muon id group released the first measurements of these efficiencies centrally performed with these tools, several improvements have been brought over the years. The automatization of the tools have been developped, with interface with the new ROOT based common DØ format (CAF, see section 1.2.2).

The efficiencies have been measured as a function of multiple variables. Their dependencies as a function of the instantaneous luminosity have been studied as well as their stability over time. Nowadays, the DØ certification procedure is well established and provides all the needed and accurate inputs to the DØ analyses.

1.1.4 Muon Momentum Oversmearing

A comparison of the J/ψ and Z boson width observed in data and in the DØ simulation shows that the muon momentum resolution is not well modeled in the MC. Indeed, the Z width measured in data is typically 6.84±0.06 GeV while the one in the MC is 4.79±0.03 GeV. This difference points to simulation modeling limitations, in particular for the dead channels in the tracker, for the tracker hit resolutions or the modeling of the magnetic field, the amount of material in the simulation or alignment effects. Improvements in all these fields were carried out over the years but the exact origin of the remaining momentum resolution discrepancy was not fully understood. That is the reason why a MC muon momentum oversmearing correction was set up in 2004. This first version however suffered from large uncertainty due to the p_T dependence of the oversmearing parameters and correlated multiple scattering and resolution effects. In 2007 with one of my student, we have developped a new oversmearing procedure that uses both the J/ψ and Z resonances [7].

The oversmearing formula that we use to adjust the MC momentum to the one in data is :

$$\frac{q}{p_T} \rightarrow \frac{q}{p_T} + G\left(A \oplus \frac{B\sqrt{\cosh\eta}}{p_T}\right) \tag{1.1}$$

where G is a gaussian distributed random number with mean 0 and width 1. A is a term to adjust the resolution, while B is a multiple scattering term. To disentangle these two terms and as the influence of B is expected to be negligible at high momentum for muons from the Z boson decay, we need to use, in addition to a Z sample, J/ψ events that provide low momentum muons. For these events a background subtraction using same sign dimuon events is used as seen in Figure 1.7. The data invariant mass distribution for the sample of Z events used to determine the oversmearing parameters is also shown in Figure 1.7.

After background subtraction, the invariant mass distributions in data need to be shifted to get the same momentum scale as they are in MC. A normalization factor is also applied. Finally a χ^2 is built to compare the data histograms with the smeared MC histograms as a function of (A, B). The χ^2 obtained using Z events is independent of B whereas the χ^2 obtained using J/ψ events is mostly dependent on A and varies slightly with B. An example for the sum of both is shown in Figure 1.8.

As muons without hits in the SMT or outside the CFT acceptance ($|\eta_{\mathrm{CFT}}| > 1.6$) have poorer resolution, the oversmearing parameters are determined separately for these different kinds of muons. Systematic uncertainties on the oversmearing parameters are determined by varying the selection criteria and the mass ranges to compute the χ^2. For central muons with SMT hits, the parameters are typically : $A = 1.7 \pm 0.1$ (stat) $\pm$ 0.1 (syst) 10^{-3} GeV^{-1} and $B = 1.5 \pm 0.2$ (stat) $\pm$ 0.4 (syst) 10^{-2}. The found parameters with their errors are implemented in DØ standard tools to be run during data analyses. The procedure has also to be repeated when detector changes are expected to modify the resolution in data or if improvements in the MC description affect the resolution in the simulation.

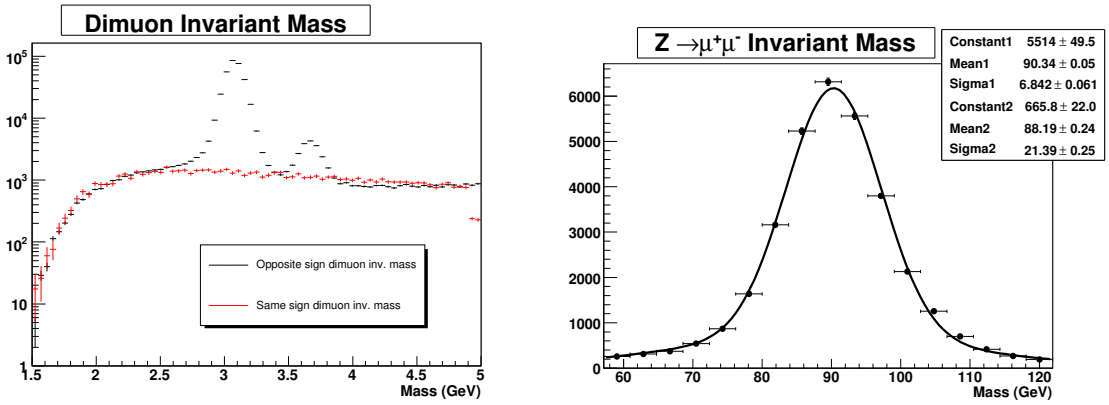

FIGURE 1.7 – Opposite sign and scaled same sign data invariant mass distribution for J/ψ events (left). Z invariant mass distribution in data fitted with a double gaussian.

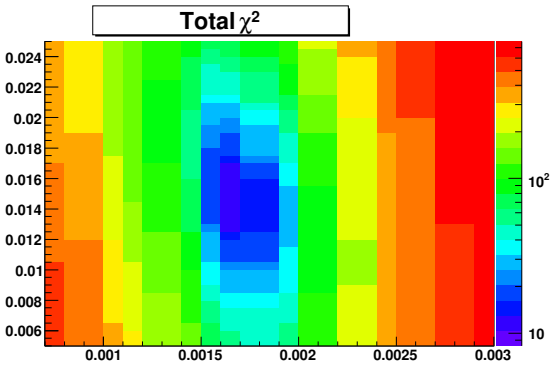

FIGURE 1.8 – Sum of the χ^2 between MC and data for Z and J/ψ events as a function of the smearing parameters (A, B) for muons with SMT hits with $|\eta_{\mathrm{CFT}}| < 1.6$.

The method described above can also be used to determine the muon momentum resolution in data by using as input the MC generated muons. The result is summarized in Figure 1.9.

This work has been further extended in 2010 by including the possibility to smear the high momentum tail of the muon momentum distribution and by adjusting the overall muon momentum scale together with the muon resolution.

1.2 Common Analysis Tools

Apart from my muon identification activities, I contributed to different aspects in the developments of DØ common analysis tools especially during my term as convener of the *Common Sample Group* from 2003 to 2005. This section starts with an overview of how DØ data is transformed from raw data to physics results. Then I shortly summarize my specific contributions to the DØ common tools.

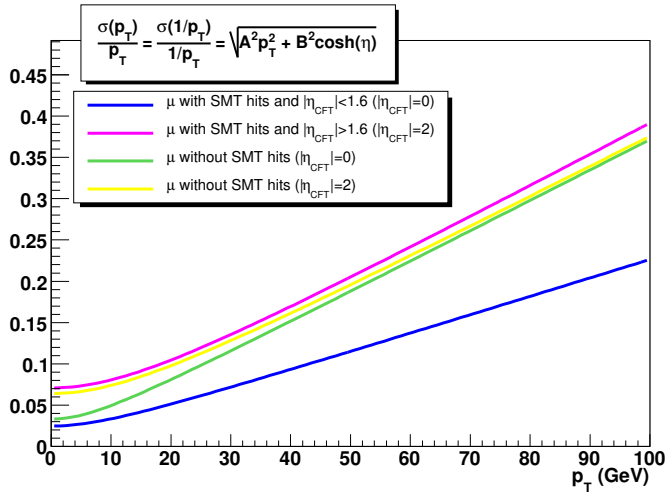

FIGURE 1.9 – Momentum resolution for different muon tracks.

1.2.1 Overview of the DØ data processing chain

Objects reconstruction is the first step of the DØ data processing chain after data recording. The DØ reconstruction program (d0reco) converts raw data into reconstructed data. A packed summary of the outputs of the various reconstruction algorithms is called a *thumbnail*. In order to be able to re-reconstruct the data from that level of informations, thumbnails also contain track clusters and calorimeter cell informations. This type of re-reconstruction can however only be performed without accessing calibration data.

The Common Sample Group was formed in 2003 to manage the post-thumbnail processing. Three types of standard thumbnail processing are being performed : fixing, skimming and application of common object corrections.

In order to get the latest vertexing, the latest calorimeter corrections and bug fixes, DØ performed fixings of its datasets. Fixing is a way of re-reconstructing events starting from thumbnail alternatively from running d0reco again. All the reconstruction could then be rerun except the early steps of track and muon finding.

The goal of skimming is to reduce the dataset to be processed in each analysis. To avoid work duplication, it is done centrally by the Common Sample Group resulting in skimmed thumbnails. Thirteen physical skims are written out based on the number of leptons and jets in the recording events, or based on which specific triggers were fired.

I especially developped the thumbnail post-processing that consists of applying common object corrections (gathered in a package named : *d0correct*. It will be described in section 1.2.3 below.

Finally after post-processing the corrected skimmed thumbnails are converted into root-trees called *CAF-tree*. This format is described further in section 1.2.2 below.

A summary of the DØ reconstruction chain is shown in Figure 1.10.

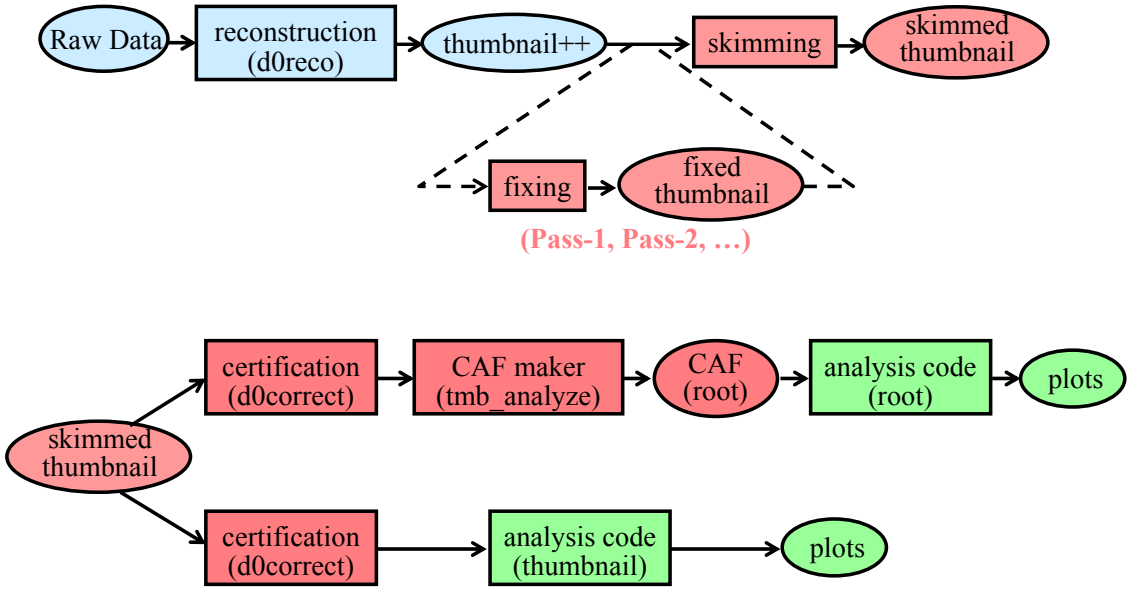

FIGURE 1.10 – Schematic view of the DØ data tiers and processing chain.

1.2.2 Common analysis format : CAF

In 2004, a data format working group was formed in order to review the available root-based formats existing in DØ at the time, to understand the advantages and drawbacks of each data format and to develop a common root-based data format to be used by all physics group of the collaboration incorporating desirable features of existing formats and analysis tools. I was a member of that group. The new proposed format named *CAF* (for Common Anaysis Format) required to contain enough informations to support most of DØ analyses with a reasonable size per event and needed to be read much quickly than thumbnails. Apart from the reading speed, the obvious advantages of a common format is to reduce the software development and maintenance efforts of the physics groups and to facilitate the sharing of data and analysis algorithms. The possibility to port it to non DØ environment was also a requirement for such a common format.

After reviewing the existing analysis formats at the time, it was decided to develop a common format that is an objected-oriented root tree. The development of CAF started from an existing root format in 2004 and was fully deployed in 2005. CAF trees are centrally produced by the Common Sample Group. The format was a great success and significantly improve the productivity of the experiment. The large majority of the DØ analyses are now using it.

1.2.3 Common corrections on reconstructed objects

Standard reconstructed object corrections are gathered into a package named *d0correct*. This central package is aimed at applying all the post-reconstruction object corrections as well as object certification cuts in a coherent way for electrons, muons, jets and missing transverse energy. I have created it in 2003. It runs on thumbnails before making CAF-trees.

This post processing includes in particular :

- for muons : remove duplicate muons if any, set the muon quality criteria according to the certification (see section 1.1.2), apply the muon momentum smearing (see section 1.1.4) ;
- for electrons : apply the electromagnetic energy scale, the latest geometrical corrections if any, apply cuts to define good electromagnetic objects ;
- for jets : apply jet energy scale, apply certified cuts to remove bad jets, remove jets that are in fact electrons, apply jet momentum smearing ;
- for missing transverse energy : recompute the missing transverse energy taking into account certified electrons, jets and muons, apply energy scale corrections.

After the full development of CAF, the possibility to apply most of these post-processing at the CAF level has been added.

1.3 Conclusion

In this chapter, I presented an overview of the developments of the analysis tools over the year at DØ from the basic tools to compute reconstruction and trigger efficiencies to the common tools and format centrally produced for the whole collaboration. Some of these developments could have been put in place earlier in the run but at the end these were one of the main ingredients for the success of DØ Run II.

I was personnally involved into improving the muon identification criteria and into setting up the muon efficiency measurement and certification method. This method have been further automatized afterwards. Tools to apply MC/data efficiency ratios on MC events have also been built up. I participated into the DØ CAF revolution to successfully develop a common ROOT based format and to adapt the tools to apply MC correction factors on this new format. Common corrections that I first implemented have been afterwards also ported to be applied on CAF files. This common format significantly improved the productivity of the experiment in delivering physics results in a timely manner.

Chapter 2

Measurement of the inclusive production of W boson into muon at DØ

Contents

2.1 Physics Motivations **30**
2.2 Data Samples and Selection of the $W \to \mu\nu$ Events **31**
2.3 Efficiency Computation and Fast Simulation **33**
2.3.1 Trigger, Muon and Tracking Efficiency 33
2.3.2 Isolation Efficiency 36
2.3.3 Fast Simulation 37
2.4 Background Estimation **38**
2.5 Results **40**
2.6 Conclusion **43**

Between 2002 and 2005, I have worked together with other colleagues from Saclay and Manchester on the measurement of the inclusive $W \to \mu\nu \times \mathcal{B}(W \to \mu\nu_\mu)$ cross section in $p\overline{p}$ collisions at DØ. This work has led to two DØ preliminary results in 2003 [8] and 2005 [9]. The main parts of these analyses are summarized in this section. The first analysis in 2003 was performed only a few months after the beginning of the Run II data taking. Hence especially for this analysis a lot of the tools that are now available centrally had to be developped in order to successfully perform the analysis. When appropriate, we will outline the significant difference with the analyses tools that are now commonly used at DØ.

2.1 Physics Motivations

The W boson is one of the mediator of the weak interaction. It has been discovered at the CERN $Sp\bar{p}S$ in 1982 by the UA1 [10] and UA2 [11] experiments consolidating the construction of the Standard Model (SM) of particle physics. The measurement of the inclusive production cross sections for both the W and Z boson in $p\overline{p}$ collisions at high energy and high luminosity at the Tevatron is an important test of the SM. At hadron colliders the W and Z boson are essentially identified through their leptonic decay modes. The main W boson production diagram at the Tevatron is shown in Figure 2.1.

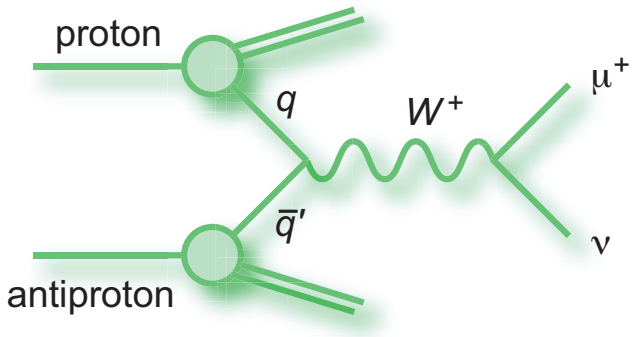

FIGURE 2.1 – Main Feynman diagram for the W boson production at the Tevatron.

The W boson inclusive production provides a standard candle to study the performance of the detector and reconstruction in an experiment. So the measurement of the W boson inclusive production cross section was one of the priority of DØ at the beginning of the Run II data taking. Besides this important role, measuring the W boson cross section provides a test of the SM predictions as well as a precise indirect measurement of the total decay width of the W boson Λ_W within the framework of the SM. Indeed, together with the measurement of the Z boson cross section, it allows to build the ratio :

$$R = \frac{\sigma_W \mathcal{B}(W \to \mu\nu)}{\sigma_Z \mathcal{B}(Z \to \mu\mu)} = \frac{\sigma_W}{\sigma_Z} \frac{\Gamma(W \to \mu\nu)}{\Gamma(Z \to \mu\mu)} \frac{\Gamma(Z)}{\Gamma(W)}.$$

σ_W/σ_Z can be calculated precisely while $\Gamma(Z)$ and $\Gamma(Z \to \mu\mu)$ have been very well measured at the LEP experiments. Then using the SM predictions for $\Gamma(W \to \mu\nu)$, the measurement of R allows to extract indirectly $\Gamma(W)$.

The ratio of W boson cross sections when the W boson decays into a muon or an electron can also be used to determine the ratios of the W boson coupling constants to the muon or electron and then provides a test for lepton universality.

2.2 Data Samples and Selection of the $W \to \mu\nu$ Events

The first analysis in 2003 [8] used a data sample limited to the data collected by DØ from September 2002 to January 2003 corresponding to an integrated luminosity of 17.3 pb^{-1}. The second one in 2005 [9] was already not limited anymore by the number of $W \to \mu\nu$ candidates (62,285) and used better undestood data collected from February 2003 to September 2003 corresponding to an integrated luminosity of 95.6 pb^{-1}.

The $W \to \mu\nu$ signal is characterized by an isolated muon with high transverse momentum (p_T) and significant missing transverse energy ($\not\!\!E_T$) that signs the presence of an escaping neutrino. The muon is identified by tracks in the central track as well as in the muon spectrometer. The $\not\!\!E_T$ is computed as the inverted vector sum of the energies in the calorimeter corrected for the momentum of the muon.

Several backgrounds to the $W \to \mu\nu$ events can be identified. First a veto on events that contain another high p_T reconstructed muons or a second high p_T track is applied to reduce contamination from cosmic rays and $Z \to \mu\mu$ events. The amount of events with one jet decaying semileptonically into a muon (in particular in the production of $b\bar{b}$ QCD events) is reduced by requiring an isolated muon both in the calorimeter and in the tracker. Background from pions or kaons that decay in the central tracker into muons is reduced by requiring quality cuts on the central track attached to the signal muon. Indeed such in-flight decays produce a kinked track that affect the track reconstruction.

In order to be able to compute the signal selection efficiency properly, $W \to \mu\nu$ events are required to fire specific single muon triggers. These triggers are evolving versus time depending on the instantaneous luminosity delivered by the Tevatron. Due to their relatively high rate, they are often prescaled. Typically for the 2005 analysis, two single muon triggers were used that require at least one muon trigger either within $|\eta_{det}| < 1.5$ ('wide' region) or 2 ('all' region) with tight scintillator timing cuts and loose wire requirements at Level 1, a medium Level 2 muon with $p_T > 3$ GeV, and at least one Level 3 central track with $p_T > 10$ GeV.

In the early version of the analysis in 2003, the data quality for the different subdetectors was not fully established. We have then checked the measured cross section for observing one medium muon matched to a central track and passing the trigger requirement as a function of the run number. This is shown in Figure 2.2. This check has allowed us to identify further the bad runs compared to the available bad run lists. It illustrates one of the interest to perform the measurement of the $W \to \mu\nu$ cross section in an early stage of an experiment. Such a measurement also allows to understand and check the full analysis chain in particular the data quality, trigger, reconstruction and identification efficiencies.

To select $W \to \mu\nu$ events the following cuts have been applied :

- Events must fire the selected single muon triggers (either in the 'wide' or in the 'all' region). For each run, one of these triggers was selected depending on its prescale. When the 'wide' region trigger had a lower prescale it is selected. When the prescales

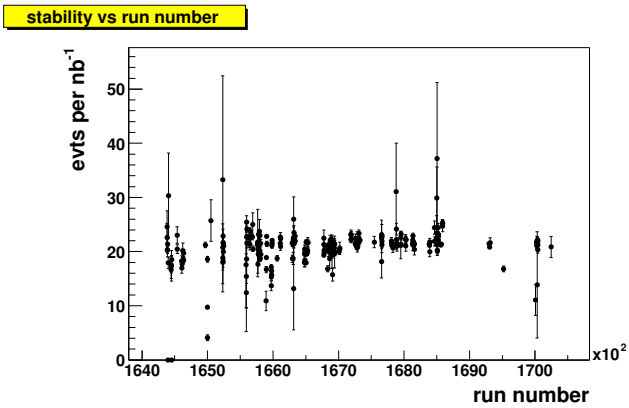

FIGURE 2.2 – Number of cumulated events with at least one medium muon matched to a central track passing the trigger requirement divided by the per run integrated luminosity as a function of the run number.

of the two triggers were equal, the 'all' region trigger was selected to take advantage of its larger acceptance.

- Events are required to contain one medium quality muon matched to a central track with at least one hit in the silicon tracker (SMT), with a distance of closest approach to the beam position (dca) less than $|dca| < 110$ μm and with a χ^2/d.o.f. from the fit in the central tracker less than 3.3. The muon central track must be greater than 20 GeV.
- In order to be consistent with the way the efficiencies have been computed, the muon is required to be within the geometrical acceptance of the muon detector, namely not in the forward region around the beam pipe and out of the bottom region within detector coverage due to the detector supports.
- The muon is required to be isolated in the calorimeter and in the central tracker with detector criteria varying with the instantaneous luminosity per bunch crossing $\mathcal{L}_\mathcal{I}$ (in units of $10^{30} cm^{-2} s^{-1}$) : $\sum_{0.4}(E_T) - \sum_{0.1}(E_T) < 1.65 + 0.75\mathcal{L}_\mathcal{I}$ GeV with $\sum_{X.X}$ being the sums of the E_T of the calorimeter cells in a cone of $\Delta R = 0.1$ or $\Delta R = 0.4$ around the muon, and $\sum_{0.5}(p_T) < 1.1 + 0.5\mathcal{L}_\mathcal{I}$ GeV where $\sum_{0.5}(p_T)$ is the sum of the p_T of the tracks contained in a cone of $\Delta R < 0.5$ around the muon direction (excluding the track of the muon). The exact value of these cuts have been chosen so that the isolation efficiency is indenpendent of the luminosity. Note that these isolation criteria are independend of the p_T of the muon. To further reduce QCD heavy flavor background, a p_T dependent isolation cut is now mostly used for the DØ analyses. It has also to be noticed that efficiencies currently measured in data that appear to be significantly dependent on the luminosity are parametrized versus instantaneous luminosity.
- The reconstructed muon has to matched the single muon trigger object that fired the event. This cut is required to be consistent with the trigger efficiency computation since trigger efficiencies are computed with respect to reconstructed offline muons.
- The missing transverse energy corrected for the muon momentum is required to satisfy : $\not{E}_T < 20$ GeV

– The transverse mass M_T has to be greater than 40 GeV to remove a region where the heavy flavor QCD background is difficult to model.
– Events that contain a second medium quality muon separated from the signal muon or a second central track with $p_T > 20$ GeV with the same quality as the central track from the signal away from it are vetoed.

After applying these cuts and in order to extract the $W \to \mu\nu$ cross section, we have to compute both the efficiency to select $W \to \mu\nu$ signal events and to estimate the number of background event contamination in the selected sample. These two steps are summarized in the two following sections.

2.3 Efficiency Computation and Fast Simulation

The procedure to measure the efficiencies on data is based on the so-called "tag and probe" method (see section 1.1.3).

These measured efficiencies are then parametrized as a function of the relevant kinematic variables and then implemented in MC so that it reproduces the efficiency in data. At the time of the analysis, it was not possible to produce large amount of MC samples needed for this measurement. A fast simulation that parametrizes the detector resolution was then used to estimate the signal acceptance as well as the electroweak backgrounds.

2.3.1 Trigger, Muon and Tracking Efficiency

Muon identification efficiency is computed using a $Z \to \mu\mu$ sample selected with one tag isolated high p_T muon matched to a single muon trigger object and a high quality isolated probe track (see section 1.1.3 for more discussion on muon efficiency computation). Both muon and track should be acolinear and oppositely charged. Counting the number of times an identified muon is reconstructed in association with the probe track leads to the measurement of the muon identification efficiency. In the first version of the analysis in 2003, the probe track was required to be matched to a Minimum Ionizing Particle (MIP) energy deposit signal that the muon would have generated in the calorimeter. It has been shown that this requirement is in fact not needed to enhance the purity of the tag and probe selected Z sample. An example of the efficiency for medium quality muon is shown in Figure 2.3.

The same kind of selection but requiring an offline muon associated with the probe track allows to measure the muon trigger efficiency.

The tracking and track trigger efficiency is computed using a $Z \to \mu\mu$ sample selected with one tag high p_T muon matched to a central isolated track with low dca and a probe loose quality muon. The two muons are asked to be separated and passing the requirements on the timing of the scintillators. The events are required to have a fire a dimuon trigger without track requirements to avoid any trigger bias in the efficiency computation. Counting the number of times a good quality track is associated with the probe muon allows to measure the track related efficiencies. This measurement allow us to stress the importance of the choice of the efficiency parametrization. Indeed, to ensure that there are no significant bias from the tag and probe method the efficiencies have been also mesasured using full simulated MC events. The true efficiency can then be computed by looking if a reconstructed track is

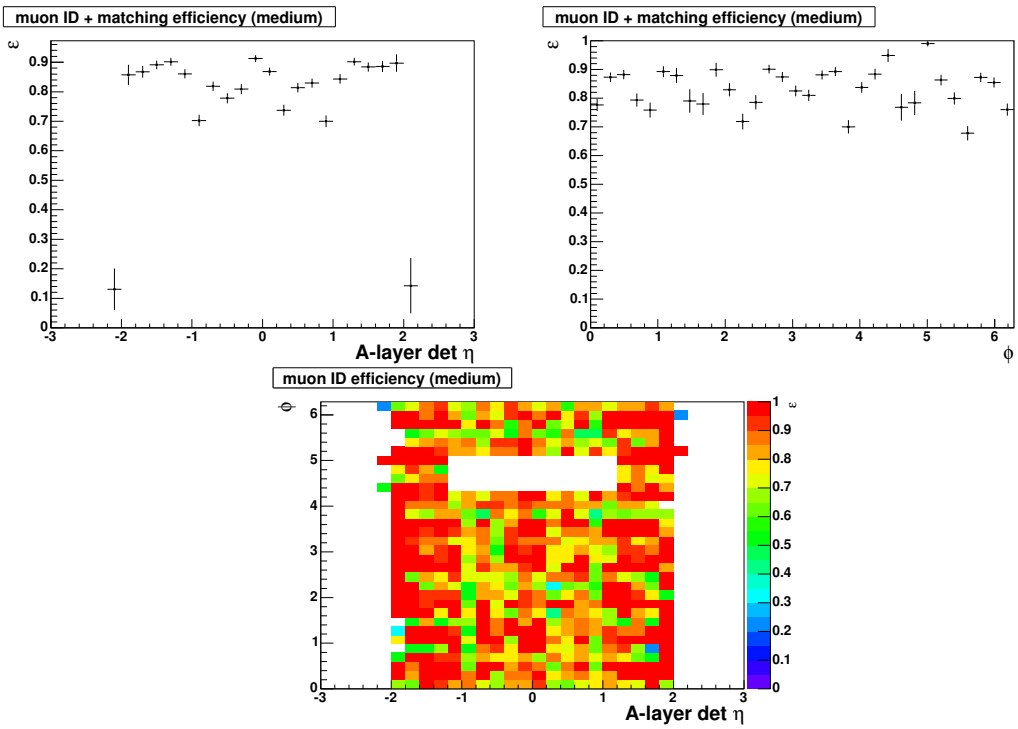

FIGURE 2.3 – Medium quality muon efficiency measured in data using the tag and probe method as a function of the muon detector layer-A η and ϕ in projection and the two dimensional distribution.

found near the generated muon track. A first comparison with the true efficiency and the efficiency from the tag and probe method applied on MC events shows a significant bias of about 3% as a function of the CFT detector pseudorapidity (see Figure 2.4).

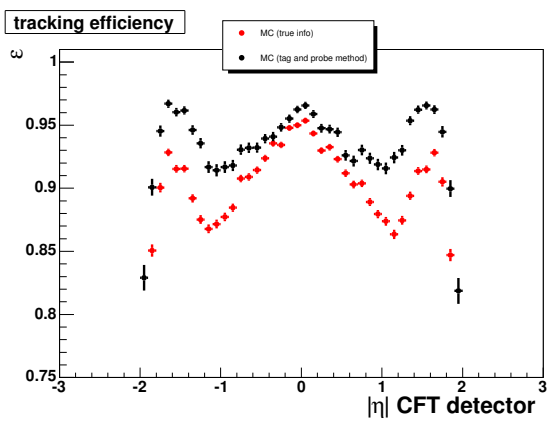

FIGURE 2.4 – Comparison of the true track efficiency in MC $Z \to \mu\mu$ events (red) with the measured efficiency in MC using the tag and probe method (black) as a function of the CFT detector η.

This bias is due to the dependence of the tracking efficiency as a function of the position of the track along the beam axis z due to the acceptance of the SMT detector. A way to remove this bias is to evaluate this efficiency in bins of z as seen in Figure 2.5 where the bias has mainly disappeared. The remaining difference is around 0.2% and is taken as a systematic uncertainty.

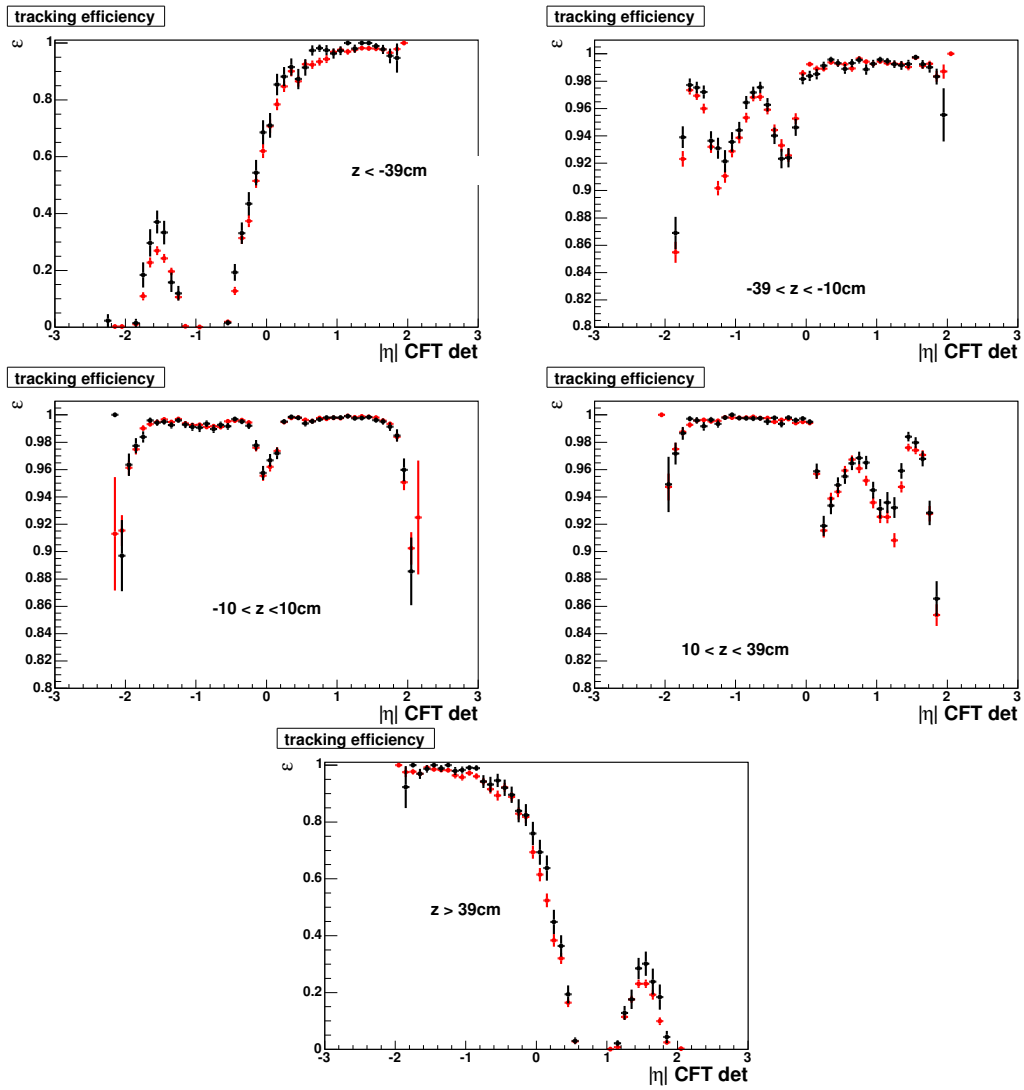

FIGURE 2.5 – Comparison of the true track efficiency in MC $Z \to \mu\mu$ events (red) with the measured efficiency in MC using the tag and probe method (black) for different bins of z as a function of the CFT detector η.

The average efficiencies measured in data with the tag and probe method are summarized in Table 2.1.

It has to be noticed that even if the tag and probe method is a very powerful tool to measure efficiencies on data, its limitation lies into the number of Z events available which often does not allow to parametrize the efficiencies as a function of more than two variables.

Efficiency	relative to	in %
medium muon		82.8 ± 0.4 (stat) ± 0.2 (sys)
L1 scintillator trigger (L1S)	medium offline muon	91.7 ± 0.3 (stat)
L1 wire trigger (L1W)	medium and L1S	97.4 ± 0.2 (stat)
L2M3	medium, L1S and L1W	98.4 ± 0.5 (stat)
high quality track		83.4 ± 0.4 (stat) ± 0.2 (sys)
L3TRK	offline track	79.2 ± 0.5 (stat) ± 0.6 (sys)

TABLE 2.1 – Summary of the average measured efficiencies in data using the tag and probe method. The L1 muon trigger efficiencies are quoted for the 'all' region trigger term ($|\eta| < 2$)

In the current DØ analyses, such efficiencies are now centrally produced for all the different reconstructed objects (electron, muon and jets) both in the data and MC samples. Standard tools are also available to apply the parametrized ratio of efficiency between data and MC on fully simulated MC samples.

2.3.2 Isolation Efficiency

The isolation criteria in the 2005 version of the analysis (see section 2.2) have been chosen to cancel the instantaneous luminosity dependence of the isolation cuts. However since the range of luminosity variation in the data sample was rather small, performing the analysis with isolation cuts that were not luminosity dependent (as in the 2003 version of the analysis) led to the same result. At that time, the MC simulation were generated with an average luminosity of $\mathcal{L} = 0.6 \times 10^{30}\ cm^{-2}s^{-1}$. In the current DØ analyses, zero bias colliding data are overlaid to the generated hard scattering in the MC simulation so that it better reproduces physics data samples. In addition the luminosity profile of these MC simulation samples, corresponding to the luminosity profile of the overlay zero bias events, is reweighted to the one measured in the signal data samples.

In the 2005 version of the analysis, the isolation efficiency has been measured in $Z \to \mu\mu$ data using the tag and probe method where the tag muon is required to be isolated to reduce the contamination from heavy quark initiated jets, while the number of isolated probe muons allow to measure the isolation efficiency. However using this technique, two biases have been observed when checking the method on full simulation. First requiring the tag muon to be isolated leads to an isolation efficiency 1% higher than the true one because of correlation between the two muons. Indeed the isolation strongly depends on the number of reconstructed tracks which is common between the two muons. We corrected for this bias in the efficiency measurement in data. In the current DØ analyses, this correction is taken as a systematic uncertainty.

The second bias comes from the dependency of the isolation efficiency on the muon p_T (see Figure 2.6). This is understood to come from the fact that low p_T muons are more likely to be located in the opposite hemisphere of the Z boson boost, while high p_T muons will be along the boost of the Z boson. The opposite hemisphere of the Z boson boost will also contain jets recoiling against the Z and then the low p_T muons are less likely to be isolated. This bias is simply taken into account by parametrizing the isolation efficiency as a function

of the muon p_T. The isolation efficiency is also found to be slightly dependent on η and so will vary with the acceptance of the muon trigger. For the 'all' trigger requirement, the isolation efficiency is measured to be : $\epsilon = 84.6 \pm 0.6(\text{stat}) \pm 0.5(\text{sys})\%$.

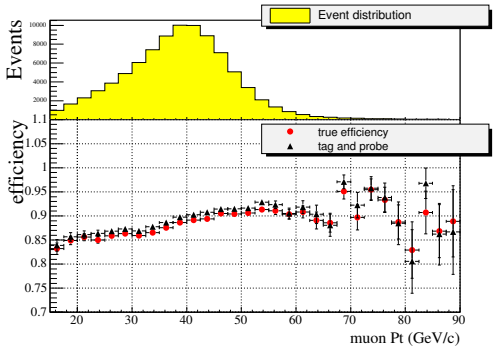

FIGURE 2.6 – Isolation efficiency as a function of the probe muon p_T.

This isolation fake rate will be discussed in the background section below (see section 2.4).

2.3.3 Fast Simulation

At the time the analyses were performed we did not have enough statistics available for the MC simulation. So the evaluation of the electroweak backgrounds, the $W \to \mu\nu$ efficiency, the uncertainties on the signal acceptance as well as the efficiency for the $Z \to \mu\mu$ veto were evaluated using a fast MC simulation. This fast simulation program (PMCS : Parametrized Monte Carlo Simulation) is based on parametrized physics processes and works by simulating the smearing effects of the DØ detector on reconstructed physics objects like electrons, muon and jets.

My work on PMCS has been focused in particular on the muon simulation. The effects of detector resolution on the measured muon p_T is simulated using three parameters A, B and then C as :

$$\begin{aligned} \frac{\sigma_{1/p_T}}{1/p_T} &= \sqrt{A^2 \frac{{p_T}^2}{L^4} + \frac{B^2}{L \sin\theta}} \\ p_T &= C.p_{T_{\text{smear}}}. \end{aligned}$$

A parametrizes the effect of the tracker and muon spectrometer resolution in the measurement of p_T, while B parametrizes the effect of multiple scattering. C corresponds to the mismeasurement of the muon scale due to the imperfect description of the magnetic field and energy loss through material applied after the corrections using A and B. L is the pending lever arm and θ the polar angle of the muon track.

The parameters A, B and C have been ajusted to reproduce the width and mean values of the $Z \to \mu\mu$ invariant mass distribution in a way similar to what is currently used to smear the full simulation (see section 1.1.4).

A parametrization of the $\not\!\!E_T$ simulates the $\not\!\!E_T$ resolution using the recoil jet and the effect of the underlying event. The muon energy deposit in the calorimeter (MIP signal) has

been fitted to reproduce the recoil of the W boson along the direction of the muon in the data.

As we have seen in section 2.3.1 the tracking efficiency is very dependent on the z position of the muon track. It is then important to reproduce correctly the event vertex distribution along the beam axis in the fast MC. To do so, both the width and the offset of the gaussian distribution of the DØ interaction region has been ajusted in the data and applied as weight to the fast MC.

Using this fast MC, for the 'all' trigger region, the acceptance for $W \to \mu\nu$ events is found to be : $\epsilon = 25.6 \pm 0.1(\text{stat}) \pm 2.0(\text{sys})\%$. The systematic uncertainty quoted here includes the PDF uncertainty, the error coming from the efficiency measurements and the modeling of the fast MC.

In most of the current DØ analyses the full MC simulation is now used. The efficiencies for reconstructing physics objects are centrally produced and parametrized as a function of the relevant variables. Generic tools allow to apply the ratio of these efficiencies measured in data and MC to the MC samples so that the efficiencies in the MC matched the ones in data. Tools to match the luminosity in MC and data or to reweight the beam distribution in the MC to the one measured run by run in the data are also now used by default.

2.4 Background Estimation

The four sources of background for the $W \to \mu\nu$ signal are :

- the electroweak background from $Z \to \mu\mu$ events where one of the two muons is not identified and $W \to \tau\nu$ or $Z \to \tau\tau$ where at least one τ lepton is decaying into a muon. This background is estimated using the fact MC simulation computing the ratio f_{EW} of cross section times efficiencies of such electroweak processes to the $W \to \mu\nu$ signal ;
- candidate events from quarks decaying semi-leptonically into muons (so called QCD background) ;
- contamination from mesons such as pions or kaons that decay inside the tracking volume (so called in-flight decays) ;
- background from cosmic rays.

We will discuss here shortly the last three background that are estimated using data. The QCD background was estimated using the so called matrix method which uses a set of two equations, one with a loose cut and the second with a tight one, to extract the number of signal and background events :

$$\begin{aligned} N_l &= B + S \\ N_t &= fB + \epsilon S. \end{aligned}$$

Here N_l is the number of data events having dropped the isolation requirements composed of a number of background events B and a number of signal $W \to \mu\nu$ events S. N_t represents the number of data events in the standard selection with isolation applied. f is the efficiency for a background events to pass the isolation cuts (isolation fake rate) and ϵ is the isolation efficiency on signal events computed in section 2.3.2. Solving these two equations leads to the number of background events after the final selection : $B = \frac{\epsilon N_l - N_t}{\epsilon - f}$.

To compute the isolation fake rate f, we need to build a sample dominated by QCD background with kinematic properties as close as possible to $W \to \mu\nu$ events. In the 2005 version of the analysis, this background dominated region was obtained using events with high $\not\!\!E_T$, high W transverse mass M_T and low muon p_T. The normalized number of events passing the isolation requirements in such a sample as a function of the muon p_T is shown in Figure 2.7.

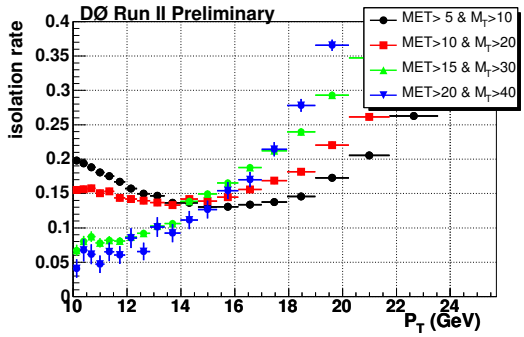

FIGURE 2.7 – Isolation fake rate as a function of the muon p_T for different $\not\!\!E_T$ and M_T requirements.

At high p_T the background sample becomes contaminated with $W \to \mu\nu$ events which biases the fake rate towards higher value. We estimate the fake rate looking at the low p_T region of the plots for high $\not\!\!E_T$ values. To extrapolate the value at high muon momentum, we have used the dependency of the isolation as a function of muon p_T in $Z \to \mu\mu$ events and same charge dimuon events. Both show a decrease of the isolation when the muon p_T increases. However the estimation of the fake rate using all these different samples does not lead to the same value which demonstrates the fact that the fake rate is sensitive to the overall kinematic configuration of the events. This was already observed in the 2003 analysis. Indeed for this early version, the background sample to measure f was built by requiring events with low $\not\!\!E_T$. It was shown that the isolation fake rate is highly depending on the actual $\not\!\!E_T$ cut used to define this sample (see Figure 2.8). The decrease of the fake rate when the $\not\!\!E_T$ upper bound is decreasing was checked using a MC $b\bar{b}$ sample. This makes the extrapolation of this measured fake rate in the signal region at high $\not\!\!E_T$ difficult.

In the 2005 version of the analysis, we have conservatively estimated : $f = 0.03 \pm 0.03$. This allowed us to extract the number of QCD events from the matrix method to be : $f_{\mathrm{QCD}} = 0.8 \pm 0.8\%$ for the 'all' trigger region.

The other sources of background come from mesons that decay into muons inside the tracker volume. A single track could then be fitted from the combination of the meson track and its muon decay with worse χ^2 than the ordinary track together with a high dca and poorer p_T resolution. Cosmic rays can also be a source of background if they are reconstructed in both the tracker and the muon spectrometer which result again in tracks with large dca. To estimate these two background sources, the dca distribution in data prior to any dca cuts is fitted with a sum of background and signal templates to estimate the fraction of in-flight decays and cosmic rays in the signal sample. The template dca signal sample has been obtained from $Z \to \mu\mu$ events while the sample dominated by cosmic muons is built by

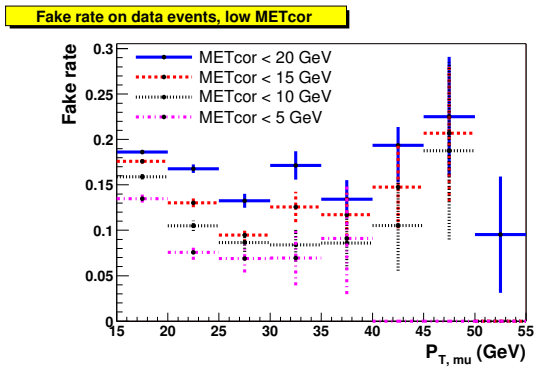

FIGURE 2.8 – Isolation fake rate as a function of the muon p_T for different $\not\!\!E_T$ upper bound.

reversing the acolinearity cuts and the sample dominated by QCD background by reversing the isolation criteria. The template for the in-flight decays can be obtained either in a sample without any track χ^2 cut applied or by applying a higher cut on the muon p_T measured in the spectrometer. An example of the fitted dca distribution using the above templates is shown on Figure 2.9. This fit allows to extract the number of remaining in-flight decay and cosmic rays background in the signal sample after the dca requirement which is estimated to be $f_{\text{IFD}} = 0.25\%$ of the number of $W \to \mu\nu$ events.

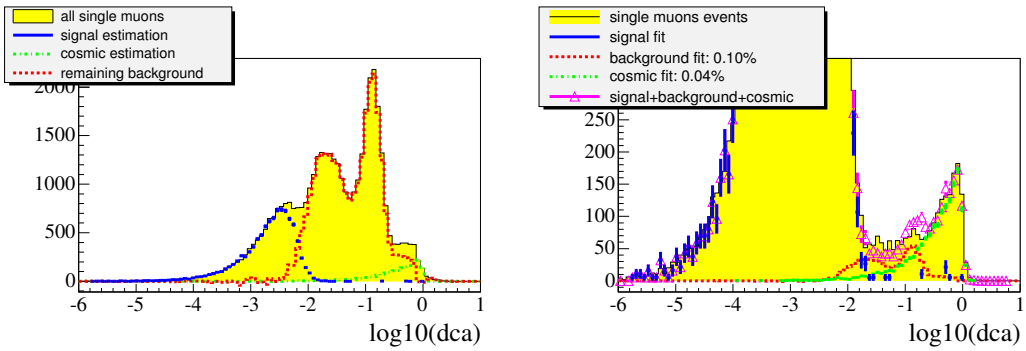

FIGURE 2.9 – fit of the log10(|dca|) distribution using as template for the in-flight decay background a sample without track χ^2 cut and with an upper cut on the muon p_T measured in the spectrometer : $p_T < 20$ GeV. (left) Fit to determine the in-flight decay template, (right) fit of the signal sample to determine the number of in-flight decay background in the final sample.

2.5 Results

The inclusive $W \to \mu\nu$ production cross section can be computed using the following formula :

$$\begin{aligned}\sigma(p\overline{p} \to WX)\mathcal{B}(W \to \mu\nu) &= \frac{N_{\text{data}} - N_{\text{bkg}}}{\epsilon\mathcal{L}} \\ &= \frac{N_{\text{data}}}{\epsilon\mathcal{L}} \frac{(1 - f_{\text{QCD}} - f_{\text{IFD}})}{1 + f_{\text{EW}}}\end{aligned} \tag{2.1}$$

where N_{data} is the number of selected events, f_{EW} the fraction of electroweak background with respect to the number of $W \to \mu\nu$ events and f_{QCD} and f_{IFD} the fraction of QCD and in-flight decay background with respect to the number of selected events. ϵ is the overall efficiency for $W \to \mu\nu$ events and $\mathcal{L}$ the integrated luminosity.

The relevant numbers to compute the cross section with the above formula are summarized in Table 2.2 for the two selected triggers.

	wide trigger	'all' region
N_{data}	33126	29159
ϵ	18.95%	21.57%
f_{EW}	6.7%	7.0%
f_{IFD}	0.25%	0.25%
f_{QCD}	0.7%	0.8%
$\mathcal{L}$	53.7 pb^{-1}	41.9 pb^{-1}
$\sigma(p\overline{p} \to WX)\mathcal{B}(W \to \mu\nu)$	3020 pb	2984 pb

Table 2.2 – Summary of the number relevant to compute the inclusive $W \to \mu\nu$ production cross section

The main systematic uncertainties on this measurement come from variations of the result observed when varying the kinematic cuts of the selection (muon p_T, $\not{E}_T$ and M_T) for the wide trigger : 2.5%, from the modeling of the muon veto (difference when vetoing just on extra muons or just on extra tracks) : 1.5%, from the PDF uncertainties : 1.4%, from the uncertainty on the isolation efficiency measurement : 0.9% and from the limited $Z \to \mu\mu$ statistics in the efficiency computation : 0.9%.

After the release of the 2005 preliminary result, the variation with the selection cuts has been partly traced back to a bug in the implementation of the τ decays in Pythia [12] through Tauola [13]. The observed changes when applying different types of veto have been understood to come from an inconsistency in the treatment of the trigger efficiencies in the fast MC simulation for events with several muons like in $Z \to \mu\mu$ events.

The cross section results for the two selected triggers and for the combination of the two are then :

$$\begin{aligned}\text{wide trigger} : \sigma(p\overline{p} \to WX)\mathcal{B}(W \to \mu\nu) &= 3020 \pm 16(\text{stat}) \pm 114(\text{syst}) \pm 196(\text{lumi})\ \text{pb}; \\ \text{all trigger} : \sigma(p\overline{p} \to WX)\mathcal{B}(W \to \mu\nu) &= 2984 \pm 17(\text{stat}) \pm 81(\text{syst}) \pm 194(\text{lumi})\ \text{pb}; \\ \text{combination} : \sigma(p\overline{p} \to WX)\mathcal{B}(W \to \mu\nu) &= 2989 \pm 15(\text{stat}) \pm 80(\text{syst}) \pm 194(\text{lumi})\ \text{pb}.\end{aligned}$$

Figure 2.10 summarizes the measurement of the W and Z cross sections at the Tevatron. Some distributions comparing the data and the expected signal and backgrounds are shown in Figure 2.11 for the 'all' trigger.

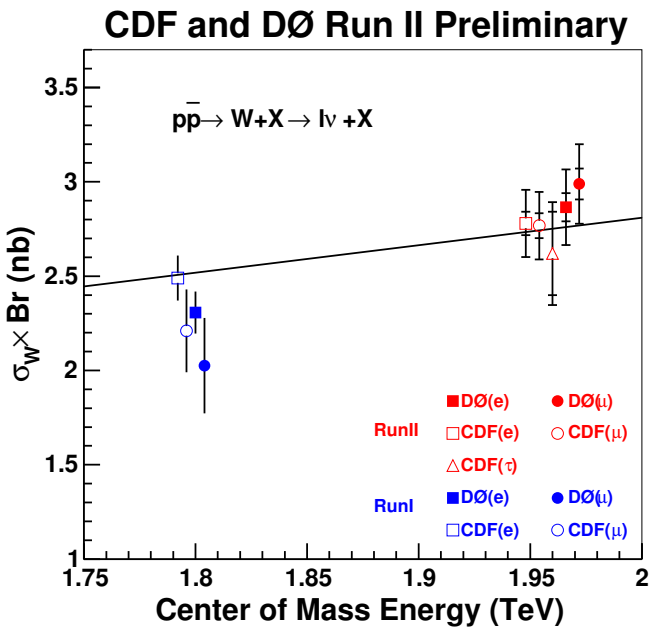

FIGURE 2.10 – Summary of the W and Z cross section measurements at the Tevatron.

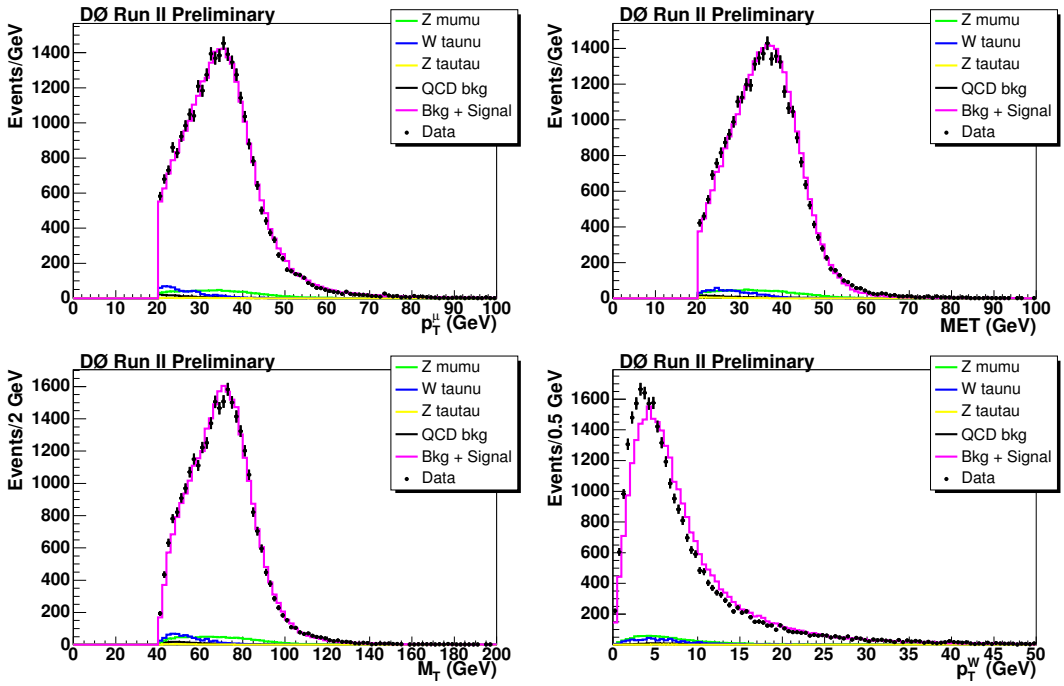

FIGURE 2.11 – Comparisons between data and expected signal + background for the muon p_T,$\not{E}_T$, M_T and the p_T of the W boson for the 'all' trigger.

2.6 Conclusion

The analysis reported here remains the latest official DØ measurement of the $W \to \mu\nu$ production cross section. Even if several improvements have been carried out after it was released as a preliminary result (see the remarks about the systematic uncertainties above) it has never been brought to publication. This is partly due to manpower availability and mainly due to the fact that at the end of 2005, DØ decided to re-calibrate its luminosity detector which leads to a decrease of the DØ measured luminosity by about 12 to 15% depending on the data samples [14]. Taking these changes into account, the combined measurement above can be reevaluated [4] :

$$\sigma(p\overline{p} \to WX)\mathcal{B}(W \to \mu\nu) = 2741 \pm 13(\text{stat}) \pm 60(\text{syst}) \pm 167(\text{lumi}) \text{ pb}$$

in agreement at the level of 0.8σ with the theoretical predictions of $\sigma = 2590 \pm 107$ pb computed with [15] and CTEQ6.1 [16].

Even if this result was never published, it helped setting the tools that have been further developped later in order to handle all the necessary efficiencies and to achieve good agreements between collider data and the MC simulation now in place at DØ.

Chapter 3

A Partial Top View

Contents

3.1 Top Quark Physics Using $t\bar{t}$ Events 46

3.1.1 Introduction to Top Quark Physics at the Tevatron 46

3.1.2 $t\bar{t}$ Event Selection Criteria 48

3.1.3 Background Processes 48

3.1.4 Sources of Systematic Uncertainty 49

3.2 Top Quark as Window to New Physics 52

3.3 $t\bar{t}$ Production Cross Section 53

3.3.1 Theoretical Computations 53

3.3.2 $t\bar{t}$ Cross Section Measurements in the Dilepton Channel 54

3.3.3 $t\bar{t}$ Cross Section Combination 65

3.3.4 Ratio of $t\bar{t}$ Cross Sections 66

3.4 Some Top Quark Properties 69

3.4.1 Top Quark Mass 69

3.4.2 $t\bar{t}$ Charge Asymmetry 86

3.5 Conclusion and Perspectives 92

After the work on the measurement of the inclusive $W \to \mu\nu_\mu$ cross section, I started to work on top quark physics in 2005. With other colleagues from Saclay, I mainly focused on studying the dilepton channel, which became the expertise of the Saclay group. I was convener of the DØ dilepton top quark subgroup from 2007 to 2008, and then convener of the whole DØ top group from 2008 to 2011. Since then, I am one of the DØ representative in the Tevatron top combination group.

In this chapter, I will give a short overview of top quark physics at the Tevatron and focus on some of the publications I worked on together with my students and postdoc : the measurement of the $t\bar{t}$ production in the dilepton channel and cross section ratios, the measurement of the dilepton top quark mass using the matrix element method, the determination of the top quark mass from the $t\bar{t}$ cross section at DØ and ATLAS, the combination of the top quark mass measurements at the Tevatron and the measurement of top-antitop charge asymmetry at DØ and ATLAS. Some parts of this chapter will be extracted from the review paper on $t\bar{t}$ physics at the Tevatron I wrote for Review of Modern Physics [17] with D. Glenzinski from CDF. These parts are materialized using a different text font in this chapter.

3.1 Top Quark Physics Using $t\bar{t}$ Events

3.1.1 Introduction to Top Quark Physics at the Tevatron

The Standard Model of particle physics (SM) contains six quarks arranged in three generations of two quarks each. The six leptons of the SM are similarly arranged. The top quark is the weak-isospin partner to the bottom quark, which together constitute the third generation of quarks.

The bottom quark was discovered in 1977 [18] and the search for its weak-isospin partner began in earnest. It was nearly two decades before the top quark was directly observed by experiment [19, 20, 21] owing to its surprisingly large mass. Of course the immediate consequence of this discovery was to further solidify the SM. Indeed, by the time the direct observation was made there was mounting indirect evidence that the top quark existed and that it had to be heavy [22]. But it could be argued that this indirect evidence was model dependent and that an important consequence of the top-quark discovery was the definitive elimination of "top-less" theories that might otherwise still be viable. In fact, the principal interest in the top quark arises because of the possibility it will offer a window into new physics, into physics Beyond the Standard Model (BSM). Thanks to its very large mass (it weighs about as much as a gold atom) BSM contributions to physics involving top quarks can occur in a wide variety of ways - the production mechanisms can be affected, the decay widths can be altered, its intrinsic properties changed, or the experimental signature mimicked by a new particle of similar mass. A thorough exploration of all these possibilities is what constitutes the field of "Top Quark Physics", pioneered over the last 15 years by the experiments at the Fermilab Tevatron.

From 1989-2009 top quarks could only be produced at one place in the world. The Tevatron is a proton (p) anti-proton ($\overline{p}$) collider with a center-of-mass energy of $\sqrt{s} = 1.96$ TeV located at Fermilab. For $p\overline{p}$ collisions at this energy top quarks are predominantly produced in pairs ($t\bar{t}$) via the strong interaction as shown in Fig. 3.1. The LHC is now the world largest energy collider with pp collisions at a center-of-mass energy of $\sqrt{s} = 7$ TeV in 2011.

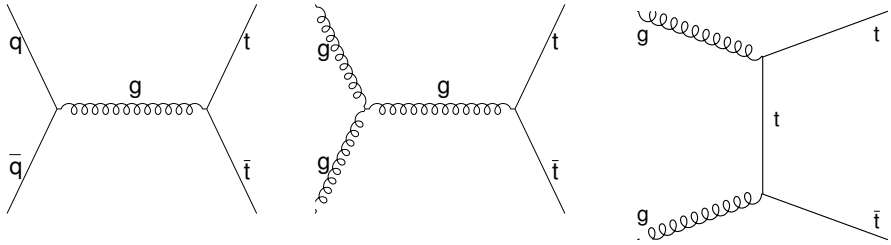

FIGURE 3.1 – Feynman diagrams of $p\overline{p} \to t\overline{t}$ for the $q\overline{q}$ annihilation process (left) and the gluon-gluon fusion process (middle and right).

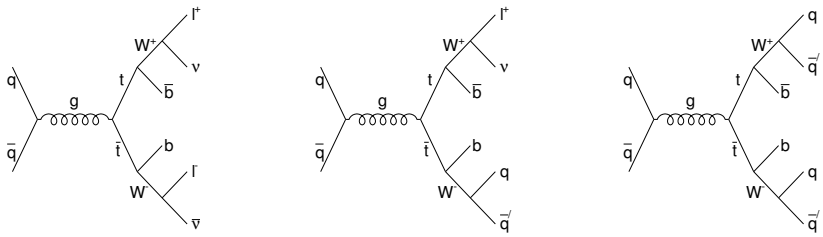

FIGURE 3.2 – Feynman diagrams of $p\overline{p} \to t\overline{t}$ production with the $t\overline{t}$ decaying to the dilepton (left), lepton-plus-jets (middle), and all hadronic (right) final states.

In the SM the top-quark decay is well specified and the branching fraction is completely dominated by $t \to W^+b$ with the decays $t \to W^+q$ ($q = s,\ d$) contributing at the $< 1\%$ level. Thus for $t\overline{t}$ events the experimental final state is determined by the decay of the W bosons. The leptonic decays ($l = e,\ \mu,\ \tau$) of the W boson have a branching fraction of $\mathcal{B}(W \to l\nu) = 10.8\%$ each while the hadronic decays have a total branching fraction of $\mathcal{B}(W \to q\overline{q}') = 67.7\%$ [23]. For $t\overline{t}$ events there are then three possible final states. The dilepton final state (dil) corresponds to both W bosons decaying leptonically, $t\overline{t} \to \ell^+\nu b\ell^-\overline{\nu}\overline{b}$, and occurs 10% of the time. The lepton-plus-jets final state (ljt) corresponds to one W decaying leptonically and the other hadronically, $t\overline{t} \to \ell\nu qq'b\overline{b}$, and occurs 44% of the time. The all hadronic final state (had) corresponds to both W bosons decaying hadronically, $t\overline{t} \to qq'bqq'\overline{b}$, and occurs 46% of the time. Figure 3.2 shows the Feynman diagrams corresponding to these three final states at the Tevatron, which, experimentally, are treated separately since the contributing sources of background and the dominant detector effects differ among them.

The decay width of the top quark is also well specified in the SM. Including radiative QCD and QED corrections the decay width for a top-quark mass of 172 GeV is $\Gamma_t = 1.4$ GeV [24, 25]. The theoretical uncertainty is at the level of a few percent relative and is dominated by uncertainties in α_s and in missing higher order QCD corrections. The large decay width of the top quark has important experimental consequences. Since Γ_t is large relative to the hadronization scale of QCD, $\lambda_{QCD} = 250$ MeV, the top quark decays before quark/anti-quark bound states are formed. Essentially, the top quark is produced and decays as a free quark - it is unique among the quarks in this respect. As a result of this unique feature, many of the experimental techniques used to explore the properties of the lighter quarks are not useful in exploring the top quark so that new methodologies had to be developed.

3.1.2 $t\bar{t}$ Event Selection Criteria

After the full reconstruction software has been run either at the Tevatron or at the LHC, the following event selection criteria are employed to identify a sample of candidate $t\bar{t}$ dil, ljt, and had events. The three samples are statistically independent by construction. Only the dil channel will be described here since this is the final state I mostly worked on.

The selection of dil events begins by requiring a pair of high energy leptons, e^+e^-, $\mu^+\mu^-$, or $e^\pm\mu^\mp$, with $E_T^{\rm lept}$ exceeding a value around 20 GeV. Several lepton selection criteria categories are usually employed ranging from "tight", which yield a very pure sample of leptons, to "loose", which can significantly increase the acceptance but with hadron mis-identification rates that are significantly higher. The leptons are required to be isolated. Backgrounds from $Z^0 \to e^+e^-$ and $Z^0 \to \mu^+\mu^-$ events are removed by vetoing events for which the two leptons yield an invariant mass consistent with the mass of the Z-boson. The events are also required to have a large missing transverse energy, $\not{E}_T > 20 - 25$ GeV, and at least two jets with $E_T^{\rm jet} > 15 - 20$ GeV (after correcting to the particle level) and $|\eta| < 2.0 - 2.5$. To remove backgrounds from semi-leptonically decaying b-jets the lepton-lepton invariant mass is required to be larger than 5 GeV. If an e^+e^- event is consistent with having originated from a photon conversion in material, or a $\mu^+\mu^-$ event is consistent with a through going cosmic ray event, they are vetoed. Except for special cases, events with 0 or 1 reconstructed jet are used as background dominated control regions to verify the accuracy of the background estimates. The total acceptance times branching fraction achieved is typically around 0.8% with a purity of around $70 - 75\%$. If a requirement that at least one of the jets is identified as a b-jet the acceptance times efficiency falls to about 0.5% and the purity rises to about $90 - 95\%$.

All the dil analyses described below begin by using the samples obtained after employing this event selection. Often, depending on the analysis, additional criteria are used to further improve the $t\bar{t}$ purity of the sample. A variety of methodologies are employed to account for the remaining background contributions as described in the next section.

3.1.3 Background Processes

After all selection criteria, background events still remain and must be accounted for in order to extract the $t\bar{t}$ physics parameters of interest. A variety of background processes contribute to each $t\bar{t}$ final state and fall into two basic categories : physics backgrounds and instrumental backgrounds. Physics backgrounds are those processes that share the same final state as the $t\bar{t}$ signal sample we are aiming to isolate. For example, the $p\bar{p} \to Z + q\bar{q}$ process, with the Z decaying to e^+e^- or $\mu^+\mu^-$, is a physics background to the $t\bar{t} \to \ell^+\nu b\ell^-\bar{\nu}\bar{b}$ sample. Instrumental backgrounds are those processes which mimic the $t\bar{t}$ final state of interest due to an instrumental effect resulting in a mis-identification of some of the final state objects. For example, the $p\bar{p} \to W + b\bar{b}q\bar{q}$ process, with the W decaying to $e\bar{\nu}$ or $\mu\bar{\nu}$, is an instrumental background to the $t\bar{t} \to \ell^+\nu b\ell^-\bar{\nu}\bar{b}$ sample when one of the jets is mis-identified as a high energy lepton. Although the mis-identification rates are typically very small, $< 1\%$, the instrumental backgrounds can still significantly contribute to the final selected samples due to the very large production cross sections for the relevant QCD process. In general, the acceptances for physics backgrounds are estimated using Monte Carlo simulations, while the instrumental backgrounds are estimated using data control samples. For background processes making small contributions to the final sample, or with

well understood theoretical cross sections, the normalization is taken from theory calculations. For all other cases the normalization is taken from the data using background dominated control samples and then extrapolated to the final signal sample.

The $Z/\gamma+$ jets process has a production cross section about four orders of magnitude greater than the $t\bar{t}$ process. This is potentially an important background in the dil channel since Z^0/γ^* decays to e^+e^- or $\mu^+\mu^-$ yield two high energy isolated leptons. However to survive the full selection criteria the $\not\!\!E_T$ must be mis-measured. For the $e\mu$ final state, the only significant contributions arises from Z^0/γ^* decays to $\tau^+\tau^-$ with the subsequent decay of the two τ leptons to $\tau^\pm \to e^\pm\nu_\tau\overline{\nu_e}$ or $\tau^\pm \to \mu^\pm\nu_\tau\overline{\nu_\mu}$ in order to generate two light leptons and survive the selection criteria. If b-jet identification is required, the relevant efficiency and mis-identification rates are taken from data control samples and applied to the surviving Monte Carlo events. The $Z/\gamma+$ jets production rate is normalized to theoretical predictions calculated to next-to-next-to-leading order.

The QCD processes $p\overline{p} \to \text{jets}$ have a production cross section that is about 9 orders of magnitude larger than the $t\bar{t}$ production cross section. The jets produced predominantly originate from uds-quarks or gluons, although b-quark jets are produced in a few percent of these events. For the $t\bar{t} \to \ell^+\nu b\ell^-\overline{\nu}\overline{b}$ final state the QCD background is small since two jets would need to be mis-identified as an isolated high energy lepton and the $\not\!\!E_T$ would have to be mis-measured. If b-jet identification is required, a further mis-identification of one of the $udsg$-jets is also necessary in order for the event to survive all selection criteria. All these fake rates are taken from data control samples and then applied on the signal sample in order to estimate the contribution of this background to the final selected sample. There are large uncertainties associated with this background which arise from the relatively low statistics of surviving events in the control samples once the identification criteria are applied (i.e. because the mis-identification rates are quite small) and from systematic uncertainties accounting for kinematic differences between the control samples and the signal sample.

The diboson processes $p\overline{p} \to VV$ ($V = W^\pm$, Z^0, or γ) have production cross sections within a factor of two of the $t\bar{t}$ cross section. When the $W^\pm$ and/or Z^0/γ bosons decay leptonically these processes make contributions to the dilepton samples. These are physics backgrounds whose estimates are taken from Monte Carlo and normalized to theoretical predictions calculated to next-to-leading order. If b-jet identification is required, the relevant efficiency and mis-identification rates are taken from data control samples and applied to the Monte Carlo.

The production of a single top quark via the electroweak interaction, $p\overline{p} \to tq$, has a production cross section about a factor of two smaller than the $t\bar{t}$ cross section and makes a small contribution to the $t\bar{t} \to \ell^+\nu b\ell^-\overline{\nu}\overline{b}$ final state. It is a physics background and is estimated using Monte Carlo samples normalized to the theory predicted cross section.

3.1.4 Sources of Systematic Uncertainty

Variety of systematic uncertainties are evaluated for each of the $t\bar{t}$ analyses. They fall into three general categories : uncertainties associated with the background modeling, uncertainties associated with the signal modeling, and uncertainties associated with the methodology employed to extract the physics parameter(s) of interest. The sources of uncertainty affecting the signal and background modeling and the methods employed in evaluating them, are common across all the $t\bar{t}$ analyses and are summarized here.

Systematic Uncertainties Associated with Background Processes

The systematic uncertainties affecting the background modeling include instrumental effects related with the various mis-identification rates required to promote a background physics process into the signal region, theory related uncertainties such as variations of the factorization and renormalization scales, k-factors related to NLO corrections, and differences in parton shower and fragmentation modeling, as well as uncertainties in normalization arising from uncertainties in lepton, b-quark jet, etc. identification efficiencies. Several sources of uncertainty affect multiple background processes and their effects are accounted for in the analyses in a correlated manner.

The mis-identification rate for hadrons faking an electron or muon signature and for $udsg$-jets faking a b-jet are derived from data control samples. The mis-identification rates are parameterized by an empirically determined functional form, which includes the dependence of the rate on relevant kinematic variables (e.g. jet E_T or $|\eta|$). The validity of the parameterization is tested using statistically independent data control samples. Differences between the predicted rate, as determined using the parameterization, and the observed rate are used to assign systematic uncertainties on the mis-identification rates themselves. These uncertainties are then propagated to the number of predicted background events for those background processes for which the relevant mis-identification is required in order for that process to mimic a $t\bar{t}$ signal event. Since these mis-identification rates depend on the kinematics of the events, they also introduce a systematic uncertainty on the shape of the resulting kinematic distributions of background events surviving the full event selection criteria. These "shape" systematics are usually evaluated by re-weighting the relevant kinematic distributions using the mis-identification parameterizations varied by $\pm 1\sigma$.

Most all of the Monte Carlo samples employed in the analyses described here are based on leading order theory calculations. The inclusion of higher order corrections affect the predicted production cross section for the various background processes. These effects are accounted for in the analysis either by normalizing the Monte Carlo yields to next-to-leading order calculations, or by normalizing to the data itself. Some residual higher-order effects still remain.

The electron and muon identification efficiencies, the relevant trigger efficiencies, and the b-quark jet identification efficiencies all have associated statistical and systematic uncertainties. These uncertainties are propagated through each of the affected background processes by varying each in turn by $\pm 1\sigma$. These variations result in uncertainties on the number of contributing events for the affected background processes. For those efficiencies that have a kinematic dependence, their effect on resulting kinematic distributions is also evaluated by re-weighting the affected distributions using parameterizations that bracket the $\pm 1\sigma$ variations of the relevant kinematic dependencies.

The uncertainty on the jet energy scale is propagated by varying the parameterized jet energy corrections by $\pm 1\sigma$ and re-evaluating the predicted number of background events and the resulting kinematic distributions. This uncertainty affects all the MC-evaluated background processes.

The total uncertainty on the predicted background events is the quadrature sum of these various sources.

Systematic Uncertainties Associated with $t\bar{t}$ Modeling

The systematic uncertainties affecting the modeling of $t\bar{t}$ production and decay include variations of initial and final state radiation, variations in the parton distribution functions, variations in

the parton shower and fragmentation modeling, variations in the modeling of color reconnection effects in final state interactions between the t and $\bar{t}$ decay products, and uncertainties associated with the trigger, lepton identification, and b-jet identification efficiencies. Some of these sources of uncertainty also affect background processes and their effects are accounted for in the analyses in a correlated manner.

Uncertainties in the modeling of initial state radiation (ISR) and final state radiation (FSR) are evaluated by generating $t\bar{t}$ Monte Carlo samples with their ISR and/or FSR parameters varied by $\pm 1\sigma$ relative to the default sample. The range of variation which defines "1σ" is determined using $p\bar{p} \rightarrow Z^*/\gamma^* \rightarrow \mu^+\mu-$ samples. Like $t\bar{t}$ production at the Tevatron, this process is dominated by $q\bar{q}$ annihilation. The $p_T^{\mu^+\mu^-}$ and the N_{jet} distributions are used to constrain the parameters in the Monte Carlo affecting the ISR modeling. The constraints are derived in bins of $M^2_{\mu\mu}$ and extrapolated to $M^2_{\mu\mu} = 4M_t^2$. Since the ISR and FSR processes in the Monte Carlos are both modeled using DGLAP evolution, the same variations are used to assign systematics for FSR. Samples are produced varying ISR only, FSR only, and ISR/FSR simultaneously. The sample resulting in the largest difference relative to the nominal sample is used to assign the associated systematic uncertainty.

The parton distribution functions result from multi-dimensional fits to dozens of measurements made by a variety of different experiments. The CTEQ and MRST collaborations provide eigenvectors representing $\pm 1\sigma$ variations of 20 uncorrelated parameters affecting the resulting PDFs. The difference associated with each variation is evaluated by reweighing the $t\bar{t}$ events in the nominal Monte Carlo sample using each eigenvector in turn. The $+1\sigma$ and -1σ variations are quadratically summed separately.

The signal $t\bar{t}$ samples are generated with several different Monte Carlo generators. For those Monte Carlo samples which reasonably model the observed data distributions, the $t\bar{t}$ yields and kinematic distributions are evaluated in full. Differences between the nominal Monte Carlo sample and any viable alternative sample are assigned as systematic uncertainties. This systematic primarily accounts for differences in parton shower and fragmentation modeling but also includes possible effects from differences in the modeling of the $t\bar{t}$ p_T spectrum, $t\bar{t}$ spin correlations, and final state radiation.

Since top-quarks and W-bosons decay quickly relative to the timescale associated with the parton shower and fragmentation processes (i.e. $1/\Gamma_t$, $1/\Gamma_W << 1/\lambda_{QCD}$) it is possible that the products from the different top-quark decays could interact with each other via color reconnections. By default, all Monte Carlo generators ignore such reconnections since they are non-existent or irrelevant for most processes. These color reconnection effects were first investigated at LEP2 (e.g. [26]). Since Tevatron's $p\bar{p}$ initial state carries the color charge, the situation and its modeling is significantly more complicated that at LEP, which used an e^+e^- initial state. Recently, Monte Carlo models providing an adequate description of Tevatron $p\bar{p}$ minimum bias and underlying events and including color reconnection effects have become available. The associated systematic uncertainty is evaluated by generating $t\bar{t}$ samples with these various color reconnection models enabled and comparing to the nominal Monte Carlo sample. Difference are assigned as systematic uncertainties.

The uncertainties associated with the electron and muon identification efficiencies, the relevant trigger efficiencies, the b-quark jet identification efficiencies, and the jet energy scale uncertainties are all evaluated in the manner described in the sub-section above. These uncertainties also affect some or all of the background processes. The resulting correlations are correctly accounted for in

the analyses.

The total uncertainty on the predicted $t\bar{t}$ yields and resulting kinematic shapes is the quadrature sum of these various sources. Correlations with the background processes are included.

3.2 Top Quark as Window to New Physics

It is important to note that the SM has several short comings and is widely regarded to be a low energy approximation of a more complete description of particle physics [27]. There are numerous theories hypothesized that address these shortcomings and offer this more complete description. The theories differ primarily in the manner by which they impart mass to the elementary particles. The search to discover and describe the physics that breaks electroweak symmetry is among the most ardently pursued by high energy experimentalists and theorists alike. Is it the SM Higgs, or is it some new physics, something beyond the SM ? The principal aim of top-quark physics is to help answer these questions. With a Yukawa coupling of order unity, the top quark strongly couples to the dynamics of electroweak symmetry breaking and is thus expected to be a good place to test this dynamics and probe for BSM effects. In addition, because of its large mass, quantum loop corrections to top-quark observables from possible new particle contributions can be large - significantly larger than for the lighter quarks and leptons. The strategy for probing for BSM effects using the top quark employs both direct searches for new particles and indirect searches by looking for deviations of experimental observables from the SM expectations.

New physics contributions can affect top-quark observables directly in two ways [28]. First non-standard top-quark production can appear through intermediate heavy states such as new gauge bosons that decay into a $t\bar{t}$ pair or into a final state mimicking the SM $t\bar{t}$ signature. Secondly the top quark can decay into exotic particles such as a charged Higgs boson, $t \to H^+b$, in models with multiple Higgs doublets. In the first case, BSM effects distort the SM top-quark production observables, while in the second case BSM effects produce discrepancies among the different decay observables. It is thus important to measure the top-quark properties using as many decay final states as possible and to compare them.

There are many examples of new physics models that affect the production or decay observables in $t\bar{t}$ samples. New heavy states that carry color charge can modify the $t\bar{t}$ production observables. Color singlet resonances can be either scalar or vector. Examples of models that predict color singlet scalar particles are the supersymmetric extension of the SM, SUSY [29, 30, 31, 32], or more generally models with multiple Higgs fields, MHDM [33]. Examples of models that predict color singlet vector particles include technicolor [34, 35], topcolor [36], or top assisted technicolor [37]. Color non-singlet resonances can produce similar effects and are also predicted in several BSM theories [38, 39, 40]. Compactified extra dimension models can also affect $t\bar{t}$ production and decay. These models produce Kaluza-Klein (KK) modes that either decay preferentially into $t\bar{t}$ pairs or into final states that mimic the SM $t\bar{t}$ signature. The flat extra dimension TeV^{-1} models produce KK modes that can decay to $t\bar{t}$ pairs [41, 42, 43, 44, 45, 46]. Universal extra dimension models pair produce a KK mode that each decay as $\mathrm{KK} \to t\gamma$ so that they mimic the SM signature but also include additional photons in the final state [47, 48, 49]. Warped Randall-Sundrum extra dimension models predict KK gravitons that can decay to $t\bar{t}$ [50, 51], while bulk Randall-Sundrum models with fermions and gauge bosons in the bulk predict in addition KK top quarks that would be produced in pairs and would decay to Wb as in the SM [52, 53, 54, 55, 56, 57, 58, 59, 60, 61].

Some BSM theories predict a fourth family of (heavy) quarks and leptons. These additional generations naturally appear in grand-unified theories [62] but some of the models cited above also predict new particles that look like heavier quarks. Similarly, Little Higgs models predict new heavy vector-like quarks [63, 64]. All of these can produce decay final states that mimic the SM $t\bar{t}$ signatures.

New physics effects can also effect top-quark decays or other properties of the $t\bar{t}$ sample. For example, some SUSY and MHDM theories produce top-quark decays into new particles [32, 33]. Other models modify the SM top-quark branching fractions. For example flavor changing neutral current (FCNC) decays, $t \to cX^0$, or $t \to uX^0$ where X^0 is any neutral particle like a photon or a Z-boson, can be modified by BSM physics. Since these processes are extremely suppressed in the SM even small new physics effects can yield large changes in FCNC branching fractions [65]. The $t\bar{t}$ sample can also be probed for the presence of more general anomalous couplings [66] affecting the kinematic properties of top-quark decays and appearing as discrepancies with the SM predictions. These might affect the $t\bar{t}$ forward-backward charge asymmetry, the $t\bar{t}$ spin correlations, or the helicity fractions of W-bosons from top-quark decays [67, 68, 69, 70]. The measured intrinsic properties of the top-quark might also be affected. For example some BSM theories predict particles with electric charge $-4/3$ or $+5/3$ that decay into top-quarks [71].

For the moment, no sign of BSM effects have been clearly established at the Tevatron and at the current LHC energy.

3.3 $t\bar{t}$ Production Cross Section

3.3.1 Theoretical Computations

The computation of the top-quark pair production cross section is based on factorization in QCD, which allow to write a generic hadronic cross section as a convolution of the partonic cross section $\hat{\sigma}_{ij}$ for the scattering partons i and j (quarks or gluons), with parton distribution functions (PDFs) $f_{i/j}(x, \mu_F)$ that describe the parton content of the colliding hadrons. The scale μ_F represents the factorization scale that splits the partonic process from the process-independent PDFs. Hence the inclusive top-quark pair production cross section at hadron colliders can be written as :

$$\sigma = \sum_{i,j \in q,\bar{q},g} \int dx_1 dx_2 f_i(x_1, \mu_F) f_j(x_2, \mu_F) \hat{\sigma}_{ij}(s, \mu_F, \mu_R) \tag{3.1}$$

where $x_{1/2}$ are the longitudinal momentum fractions of the incoming partons. The scale μ_R is the renormalization scale that drives the regularization of the partonic cross section at a given order in the perturbative expansion of the strong coupling constant $\alpha_s(\mu_R)$. In principle the computed cross section should be independent of μ_F and μ_R. However, when the infinite perturbative series are truncated at finite order, the results could have a non-negligible dependence on the scales. The values of these scales are often chosen to be equal to the top quark mass : $\mu_F = \mu_R = m_t$ The related uncertainties on the computation are typically evaluated by varying μ_F and μ_R by half or twice their values which should estimate the uncertainty coming from the series truncation. The other uncertainty on the theoretical computation comes from the errors on the PDFs.

At leading order (LO), the partonic cross section $\hat{\sigma}_{ij}$ can be computed from the matrix elements squared (averaged over the initial colors and spins and summed over the final colors and spins) : $\overline{\sum}\sigma_{ij}$. These can be found for instance in [72]. The LO cross section for $\sqrt{s} = 1.96$ TeV at the Tevatron is predicted to be around 6 pb with strong dependence on the choice of the scales. To make more reliable predictions, higher order computations have to be included.

The full next-to-leading order (NLO) calculation has been performed in [73, 74]. It increases the LO result by a factor of about 1.25. Although significantly reduced, the uncertainty coming from the renormalization and factorization scales on the NLO value are still of the order of 10 % slightly larger than the uncertainties coming from PDFs. No full next-to-next-to-leading order (NNLO) calculations exist for the moment. However some of the contributions of these higher-order terms can be calculated. Indeed it is possible to compute the sum of the leading logarithms corresponding to soft gluon emission at any perturbation order. The leading logarithm (LL) terms can typically be written in powers of : $\alpha_s \ln^2(\beta)$ where $\beta = \sqrt{1 - \frac{4m_t^2}{s}}$. The further subdominant terms (next-to-leading logarithms : NLL, next-to-next-to-leading logarithms : NNLL, ...) can also be computed. Since the logarithms are related to the fact that the gluon emission is soft at threshold, such resummations are called soft-gluon or threshold resummations. It can be that these leading terms in the soft limit give the largest contributions from the next order to the hadronic cross section, that is why they could be an improvement over the fixed order expansion. The real radiation in the soft limit can be resummed infinitively (NLO+(N)NLL) or we can use only the logarithmic corrections to a certain accuracy in the fixed-order expansion (approximate NNLO). These contributions can lead to a change of 5% on the central value of the $t\bar{t}$ cross section compared to the pure NLO result. They also allow to reduce the dependence due to the scale choices up to a factor of two as can be seen in Figure 3.3 which shows the variation of the cross section with the scales. Hence for these computations the scale uncertainties are smaller than the uncertainties coming from PDFs. The evolution in time of the theoretical uncertainty for some of these computations are shown in Figure 3.4. It has to be noticed however that soft-gluon resummation at NNLL brings only a minor decrease in the perturbative uncertainty with respect to the NLL resummation [75]. Significant improvements in the $t\bar{t}$ cross section could be expected only with the complete NNLO computation. It was also noticed in [75] that the choice of PDF sets could lead to about 5% difference in the prediction for the central cross section values. Such difference could be larger than the actually PDF uncertainties usually quoted. It was understood in the case of the use of MSTW2008nnlo68cl [76] versus NNPDF21_nnlo_nf5_100 [77] to be due to different choices for the value of the strong coupling constant.

Some of the latest total cross section computations at NLO and for various NNLO approximations are presented in Table 3.1 [85].

3.3.2 $t\bar{t}$ Cross Section Measurements in the Dilepton Channel

Measuring the $t\bar{t}$ production cross section is interesting for several reasons. First it allows for a precise test of the predictions from perturbative QCD. Computations of the $p\bar{p} \to t\bar{t}$ total rate are available at NLO and as well as several approximate NNLO computations, where the dominant (N)NLL terms are resummed as discussed in section 3.3.1. Comparing

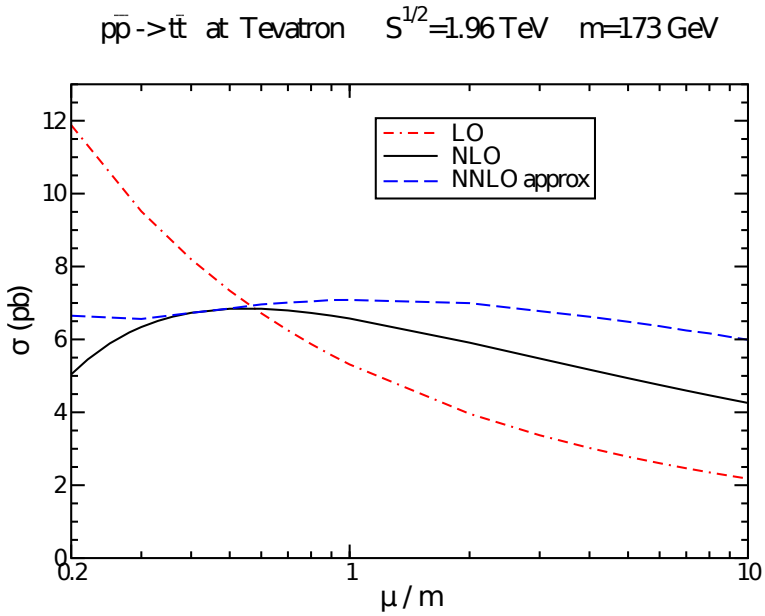

FIGURE 3.3 – Scale dependence of the $t\bar{t}$ cross section at the Tevatron for $m_t = 173$ GeV and $\mu_F = \mu_R = m_t$ [78].

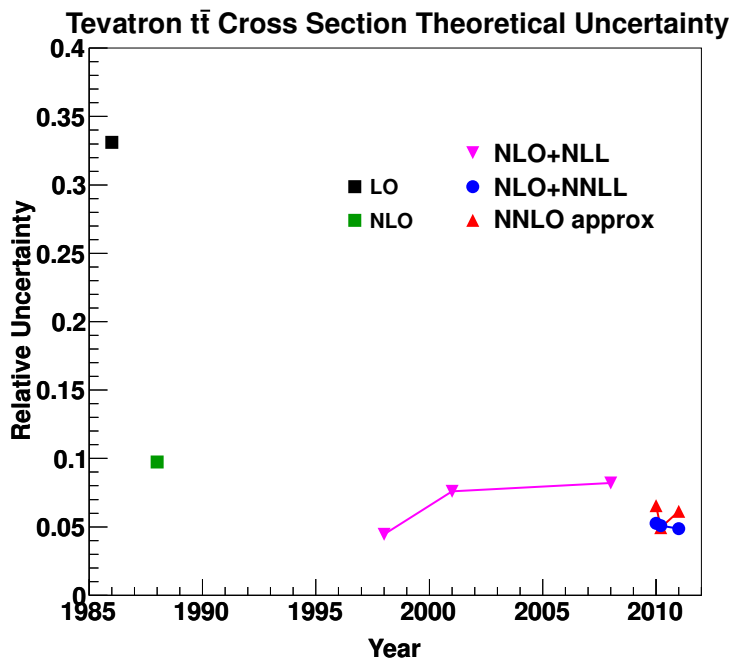

FIGURE 3.4 – Evolution in time of some of the theoretical uncertainty on the $t\bar{t}$ cross section for different theoretical accuracy [79, 80, 81, 82, 78, 83, 84, 75]. The quoted relative uncertainty contains both the scale uncertainty and the uncertainty on the PDF. The time stamp for the leading order (LO) cross section is irrelevant.

the measurements with the predictions is important since various BSM theories postulate new

	$\sigma_{t\bar{t}}$ (in pb)
NLO	$6.74^{+0.36\ +0.37}_{-0.76\ -0.24}$
Aliev et. al [83]	$7.13^{+0.31\ +0.36}_{-0.39\ -0.26}$
Kidonakis [78]	$7.08^{+0.00\ +0.36}_{-0.24\ -0.24}$
Ahrens et al. [84]	$6.65^{+0.08\ +0.33}_{-0.41\ -0.24}$

TABLE 3.1 – Some of the latest total cross section computations at NLO and for various NNLO approximations for $m_t = 173$ GeV. The first uncertainty is coming from the perturbative uncertainties while the second comes from the PDF error using MSTW2008 [76] at 90 % CL.

particles that couple preferentially to the top quark and thus predict a higher $t\bar{t}$ production rate. A typical example is the production of new resonant particles that decay into $t\bar{t}$ [86]. Examples of constraints from $t\bar{t}$ cross section measurements will be given in section 3.3.4.

It is also particularly important to measure the production cross section in different top-quark decay channels since new physics contributions can affect the various $t\bar{t}$ final states differently. Examples of such models are Two Higgs Doublet Models among which are SUSY models [33, 32] predicting the existence of charged Higgs bosons, $H^{\pm}$. If such a charged Higgs boson is light enough ($m_{H+} < m_t - m_b$), the decay $t \to H^+b$ can compete with the SM decay $t \to Wb$; the measured $t\bar{t}$ production rate will then differ among the various final states due to contributions from charged Higgs decays (see section 3.3.4).

To make precise measurements of the $t\bar{t}$ production cross section requires a good understanding of the reconstruction and identification efficiencies as well as a careful evaluation of the background processes that mimic the $t\bar{t}$ signal. Because of this, the cross section analysis also then serves as a foundation on which most the rest of the $t\bar{t}$ analyses are built. The $t\bar{t}$ cross section measurement is performed by evaluating the following formula :

$$\sigma_{t\bar{t}} = \frac{N_o - N_b}{\epsilon_{t\bar{t}} \mathcal{B} \int \mathcal{L} dt} \tag{3.2}$$

where N_o is the observed number of events after selection, N_b is the estimated mean number of background events, $\epsilon_{t\bar{t}}$ is the signal efficiency evaluated using $t\bar{t}$ Monte Carlo, $\mathcal{B}$ is the relevant final-state-dependent $t\bar{t}$ branching fraction, and $\int \mathcal{L} dt$ is the integrated luminosity for the particular set of triggers used for the measurement. It is worth noting that since $\epsilon_{t\bar{t}}$ is increasing with the top-quark mass the measured cross section is quoted at a given m_t. The numerator in Eq. 3.2 can be evaluated either using event counting after applying the final selection criteria or by fitting a discriminant variable that separates signal and background to estimate the relative contributions of each to the surviving event sample. The use of b-tagging is helpful to discriminate $t\bar{t}$ signal from background.

In the dil channel both W bosons decay to leptons. The event then contains two high E_T isolated leptons, large $\not{E}_T$, and two b-jets. This channel is often sub-divided further according to the explicit lepton identification criteria employed. When both leptons are reconstructed as an electron or muon the sample is dominated by $t \to Wb \to e\nu b$ and $t \to Wb \to \mu\nu b$ decays ($\ell\ell$ channel). The acceptance can be significantly increased, particularly for $Wb \to \tau\nu \to h\nu\nu\nu$

decays, by applying very loose criteria for one of the lepton legs (ℓtrk). Measurements have also been performed in the final state with a τ lepton decaying into hadrons explicitly identified from the decay of one W boson and an accompanying electron or muon from the other W boson decay ($\ell\tau$ channel). In general the dil channel has the advantage of a good signal to background ratio even without using b-tagging but suffers from a smaller branching fraction than the ljt or had channels.

In the dil channel, the main source of background comes from the production of electroweak bosons that decay to charged leptons. For the $\ell\ell$ channel, it arises from Drell-Yan processes, $Z/\gamma^* \to \ell^+\ell^-$, and diboson processes when the bosons decays lead to at least two leptons in the final state. These backgrounds are reduced by requiring ≥ 2 jets and large $\not\!\!E_T$. The Z/γ^*+jets and diboson backgrounds are evaluated using MC normalized to (N)NLO theory cross sections. The QCD backgrounds are evaluated using data. The jet-to-lepton fake rates are computed in a background dominated sample orthogonal to the signal sample (QCD di-jets, $\gamma + jets$, same sign dilepton samples). By applying b-jet identification a very pure $t\bar{t}$ sample can be identified.

As it benefits from a favorable signal to background ratio, the $t\bar{t}$ dilepton selection, at least in the case of two well identified leptons, relies on a small number of simple requirements. Selecting $t\bar{t}$ events decaying to dilepton requires first an inclusive lepton trigger, two high p_T isolated electrons or muons (typically with $p_T > 20$ GeV) or one isolated electron or muon and one isolated high p_T track and generally at least two jets with $p_T > 20$ GeV. Large $\not\!\!E_T$ is further required (typically $\not\!\!E_T > 25$ to 35 GeV). The $\not\!\!E_T$ threshold is raised if the dilepton invariant mass is in the range of the Z resonance. Other topological cuts sometimes replace the $\not\!\!E_T$ requirement particularly for the $e\mu$ channel since it suffers from the Drell-Yan process only through double leptonic τ decays of $Z/\gamma^* \to \tau^+\tau^-$. In the $\ell\ell$ channel, the signal-to-background ratio after all selection criteria is about 3 :1 prior to and $15:1$ after requiring at least one b-jet in the event.

Dilepton $t\bar{t}$ Cross Section Measurements at DØ

DØ has published four measurements of the $t\bar{t}$ cross section in the dil channel, in 2005 with 0.23 fb^{-1} [87], in 2007 with 0.42 fb^{-1} [88], in 2009 with 1 fb^{-1} [89] and in 2011 with 5.4 fb^{-1} [90]. Together with my colleagues and students from Saclay, I have worked on all these analyses except the first one. The results of these measurements are presented in Table 3.2. The predicted and observed number of events are shown in Table 3.3 for the latest measurement using 5.4 fb^{-1}.

Several evolutions and improvements have been carried out not only as the statistics of the analyzed dataset increased but also thanks to a better understanding of the collected data and improvements in the MC modeling. The most important changes are discussed below.

The first DØ measurement [87] used a limited statistics of 0.23 fb^{-1} observing 13 dilepton events after selection with an expected background of 3.2 ± 0.7 events. The significance of the observed $t\bar{t}$ signal over the background was 3.8 standard deviation. In this analysis the contribution from instrumental background coming from jets faking electron or containing prompt lepton decays was evaluated by computing the fraction of loose electron or muon which appears tight in control sample dominated by fake leptons. A loose electron is typically an electron without requirement of track matching to the calorimeter electromagnetic (EM) cluster. A loose muon is typically a muon without any isolation requirements. The control

Luminosity (fb^{-1})	$\sigma_{t\bar{t}}$ (in pb)				total error	$\frac{S}{\sqrt{S+B}}$	reference
0.23	8.8	$^{+3.3}_{-2.8}$ (stat)	$^{+1.1}_{-1.1}$ (syst)	± 0.6 (lumi)	$^{+3.5}_{-3.0}$: 37%	0.9	[87]
0.42*	7.7	± 1.4 (stat)	± 0.9 (syst)	± 0.6 (lumi)	± 1.8 : 23%	4.1	[88]
1.0**	7.4	± 1.0 (stat)	$^{+0.7}_{-0.6}$ (syst)	$^{+0.6}_{-0.5}$ (lumi)	$^{+1.3}_{-1.2}$: 17%	6.9	[89]
5.4	7.36				$^{+0.90}_{-0.79}$: 11%	14.3	[90]

TABLE 3.2 – DØ measurements of the $t\bar{t}$ cross section in the dilepton channel. Except for the latest measurement, the published results have been rescaled to $m_t = 172.5$ GeV. S represents the number of expected $t\bar{t}$ events and B the number of expected background. (*) also includes events with one lepton and a track. (**) also includes the $\ell\tau$ channel.

Channel	$Z \to \ell\ell$	Diboson	Instrumental back-ground	$t\bar{t} \to \ell\bar{\ell}b\bar{b}\nu\bar{\nu}$	N_{exp}	N_{obs}	$\frac{\text{Observed}}{\text{Expected}}$
ee+2jet	12.6 ± 2.0	3.0 ± 0.4	-	45.6 ± 5.3	61.1 ± 7.1	74	1.21 ± 0.20
$\mu\mu$+2jet	67.3 ± 9.7	5.1 ± 0.7	7.6 ± 1.2	59.8 ± 6.6	139.8 ± 15.7	144	1.03 ± 0.14
$e\mu$+2jet	30.3 ± 4.2	8.6 ± 1.2	22.7 ± 8.6	191.5 ± 18.8	253.1 ± 24.3	281	1.11 ± 0.13
$e\mu$+1jet	40.9 ± 4.8	20.7 ± 2.4	25.3 ± 10.5	52.1 ± 9.4	139.0 ± 16.5	150	1.08 ± 0.16

TABLE 3.3 – Numbers of expected and observed events for DØ $t\bar{t}$ cross section measurement in the *dil* channel using 5.4 fb^{-1} [90] assuming the SM $t\bar{t}$ cross section for a top quark mass of $m_t = 172.5$ GeV (7.45 pb). Expected numbers of events are shown with their systematic uncertainties. The uncertainty on the ratio between observed and expected numbers of events takes into account the statistical uncertainty in the observed number of events (N_{obs}) and the systematic uncertainty in the expected number of events (N_{exp}).

samples to measure the lepton fake fraction were data samples with low $\not\!\!E_T$ or dimuon events with one non-isolated tag muon.

The measurement using 0.42 fb^{-1} [88] also included events where one of the lepton is only identified with a charged track ($\ell+$trk channel) requiring in addition one jet to be b-tagged. The analysis used a new method to determine the fake electron background in the $e\mu$ channel. Indeed, in addition to requirements on the energy, isolation, longitudinal and lateral shower profiles of the EM clusters, electron were identified using a electron likelihood formed from several variables. These variables included the fraction of cluster energy deposited in the EM layers of the calorimeter, the ratio of calorimeter transverse energy to track transverse momentum, the quality of the spatial matching between the central track and the EM cluster, the distance of closest approach of the track to the primary vertex, the number of tracks in a $\Delta R = 0.05$ cone, and the sum of the transverse momenta of all tracks in a cone of size $\Delta R = 0.4$ around the EM-associated track. For each discriminating variable x_i, these distributions provided probabilities $P^i_{\text{sig}}(x_i)$ and $P^i_{\text{bkg}}(x_i)$ for an EM object to be from a real and a fake electron, respectively. The following likelihood discriminant was used to distinguish between real electrons and fakes from hadronic objects :

$$\mathcal{L}_e(\mathbf{x}) = \frac{P_{\text{sig}}(\mathbf{x})}{P_{\text{sig}}(\mathbf{x}) + P_{\text{bkg}}(\mathbf{x})}, \tag{3.3}$$

where $\mathbf{x}$ is the vector of likelihood variables. The probabilities were formed disregarding the correlations between the likelihood variables, i.e.

$$P_{\text{sig/bkg}}(\mathbf{x}) = \prod_{i=1}^{7} P^i_{\text{sig/bkg}}(x_i). \tag{3.4}$$

Tight electron required that the above electron likelihood $\mathcal{L}_e$ is above 0.85. The efficiency of this cut on real electrons was estimated to be around 86 % in the central part of the calorimeter and 84 % in the forward/backward parts. Starting from the 0.42 fb^{-1} analysis, the background from fake electrons was estimated by performing an extended unbinned likelihood fit to the observed electron likelihood distribution in events passing all selection criteria using a likelihood given by [88] :

$$\mathcal{L} = \prod_{i=1}^{N} [n_e S(x_i) + n_{\text{fake}} B(x_i)] \frac{e^{-(n_e + n_{\text{fake}})}}{N!}, \tag{3.5}$$

where i is an index that runs over all selected events, x_i is the corresponding observed value of the electron likelihood, N is the total number of events, n_e is the number of events with signal-like electrons, n_{fake} is the number of events having fake electrons, and S and B are the signal and background probability distribution functions (pdf), respectively. The signal pdf S was measured in $Z/\gamma^\star \to ee$ data events. The background pdf B was determined using a data sample with low $\not\!\!E_T$ dominated by false electrons. The event counts n_e and n_{fake} were allowed to float in the fit. The total number of events with a jet misidentified as an electron is given by n_{fake} scaled for the integral of $B(x)$ over the region satisfying the likelihood requirement. Note that this fake electron estimate includes backgrounds containing both real and fake isolated muons. This method was further propagated to the fake evaluation in the ee channel starting from the analysis using 1 fb^{-1}.

The measurement using 1 fb^{-1} [89] which also included events with one electron or muon and one τ lepton with b-tagging requirement ($\ell\tau$ channel) included several addition improvements. First, changes in the event selection allowed to increase the signal acceptance to further reduce the statistical uncertainty on the measurement. The muon isolation has been loosened. Two isolation criteria are used to distinguish muons produced in top quark decays from those originated from hadronic decays. One variable is computed by summing over the charged tracks in a cone of $\Delta R = 0.5$ around the track associated with the muon excluding this track from the sum ($\mathcal{E}^{\rm trk}_{\rm cone}$). Another variable was derived from summing the calorimeter deposited energy in a halo cone of $0.1 < \Delta R < 0.4$ around extrapolated muon track ($\mathcal{E}^{\rm cal}_{\rm halo}$). Both sums are scaled by the muon transverse momentum (see section 1.1.2). The cut on these two isolation variables has been optimized from : $\mathcal{E}^{\rm trk}_{\rm cone} < 0.12$, $\mathcal{E}^{\rm cal}_{\rm halo} < 0.12$ to $\mathcal{E}^{\rm trk}_{\rm cone} < 0.15$, $\mathcal{E}^{\rm cal}_{\rm halo} < 0.15$ without significantly increasing the background from multijet production.

Another improvement in the acceptance was achieved by selecting events with only one high p_T jet in the clean $e\mu$ channel. Even if the background level in events with exactly one jet is high ($S/B \sim 1$), it allows to collect 25 % additionnal $t\bar{t}$ events compared to the two jet channel. In this channel, the last step of the signal selection relies on a topological cut in the variable H_T defined as :

$$H_T = {p_T}^{\ell_1} + \sum_{i=1}^{2} {p_T}^{j_i} \tag{3.6}$$

where ℓ_1 denotes the highest p_T lepton, and i extends over the two highest p_T jets in the event. For the $e\mu$ analysis, a cut on H_T was found to be more effective than a cut on $\not{E}_T$ in rejecting the $Z \to \tau\tau$ background. For events with only one jet, H_T is defined simply as the scalar sum of the p_T of the lepton and of the leading jet. A cut at $H_T > 115$ GeV for two jet inclusive events and at $H_T > 105$ GeV for one jet exclusive events was found to maximize $S/\sqrt{S+B}$ where S is the number expected $t\bar{t}$ events and B the number of estimated backgounds.

In the ee and $\mu\mu$ channels, the previous version of the analyses were using specific topological variables to further enrich the final data sample with $t\bar{t}$ events. The ee channel used a cut to reject events in which jets are produced in a planar geometry due to gluon radiation to reduce most of the background. This cut is based on the sphericity ($\mathcal{S}$) which is defined as

$$\mathcal{S} = \frac{3}{2}(\epsilon_1 + \epsilon_2), \tag{3.7}$$

where ϵ_1 and ϵ_2 are the two leading eigenvalues of the event-normalized momentum tensor [91]. The tensor ($\mathcal{M}_{xy}$) is calculated as

$$\mathcal{M}_{xy} = \frac{\sum_i p^i_x p^i_y}{\sum_i (p^i)^2}, \tag{3.8}$$

where the index i runs over the leading two electrons and the leading two jets in the event. Sphericity can take values between 0 and 1. A cut at $\mathcal{S} > 0.15$ was applied. In the $\mu\mu$ channel, further background rejection was achieved by cutting on the compatibility of an event with the $Z \to \mu\mu$ hypothesis. To this end, a χ^2 was formed using a Z boson mass constraint and the measured muon momentum resolution. The resulting variable accounts for the p_T and

η dependence of the tracking resolution. Given the muon momentum resolution, selecting events with $\chi^2 > 2$ was more effective than selecting on the dimuon invariant mass. In the 1 fb^{-1} analysis, more effective topological selection were applied. The sphericity cut was substituted by a cut on the missing transvers energy $\not{E}_T$. This requirement was tightened in a dielectron invariant mass window around the Z mass in the dielectron channel. The χ^2 cut in the dimuon channel was also replaced. Instead the missing transverse momentum significance ($\sigma_{\not{E}_T}$) based on the per-event $\not{E}_T$ probability distribution was defined, calculated from the expected resolution on $\not{E}_T$ and the energies of the electrons, muons and jets. This variable $\sigma_{\not{E}_T}$ was required to be larger than 5. This requirement was also used in the ee channel instead of the $\not{E}_T$ cut in the latest $t\bar{t}$ cross section measurement.

Due to improvements in the MC, mainly by taking into account the proper electron, muon (see section 1.1.4) and jet resolutions and propagating these effects to the $\not{E}_T$ computation, it was possible, in the 1 fb^{-1} analysis, to directly evaluate the background coming from mismeasured $\not{E}_T$ from the MC, i.e. using $Z/\gamma^\star \to ee$ and $Z/\gamma^\star \to \mu\mu$ MC to estimate these background in the ee and $\mu\mu$ channels.

The $\sigma_{t\bar{t}}$ cross section is measured by maximizing the likelihood function

$$\mathcal{L} = \prod_i P[n_i, \mu_i(\sigma_{t\bar{t}})] \ , \tag{3.9}$$

where i runs over the channels, and $P[n, \mu(\sigma_{t\bar{t}})]$ is the Poisson probability function to observe n events when $\mu(\sigma_{t\bar{t}})$ events are expected. In order to reduce the influence of systematic uncertainties on the cross section, all systematic errors have been incorporated in the fit as nuisance parameters [92] to constrain the overall uncertainty using data itself. Using this technique, the likelihood (3.9) is modified :

$$\mathcal{L} = \prod_i P[n_i, \mu_i(\sigma_{t\bar{t}}, \nu_k)] \ \prod_k \mathcal{G}(\nu_k; 0, sd), \tag{3.10}$$

where $\mathcal{G}(\nu_k; 0, \mathrm{sd})$ denotes the Gaussian probability density with mean at zero and width corresponding to one standard deviation (sd) of the considered systematic uncertainty. Correlations of systematic uncertainties between channels and between the different samples are naturally taken into account by assigning the same nuisance parameter to the correlated systematic uncertainties. In Eq. 3.10, the free parameters of the fit are ν_k and $\sigma_{t\bar{t}}$. In the 5.4 fb^{-1} analysis, it was quantified that using nuisance parameters leads to an overall improvement of the uncertainty of 20 %. Even with this improvement the measurement using 1 fb^{-1} was still limited by the statistical uncertainty. This was not the case anymore using 5.4 fb^{-1}.

The last novelty included in the 1 fb^{-1} measurement was the extraction of the top quark mass using the $t\bar{t}$ cross section. This extraction will be described in section 3.4.1.

Further changes have been implemented into the $t\bar{t}$ cross section measurement using 5.4 fb^{-1} [90]. In addition to what was already mentioned above, the signal acceptance has been further increased by loosening the trigger requirements. Indeed in the ee channel, the previous analyses were requiring a dielectron trigger to be fired (typically with two electromagnetic clusters with E_T>6 GeV at level 1, and with E_T>18 GeV at level 2. The level 3 requirements varied depending of the luminosity conditions). This trigger requirement was loosened to request a set of single electron triggers. Single muon triggers were used in

Source	$+\sigma$ [pb]	$-\sigma$ [pb]
Statistical	+0.50	−0.48
Muon identification	+0.11	−0.11
Electron identification and smearing	+0.24	−0.23
Signal modeling	+0.34	−0.33
Triggers	+0.19	−0.19
Jet energy scale	+0.13	−0.12
Jet reconstruction and identification	+0.21	−0.20
b-tagging	+0.06	−0.06
Background normalization	+0.29	−0.27
Instrumental background	+0.18	−0.17
Luminosity	+0.57	−0.51
Other	+0.10	−0.10
Template statistics	+0.08	−0.08

Table 3.4 – Breakdown of uncertainties on the $t\bar{t}$ cross sections in the $\ell\ell'$ channel with 5.4 fb^{-1} [90] using the nuisance parameter technique. The $\pm\sigma$ give the impact on the measured cross section when the nuisance parameters describing the considered category are shifted by ± 1 SD from their fitted mean.

the $\mu\mu$ channel. For the $e\mu$ channel, previous analyses were using an electron-muon trigger with a typical level 1 requirement on the electron at E_T>5 GeV and a loose muon. This was loosened in the 5.4 fb^{-1} analysis to consider events selected by a mixture of single and multilepton trigger as well as lepton+jet triggers. Efficiencies for single lepton triggers have been measured with $Z/\gamma^{\star}\rightarrow \ell\ell$ data. These efficiencies are found to be around 99% for the ee channel and 80% for $\mu\mu$. For the $e\mu$ channel the trigger efficiency is close to 100%. In the 5.4 fb^{-1} analysis, the offline muon quality was also loosened from medium quality to loose quality (see section 1.1.2 for the muon quality definitions).

The other important change in the last version of the $t\bar{t}$ cross section measurement was the use of b-tagging. A neural-network (NN) tagging algorithm [93] to identify jets from b-quark was used since the $t\bar{t}$ events have two b-quark jets in the final state, but most of the background events have jets produced by light quarks or gluons. The algorithm combines information from the impact parameters of the tracks and variables that characterize the presence and properties of secondary vertices within the jet in a single discriminant. The NN discriminant has a value close to one for the b-quark jets and close to zero for the light quark and gluon jets. In order to achieve a better separation between signal and background when measuring the cross section, no explicit cut was applied on the NN discriminant but instead the full distribution of the smallest of the two b-tagging NN discriminants of the two leading jets was used. Then the $t\bar{t}$ cross section was measured by simultaneously fitting the NN distributions in the four channels and maximizing the likelihood function (3.10). With this method as well as the incorporation of the systematic uncertainty using nuisance parameters, this measurement was systematically limited at DØ for the first time in the *dil* channel. The systematic uncertainties for this measurement are summarized in Table 3.4.

Some distributions in the $e\mu$ channel that carries the largest weight within the *dil* final

states due its larger branching ratio are presented on Figure 3.5. Figure 3.6 shows the DØ *dil* measurements as a function of the top quark mass and compared to theoretical computations.

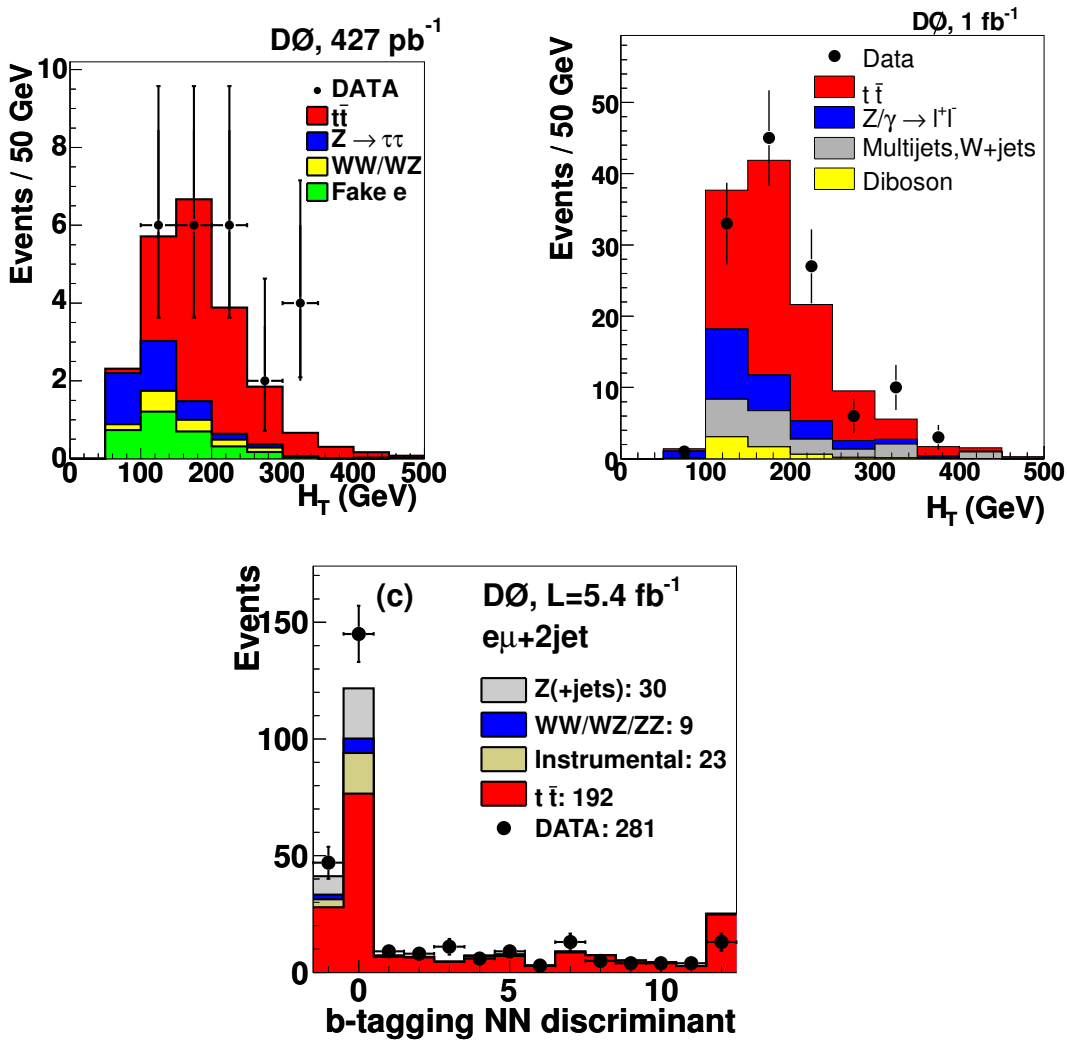

FIGURE 3.5 – Expected and observed distributions for the H_T variable in the $e\mu$ final state using 0.42 fb^{-1} [88] and 1 fb^{-1} [89] (top). Expected and observed distribution for the smallest b-tagging NN discriminant output of the two leading jets for the $e\mu$ channel using 5.4 fb^{-1} [90].

Potential additional improvements would have to focus on reducing the systematic uncertainties. The main gain could be to reduce the uncertainty coming from luminosity. This could be achieved by normalizing the number of events observed in data using Z events before any jet requirement. The CDF collaboration has in fact measured the ratio of the $t\bar{t}$ over the Z cross section in the ljt channel [94]. If the Z events are selected based on trigger and lepton requirements carefully chosen, such a measurement of the number of Z also constrains the trigger and lepton systematic uncertainties in $t\bar{t}$ events and so further increases its accuracy.

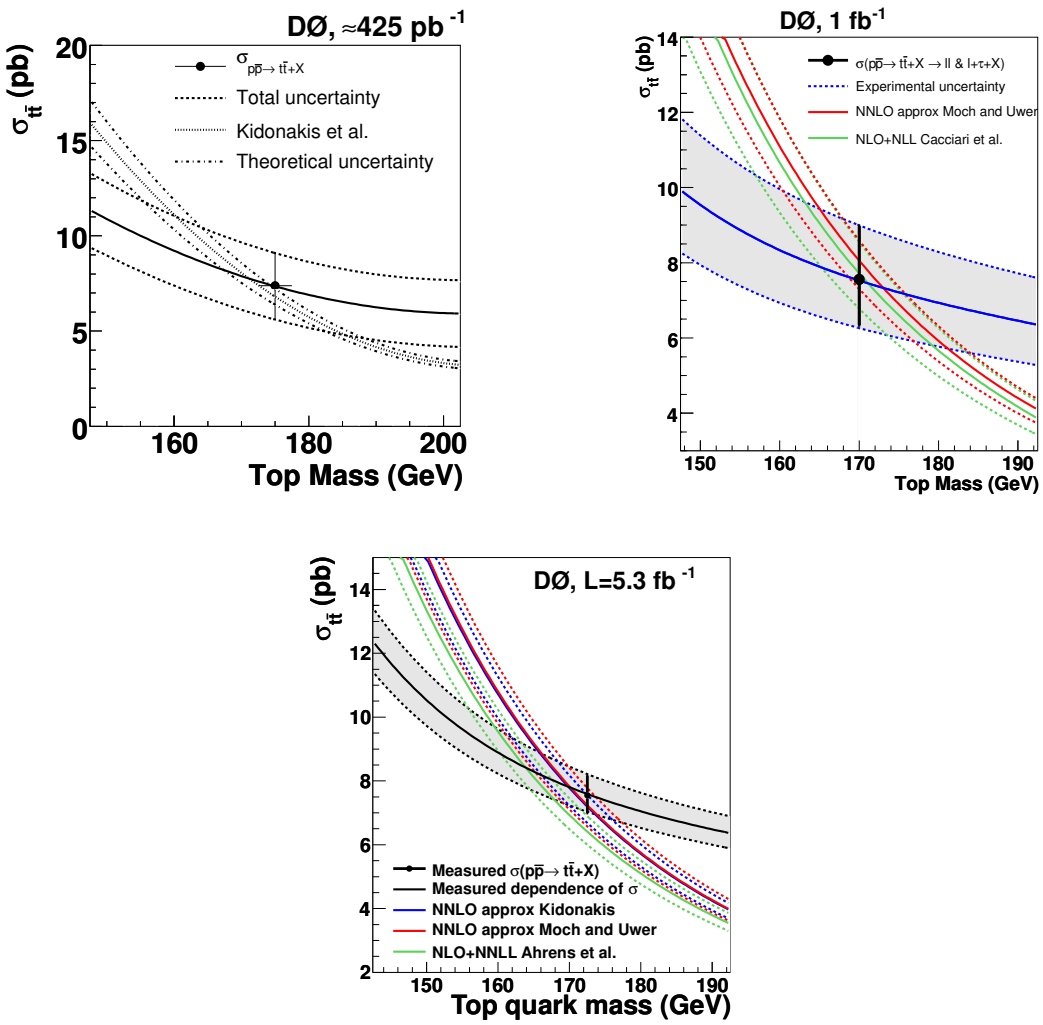

FIGURE 3.6 – Dependency of the experimental and theoretical $t\bar{t}$ cross section measurements in the *dil* channel on the top quark mass using 0.42 fb^{-1}, 1 fb^{-1}and 5.4 fb^{-1} by DØ [88, 89, 90].

Dilepton $t\bar{t}$ Cross Section Measurements at Other Experiments

The CDF collaboration has also performed $t\bar{t}$ cross section measurement in the *dil* channel. Its latest published result gives :

$$\sigma_{t\bar{t}} = 6.27 \pm 0.73 \text{ (stat)} \pm 0.63 \text{ (syst)} \pm 0.39 \text{ (lumi) pb}$$

for $m_t = 175$ GeV using 2.8 fb^{-1}, which corresponds to a relative uncertainty of 17 %. The current most precise preliminary measurement from CDF for $m_t = 172.5$ GeV using 5.1 fb^{-1} of data employs b-tagging and yields :

$$\sigma_{t\bar{t}} = 7.25 \pm 0.66 \text{ (stat)} \pm 0.47 \text{ (syst)} \pm 0.44 \text{ (lumi) pb},$$

which yields a 13 % relative uncertainty.

The latest preliminary measurements at the LHC for $m_t = 172.5$ GeV at $\sqrt{s} = 7$ TeV

are from ATLAS using 0.7 fb^{-1} :

$$183 \pm 6 \text{ (stat)}^{+18}_{-14} \text{ (syst)}^{+8}_{-7}\text{(lumi) pb},$$

with a relative uncertainty of 10 % and from CMS using 1.1 fb^{-1} of data :

$$169.9 \pm 3.9 \text{ (stat)} \pm 16.3 \text{ (syst)} \pm 7.6\text{(lumi) pb}$$

for $m_t = 172.5$ GeV, corresponding to a 11 % total relative uncertainty.

As for the DØ one, most of these measurements are now systematically limited. In the future, the emphasis will then be put more on precise differential cross section measurements.

3.3.3 $t\bar{t}$ Cross Section Combination

CDF and DØ have measured the $t\bar{t}$ cross section in almost all possible decay channels assuming the SM branching fractions. Figure 3.7 shows the evolution in time of some of these measurements. A comparison of the results is sensitive to potential BSM contributions

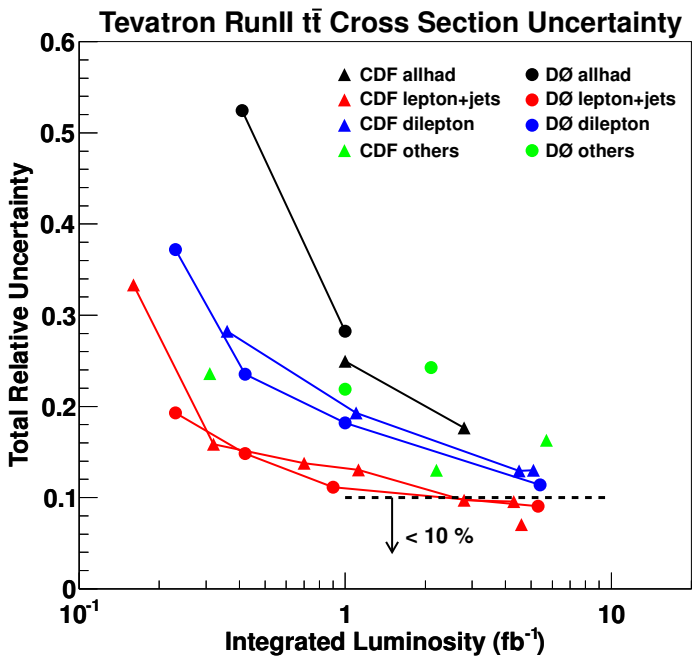

FIGURE 3.7 – Evolution in time of the experimental total uncertainty on the main $t\bar{t}$ cross section measurements by CDF and DØ in the different top quark decay channels.

that affect the various decay channel in ratios differing from the SM. Within uncertainties all the measured $t\bar{t}$ cross sections in the different final states agree with each other. These measurements are further combined yielding an improved precision on the $t\bar{t}$ cross section. To simplify the combination all channels are constructed to be statistically independent. To compute the combined cross section, DØ uses again the nuisance parameter approach taking correlations between common systematics uncertainties into account. The product of the likelihood for the *dil* and *ljt* channels is maximized including each systematic uncertainty

as a nuisance parameter in the likelihood function [90]. Correlations between channels are taken into account by using the same nuisance parameter. Combining the ljt and the dil channels measured using 5.4 fb^{-1}, DØ finds [90] $\sigma_{t\bar{t}} = 7.56^{+0.63}_{-0.56}$ pb for $m_t = 172.5$ GeV, in agreement with the theoretical prediction. CDF performs a combination of its latest preliminary measurements, using up to 5.7 fb^{-1} of data in the dil, had, topological ljt, and b-tag ljt channels, by forming a best linear unbiased estimate [95, 96] and taking into account the statistical and systematic correlations. For $m_t = 172.5$ GeV/c^2 the preliminary combination yields 7.50 ± 0.48 pb in agreement with the theoretical computation. Figures 3.8 show a summary of the latest $t\bar{t}$ cross section measurements performed by CDF and DØ.

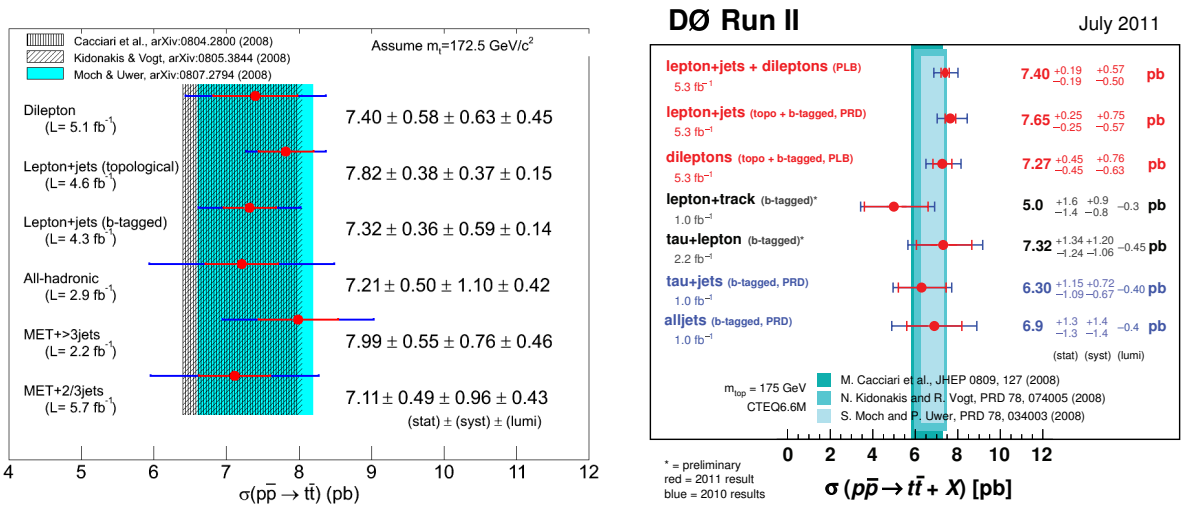

FIGURE 3.8 – Summary of the latest $t\bar{t}$ cross section measurements performed by CDF (left) and DØ (right).

3.3.4 Ratio of $t\bar{t}$ Cross Sections

Calculating the ratio of $\sigma_{t\bar{t}}$ measured in different final states or with different numbers of b-tagged jets probes for the presence of non-SM decays of the top quark. Some BSM theories which might give rise to such effects were discussed in section 3.2.

An example of such an approach, that I worked on with one of my student, is the measurement of the ratio of top quark branching fractions, $R_b = \dfrac{\mathcal{B}(t \to Wb)}{\mathcal{B}(t \to Wq)}$, which can be expressed in terms of the Cabibbo Kobayashi Maskawa (CKM) matrix elements [97, 98]. Indeed the decay rate of the top quark into a W boson and a down-type quark q ($q = d, s, b$) is proportional to $|V_{tq}|^2$, the squared element of the CKM matrix. Under the assumption of a unitary 3×3 CKM matrix, $|V_{tb}|$ is highly constrained to $|V_{tb}| = 0.999152^{+0.000030}_{-0.000045}$ [23], and the top quark decays almost exclusively to Wb. The existence of a fourth generation of quarks would remove this constraint and accommodate significantly smaller values of $|V_{tb}|$. A smaller value of $|V_{tb}|$ could be observed directly through the electroweak production of single top quarks, for which the cross section is proportional to $|V_{tb}|^2$, and could also affect the decay rates in the $t\bar{t}$ production channel. The latter can be used to extract the ratio of

branching fractions R_b :

$$R_b = \frac{\mathcal{B}(t \to Wb)}{\mathcal{B}(t \to Wq)} = \frac{\mid V_{tb} \mid^2}{\mid V_{tb} \mid^2 + \mid V_{ts} \mid^2 + \mid V_{td} \mid^2} . \tag{3.11}$$

Given the constraints on the unitary 3×3 CKM matrix elements, R is expected to be $0.99830^{+0.00006}_{-0.00009}$. R_b was measured using 5.4 fb^{-1} of data collected by DØ in the *dil* channel[99]. This result was combined with the measurement in the ljt channel using the same dataset. The key ingredient in the *dil* measurement is the use of the NN b-tagging algorithm to identify jets from b quarks and then distinguish the bb, bq_l and q_lq_l $t\bar{t}$ final states. The NN smallest output of the two leading jets was used to calculate a discriminant likelihood as it yields the best expected precision on R_b for values close to unity. Templates for the $t\bar{t}$ decay modes bb, bq_l, q_lq_l as well as for all background components were constructed and a likelihood as in Eq. 3.10 was formed for each bin of the NN output. R_b is then fitted simultaneously with the $t\bar{t}$ cross section to obtain :

$$\begin{aligned} R_b &= 0.86 \pm 0.05(\text{stat} + \text{syst}), \\ \sigma_{t\bar{t}} &= 8.19^{+1.06}_{-0.92}(\text{stat} + \text{syst}). \end{aligned}$$

In such a $\sigma_{t\bar{t}}$ measurement, $\mathcal{B}(t \to Wb) = 1$ was not assumed as in the measurements described in the previous section, but only $\mathcal{B}(t \to Wq) = 1$ is required. Figure 3.9 shows the distribution of the minimum b-tag NN ouput for different R_b hypothesis. This result is still dominated by the statistical uncertainties. It was further combined with the ljt channel to give :

$$R_b = 0.90 \pm 0.04 \text{ (stat+syst)}$$

where the result is dominated now by systematic uncertainties among which the uncertainty on the b-tagging probability is the largest. Using the Feldman and Cousins [100] frequentist approach, we obtain the intervals in R as 0.82–0.98 and V_{tb} as 0.90–0.99 at 95% CL. This result is compatible with the SM expectation at the 1.6% level.

Another example of BSM top-quark decays is $t \to H^+b$. A large $H^+ \to \tau^+\nu$ branching fraction would result in a larger fraction of $t\bar{t}$ events showing up in the $\ell\tau$ channel and fewer events in other channels than expected by the SM. On the other hand, a leptophobic charged Higgs would lead to fewer events in the $\ell\ell$ channel compared to ljt. The ratios of the $t\bar{t}$ cross sections as measured in the various decay channels (noted R_σ) was determined by DØ after taking correlations into account. Although the individual channels considered are exclusive, each channel can receive signal contributions from different $t\bar{t}$ decay modes. The ratio of the $\ell\ell$ to ljt channel was measured as [101] $R_\sigma^{\ell\ell/ljt} = 0.86^{+0.19}_{-0.17}$ while the ratio of the $\ell\tau$ determined cross section relative to all the others was measured as $R_\sigma^{\ell\tau/\ell\ell+\ell j} = 0.97^{+0.32}_{-0.29}$, both of which are compatible with the SM expectation. The measured $t\bar{t}$ ratios are summarized in Figure 3.10. These were used to set limits on tauonic ($B(H^+ \to \tau\nu)$) and leptophobic ($B(H^+ \to c\bar{s})$) charged Higgs decays [101] as well as on the parameter space of the MSSM [102]. To do that the total number of expected $t\bar{t}$ events $N_{t\bar{t}}$ is expressed in term of the branching fraction $B = B(t \to H^+ + b)$ when the charged Higgs boson is lighter than the top :

$$N_{t\bar{t}} = [(1-B)^2.\epsilon_{WW} + 2B(1-B)\epsilon_{WH} + B^2\epsilon_{HH}]\sigma_{t\bar{t}}\mathcal{L}, \tag{3.12}$$

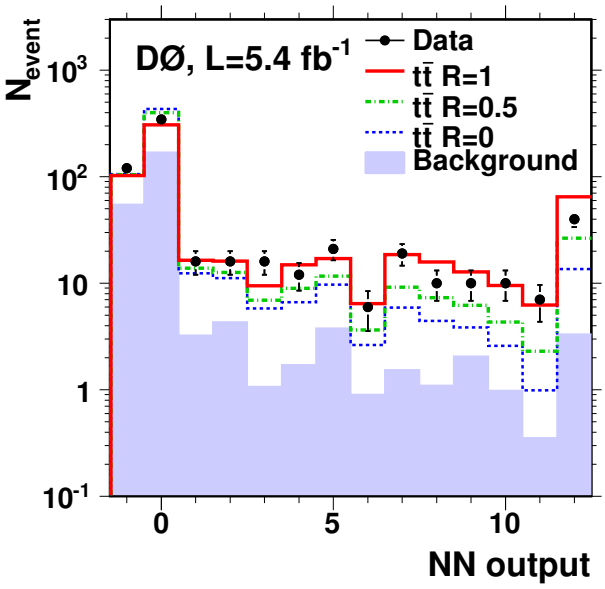

FIGURE 3.9 – Distribution in the minimum b-tag NN output of the jets of highest-p_T for the *dil* final state.

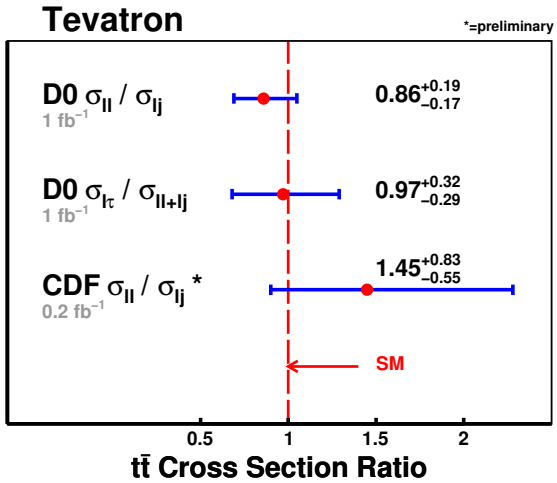

FIGURE 3.10 – Summary of the $t\bar{t}$ cross section ratios measured by DØ [101] and CDF.

where ϵ are the selection efficiencies for the different decays (WW refers to $t\bar{t} \to W^+bW^-\bar{b}$) and $\mathcal{L}$ is the integrated luminosity. The number of expected and observed events for different top decay channels are shown in Figure 3.11.

CDF has also reinterpreted its cross section results to set limits on the charged Higgs production [103] and assuming five possible Higgs decay modes : $t \to W^+b$, $t \to H^+b \to tau^+\nu b$, $t \to H^+b \to c\bar{s}b$, $t \to H^+b \to t^*\bar{b}b$ and $t \to H^+b$ where $H^+ \to W^+h$ and $h \to b\bar{b}$. Limits are set in the plane $(H^+, \tan\beta)$ for several MSSM scenarios. If no assumption is made on the charged Higgs decay, an upper limit on $\mathcal{B}(t \to H^+b)$ of 0.91 is set at 95 % confidence level.

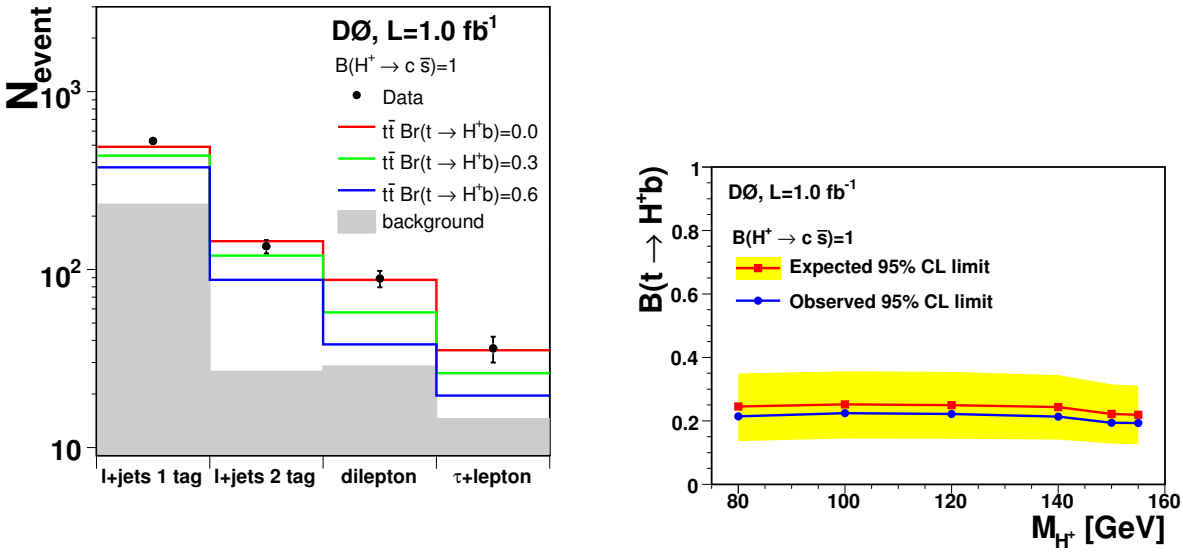

FIGURE 3.11 – (left) Number of expected and observed events for $M_{H^+} = 80$ GeV assuming an exclusive $c\bar{s}(b)$ decays of the charged Higgs boson. (right) Upper limit on $B(H^+ \to c\bar{s})$ for a leptophobic charged Higgs model versus the mass of the charged Higgs boson.

3.4 Some Top Quark Properties

3.4.1 Top Quark Mass

The top-quark mass is a free parameter in the SM and must be experimentally determined. A precision determination of m_t is important since quantum loops including top quarks contribute large corrections to theory predictions for many precision electroweak observables. For example, the SM predicts a precise relationship between the W- and Z^0-boson masses,

$$\left(\frac{m_W}{m_Z}\right)^2 = \left(1 - \sin^2\theta_W\right)(1 + \Delta\rho) \tag{3.13}$$

where $\sin\theta_W$ is the weak mixing angle and $\Delta\rho$ is 0 at tree level and non-zero once quantum loop corrections are included. The dominant quantum corrections are quadratically dependent on the top-quark mass and logarithmically dependent on the higgs-boson mass, $\Delta\rho = f(m_t^2, \ln m_H)$. As discussed in more detail in [23, 104], the experimental program then consists of measuring m_W, m_Z, and m_t as precisely as possible in order to constrain m_H. The experiments at LEP and SLAC precisely determined m_Z, the Tevatron and LEP2 experiments precisely determine m_W, and the Tevatron experiments alone precisely determine m_t. It is important to measure m_t in all the different top decay channels since BSM contributions can affect them differently [105].

Aside from having to isolate a relatively pure sample of $t\bar{t}$ events, there are a few experimental challenges to making a precise determination of m_t. One of them is the large systematic uncertainties which can arise from uncertainties in the jet energy corrections. Roughly, each $\pm 1\%$ of uncertainty in the jet energy corrections gives a ± 1 GeV uncertainty in the top-quark mass. This was a limiting systematic uncertainty for early m_t measurements. With larger statistics samples the jet energy corrections can be calibrated *in situ* by constraining the corresponding

jet-jet invariant mass to the world average m_W in events containing a $W \to qq'$ decay. Doing so significantly reduces the associated systematic uncertainty, which then scales with the statistics of the $t\bar{t}$ sample itself. Most measurements in the ljt and had channels now take advantage of this $in\ situ$ calibration by performing simultaneous fits to m_t and the jet energy scale.

For all analyses described below it is necessary to calibrate the measured m_t using MC pseudo-experiments (i.e. ensemble testing) in order to quantify the influence of the simplifications made in the employed techniques. Each pseudo-experiment is built from a mix of $t\bar{t}$ signal and background events in the proportions estimated from the relevant cross section analysis. The number of events contributing to each physics process is allowed to fluctuate according to a Poisson distribution. Once a set of pseudo-events have been assembled, they are then treated just like the data and a determination of m_t is made. Then, from an ensemble of pseudo-experiments, the relationship between the true top-quark mass (i.e. the m_t value used when generating the $t\bar{t}$ MC sample) and the mean measured m_t can be established and, if necessary, corrections can be derived - usually as a linear function of the measured value. This is done separately for each analysis technique. The ensemble of pseudo-experiments is also used to study the expected statistical uncertainty and the statistical behavior of each analysis technique. Once a particular analysis has been calibrated, its performance is checked using blinded MC samples.

Three methods are used at the Tevatron to measure the top-quark mass : the template method, the matrix element method and the ideogram method. They are shortly described below putting the emphasis on the analysis I worked on, namely the dilepton measurement using the matrix element method. Note that despite the small branching fraction of the dil final state and the presence of two neutrinos in each event, the measurement of m_t in the dilepton channel is interesting because of the lower background and the smaller jet multiplicity relative to the ljt channel resulting in a reduced sensitivity to the ambiguity from combining jets in the reconstruction of m_t. The dilepton measurement therefore complements the results from other final states. Moreover, significant differences in measured values of m_t in different $t\bar{t}$ decay channels can be indicative of the presence of physics beyond the SM [105]. However due to the absence of a hadronically decaying W bosons from the top quark decay in this channel, it is not possible to calibrate the JES *in-situ* in the dil channel. For recent detailed reviews on top-quark mass measurements, see [106, 107]. The history of the top quark mass measurements are presented in Figure 3.12.

Some Remarks on the Definition of the Quark Mass

For a free particle, the physical mass is usually defined as the pole of its renormalized propagator. However this definition is ambiguous when dealing with colored particles like quarks. Thus the definition of the top-quark pole mass (m_t^{pole}) is intrinsically ambiguous on the order of Λ_{QCD} due to non-perturbative QCD effects [108, 109, 110]. More precisely when trying to compute the pole of the renormalized propagator, the one-loop gluon radiative correction at the top quark propagator contains an integral over gluon loop momenta that involves region where α_s becomes large, with terms that are growing factorially, such that perturbation theory does not converge. This singularity at all orders is known as the renormalon ambiguity [111]. This indicate that this mass definition is unsuitable for making perturbative calculations with an accuracy better than Λ_{QCD} and that the concept of pole-mass is ambiguous by $\Delta m_t \sim \Lambda_{\text{QCD}}$ [110].

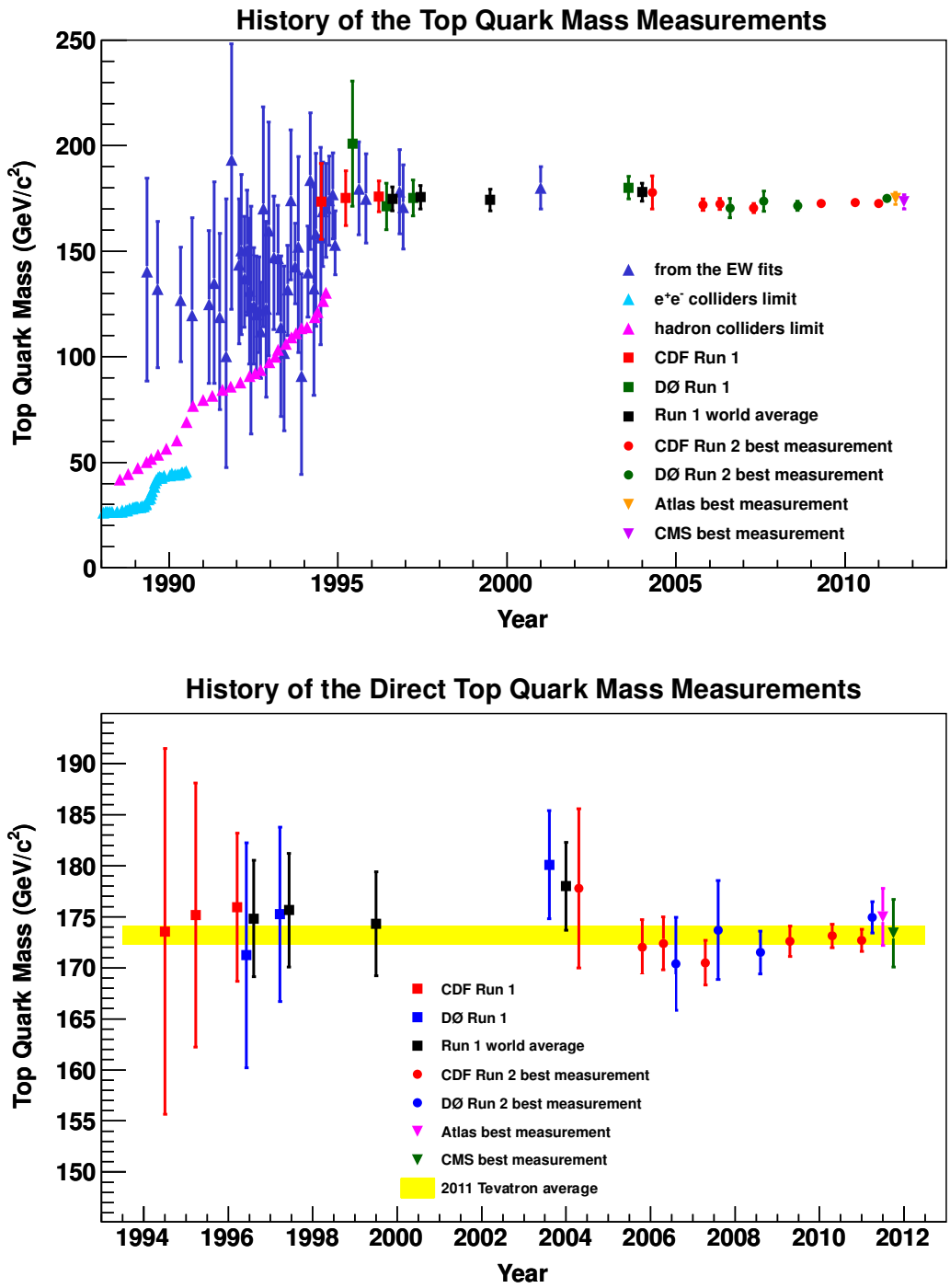

FIGURE 3.12 – Evolution in time of the direct top quark mass measurements at the Tevatron and LHC, with or without the indirect constraints from electroweak fits.

For an unstable particle (like the top quark), the pole mass enters the description of the resonance through a Breit-Wigner function. Other mass definitions exist such as the $\overline{\text{MS}}$-mass ($m_t^{\overline{\text{MS}}}$) using the $\overline{\text{MS}}$ renormalization scheme [112] or those discussed in [113]. The $m_t^{\overline{\text{MS}}}$ mass is only sensitive to short distance QCD effects and is often used to describe the mass of

the light quarks when the typical energy of the process is much larger than the quark mass in question. For most of the studied top quark observables the perturbative series converge significantly faster if expressed in term of $m_t^{\overline{\rm MS}}$ rather than the $m_t^{\rm pole}$. Schemes without the pole-mass infrared problem are known as short-distance masses and always depend on an additional infrared scale R.

At the Tevatron and LHC, the top-quark mass will be directly measured through the reconstruction of its decay products and the measured mass is taken to be $m_t^{\rm pole}$. However, aside from the theoretical ambiguity mentioned above, additional ambiguities are introduced since the measurements are calibrated using MC generators that include model dependent descriptions of the parton shower and hadronization processes. Indeed the top quark is not isolated but is part of a system that evolves by emitting gluons, decays to a b quark which further evolves and hadronizes to form a jet and interact with underlying event activities. As most of these effects are not computable from first principles, experimental measurements relies on their implementation into MC programs so that the direct mass measurements can in fact be seen as the measurement of the top mass parameter implemented into a given event generator. In principle it is not possible to make the exact connection between this mass parameter and a mass defined in a precise mass scheme as parton shower algorithm are based on leading logarithm perturbation theory and so are not accurate enough to fix the scheme since scheme dependence only starts at NLL. However an order-of-magnitude could be estimated speculating on how an ideal algorithm would work [114].

It has been established in [113, 115] that the relation between $m_t^{\rm pole}$ and any other Lagrangian mass-scheme $m_t(R,\mu)$ can be expressed as :

$$m_t^{\rm pole} = m_t(R,\mu) + R\left[\sum_{n=1}^{\infty} \alpha_s^n(\mu) c_n \left(\frac{\mu}{R}\right)\right] \tag{3.14}$$

where μ is the renormalization scale for α_s controlling the ultraviolet fluctuations and R is an auxiliary scale that controls the absorption of the infrared fluctuations. R can be seen as a cutoff on the evolution of the top quark self-energy. For instance, $R = \bar{m}(\mu)$ for the $\overline{\rm MS}$ scheme.

Only physics at scales above Γ_t is sensitive to the value of the top quark mass. However current parton shower algorithms do not interrupt the evolution at scale Γ_t but rather continue down to a scale of around $Q_0 = 1$ GeV. As argued in [114], then using Eq. 3.14 with $R \approx Q_0 \approx 1$, the likely relation between the top quark mass in the MC ($m_t^{\rm MC}$) and $m_t^{\rm pole}$ is :

$$m_t^{\rm pole} = m_t^{\rm MC} + Q_0[\alpha_s(Q_0)c_1 + ...]$$

where c_1 is unknown but assumed to be of order of 1. Hence $m_t^{\rm pole}$ could be of order of 1 GeV higher than $m_t^{\rm MC}$. Given the current experimental uncertainty on the direct top mass measurements as we will see below, more attention to clarify this relation would be needed. An alternative approach extracting the top-quark mass from the $t\bar{t}$ cross section does not suffer from this problem as will also discuss below but is still less precise than direct measurements.

Template Method

This traditional method begins by choosing an observable correlated with the top-quark mass. Distributions of this observable are then constructed using MC samples generated with varying

m_t as input. The data distribution is then compared with these MC templates using a maximum likelihood fit. The observable most correlated with m_t is the reconstructed invariant mass of the $t\bar{t}$ decay products, $m_t^{\rm reco}$, which is the most often used and is estimated using the kinematic fits. If a given analysis uses the hadronic W-boson decay to calibrate the jet energy corrections, an observable correlated with m_W is used - usually the invariant mass of the associated jets, m_{jj} - and the maximum likelihood fit is extended to two dimensions. The template method is relatively simple and can be easily extended to several decay channels or sub-samples. The observable(s) used as estimators can be chosen to minimize sensitivity to specific systematic uncertainties. The statistical sensitivity of this method is sometimes worse than other methods because it does not use the full event information, nor take advantage of event-by-event differences to weight more heavily those events with kinematics resulting in improved $m_t^{\rm reco}$ resolution.

A detailed description of using the template method to measure m_t in the dil channel can be found in [116]. Recent measurements use essentially the same methodologies on significantly larger data sets. Since the kinematics of the dil events is under constrained it is necessary to make an additional kinematic assumption in order to obtain a reconstructed invariant mass for each event. The CDF and DØ template analyses in the dil channel primarily differ in the additional kinematic assumption they choose to make.

CDF's most recent template analysis in the dil channel uses the neutrino ϕ weighting method [117], which integrates over the azimuthal angles for the two neutrinos in each event. A χ^2 function is minimized to estimate $m_t^{\rm reco}$ for each event. This χ^2 function includes a term that constrains the measured quantities within their uncertainties to the assumed $t\bar{t}$ kinematics. Templates of the $m_t^{\rm reco}$ distributions are obtained from simulated samples of $t\bar{t}$ signal and background events generated at discrete values of m_t. The shape of the templates is fit to a Landau plus two Gaussians function and the resulting parameterizations are smoothed and interpolated to enable an estimate of the template shape at any arbitrary m_t value. The top-quark mass is determined using an unbinned likelihood fit to the data.

DØ template analyses in the dil channel use a neutrino weighting method and the so called matrix weighting method [118]. The neutrino weighting algorithm employed integrates over the neutrino rapidities as the assumed input to the kinematic fit. Weights are assigned by comparing the resulting neutrino momenta solutions to the measured $\not\!\!E_T$. The first two moments of the weighted distributions are used from each event to build $m_t^{\rm reco}$ templates and extract from the data distribution the most probable top-quark mass. The templates are constructed in two different manners, using binned probability density histograms and using probability density fit functions, which are later combined. The matrix weighting technique integrates over assumed top-quark masses and solves for the t and $\bar{t}$ momenta. Each solution is then weighted by the probability to measure the observed lepton energy in the top-quark rest frame given the assumed top-quark mass using the matrix element based expressions in [119]. For each event $m_t^{\rm reco}$ is taken from the maximum of the resulting weighted distribution and used to build templates.

Using 2.9 $\rm fb^{-1}$, CDF measures in the dil channel [117] : $m_t = 165.5^{+3.4}_{-3.3}\,(\rm stat)\pm 3.1\,(\rm syst)$ GeV. Using 1 $\rm fb^{-1}$, DØ combines the results from the neutrino weighting and the matrix weighting techniques in the dil channel to measure [118] $m_t = 174.7 \pm 4.4\,(\rm stat) \pm 2.0\,(\rm syst)$ GeV. These measurements are still limited by statistics. The systematic uncertainty is completely dominated by the uncertainty in the jet energy corrections as no $in\ situ$ jet energy scale calibration is possible in the dil channel.

Using $5.6\ \rm fb^{-1}$ of CDF data and simultaneously fits the ljt and dil channels using the

in situ $W \to qq'$ decays to constrain the jet energy corrections and reduce the associated systematic uncertainties [120]. Two dimensional templates are constructed for each channel and a joint likelihood fit is performed to measure m_t. Templates are built from simulated samples of $t\bar{t}$ and background events using MC generated at discrete values of m_t. The shape of the templates at these discrete points is described using kernel density estimators [121, 122] and then smoothed and interpolated using the method of [123] to enable an estimate of the template shapes for any arbitrary value of m_t. The two dimensional data distributions are compared to the resulting templates using an unbinned maximum likelihood fit to determine m_t, the best-fit jet energy scale correction, and their associated uncertainties. The resulting top-quark mass is $m_t = 172.1 \pm 1.1$ (stat) ± 0.9 (syst) GeV. The dominant systematic uncertainties arise from residual uncertainties in the jet energy corrections [1] and from variations of the MC generator used to model $t\bar{t}$ events.

Using 1.04 fb^{-1} of 2011 LHC data, ATLAS measured the top-quark mass in ljt channel. The analysis combines two implementations of the template method, one based on the observable R_{32} defined as the per event ratio of the reconstructed invariant masses of the top quark and the W boson, the other is a two-dimensional analysis which simultaneously fit m_t and a global *in-situ* jet energy scale factor from the reconstructed invariant masses of the top quark and the W boson. The resulting top-quark mass is $m_t = 174.37 \pm 0.56$ (stat)± 2.29 (syst) GeV.

Matrix Element Method

The matrix element method is a more sophisticated method for measuring a particle property and constructs a likelihood curve for each event by comparing the observe kinematics to those expected as a function of the particle property of interest (e.g. m_t). The event probability density is estimated using a leading order matrix element and integrating over the unmeasured quantities. Detector effects are incorporated by integrating over resolution functions. The total likelihood for a given sample of events is obtained from the product of the individual event probability densities. The matrix element method offers superior statistical sensitivity since it uses the full kinematic information available in each event and since it effectively gives more weight to events whose kinematics afford a more precise estimate of m_t^{reco} by virtue of having a narrower event probability density. The principal downside is that it is enormously cpu intensive, typically requiring hours of cpu per event. This limitation renders these analyses less nimble than analyses using the template method.

The method is based on an approach suggested in [124, 125] and close to the method suggested for the measurement of the mass of the W boson at LEP [126, 127, 128]. The method was first employed by DØ [129] to measure the top-quark mass. Currently, all the most precise m_t determinations use the matrix element method. It has been applied in all the decay final states. In the ljt and had channels it is extended to include an integration over the jet energy corrections, which are then constrained *in situ* using hadronic W-boson decays. A detailed description of the matrix element technique applied to measure the top-quark mass can be found in [130].

The event probability P_{evt} is built from a $t\bar{t}$ probability ($P_{t\bar{t}}$) and a background probability (P_{b}),

$$P_{\mathrm{evt}}(x; m_t, f_{t\bar{t}}) = f_{t\bar{t}} \cdot P_{t\bar{t}}(x; m_t) + (1 - f_{t\bar{t}}) \cdot P_{\mathrm{b}}(x) \tag{3.15}$$

1. The measurement treats the jet energy scale as a constant. The residual jet energy scale systematic accounts for the known variations of these corrections as a function of jet E_T and η.

where x denotes the set of observed variables (i.e. the jet and lepton momenta) and $f_{t\bar{t}}$ is the $t\bar{t}$ signal fraction in the event sample. The signal and background probability densities are constructed by integrating over the appropriate parton-level differential cross section, $d\sigma(y)/dy$, convoluted with parton distribution functions ($f(q)$) and resolution effects. The resolution effects are described by the transfer functions, $W(x;y)$, which give the probability of observing the set of variables x given the underlying partonic quantities, y. Typically the jet and lepton angles are taken to be exactly measured so that the relevant transfer functions are simply Dirac delta functions. The transfer functions for the jet energies are parameterized as a function of parton energy and rapidity using fully simulated MC events. Separate transfer functions are derived for uds, gluon, and b-jets. The transfer functions for the lepton energies are usually taken to be Dirac delta functions but are sometimes treated in a manner similar to the jets. It should be noted that the transfer functions are not assumed to be Gaussian, and more sophisticated functions can be used to obtain a more accurate description of the relevant resolutions. The $t\bar{t}$ probability density is expressed as

$$P_{t\bar{t}}(x;m_t) = \frac{1}{\sigma^{\text{obs}}} \sum_{\text{j-p comb}} \int \sum_{\text{flavors}} \frac{d\sigma(y;m_t)}{dy} f(q_1)f(q_2)dq_1dq_2W(x;y)dy \tag{3.16}$$

where the first sum is over all possible jet-parton combinations and the second sum is over all relevant PDF parton flavors. The probability density is normalized to the total observed cross section, σ^{obs}, after including event selection effects. For signal the differential cross section is taken from the leading order matrix element, $\mathcal{M}(q\bar{q} \to t\bar{t} \to y)$, found in [131], which depends on m_t. For background the differential cross section is taken from a sum of matrix elements, calculated by dedicated MC generators, and is independent of m_t. The background probability density usually includes contributions from just the dominant background processes. The effect of the resulting approximation on the measured m_t is included as part of the systematic uncertainties and is usually found to be quite small. For analyses that constrain the jet energy corrections using hadronic W-boson decays, the jet energy transfer functions, and thus the event probability densities, are additionally expressed in terms of an overall jet energy scale factor, JES, $W(x;y) \to W(x;y,\text{JES})$.

Both CDF and DØ have recently published measurements of the top-quark mass in the ljt channel using the matrix element technique. In their most recent analysis [132] CDF measures using $3.2\ \text{fb}^{-1}$ of data : $m_t = 172.4 \pm 1.4\ (\text{stat} + \text{JES}) \pm 1.3\ (\text{syst})$ GeV. The dominant systematic uncertainty arises from difference between MC generators.

The DØ analysis [133] includes only the $q\bar{q} \to t\bar{t}$ component in the signal matrix element and calculates the background probability density using only the matrix element for the $W + 4$ partons process. The jet-parton combinations are weighted using information from a b-jet identification algorithm and an *in-situ* JES calibration is performed. The method is calibrated using MC samples generated at various values of m_t and assuming different JES values. A new flavor-dependent correction factor has been developped to bring the bring simulation of the calorimeter response to jets into agreement with data. Using 1 fb^{-1} of data DØ measures $m_t = 174.94 \pm 1.14\ (\text{stat} + \text{JES}) \pm 0.96\ (\text{syst})$ GeV. The dominant systematic uncertainty arises from uncertainties associated with the signal modeling.

CDF and DØ have also published a measurement using the matrix element technique in the *dil* channel [134]. In this channel, no JES *in-situ* calibration is possible. Measurements

in the *dil* channel using other techniques reached a precision of 3.7 GeV. Using 2 fb^{-1}, CDF measures $m_t = 171.2 \pm 2.7$ (stat) $\pm$ 2.9 (syst) GeV.

DØ performed the analysis using 5.4 fb^{-1} [135] using the same dilepton selection as for the cross section measurement described in section 3.3.2. I worked on this measurement together with some of my colleagues in Saclay, one of my students and postdoc. In the ee, $\mu\mu$, $e\mu$ channels, Z+2 jets events with $Z \to e^+e^-$, $Z \to \mu^+\mu^-$ and $Z \to \tau^+\tau^- \to e^+\mu^-\nu$ are the dominant source of background and so this process is used to compute the background probability. The second leading background from misidentified leptons is approximatively a factor of 3 smaller. While neglecting the other background probabilities leads to some bias, the calibration procedure allows us to correct for these and other limitations of the model. This background probability is calculated by using VECBOS [136]. By taking into account energy and momentum conservation, the computation of the probability (3.16) can be reduced to an integration over the b jet energies, the lepton-neutrino invariant masses squared, the differences between neutrino transverse momenta, the transverse momentum of the $t\bar{t}$ system, and the radii of curvature (${p_T}^{-1}$) of muons. The calibration using MC events is shown on Figure 3.13 where the mean value of m_t measured in 1000 pseudoexperiments as a function of the input m_t are displayed. The deviation from the ideal response, where the extracted mass is equal to the input mass, is caused both by the presence of backgrounds without a corresponding matrix element in the event probability and by approximations in the calculation of the Z+2 jets probabilities. For the case of background-free pseudoexperiments, no difference is observed. The width of the distribution of the pulls ("pull width"), defined as the mean deviation of m_t in single pseudoexperiments from the mean for all 1000 values at a given input m_t, in units of the measured uncertainty per pseudoexperiment, is also shown in Figure 3.13. The statistical uncertainty measured in the data is corrected for the deviation of the pull width from unity.

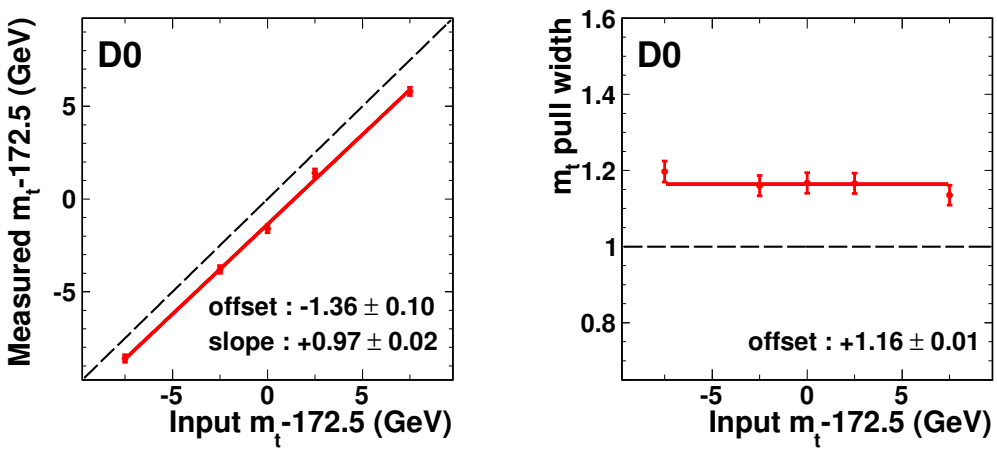

FIGURE 3.13 – (left) Mean values of m_t and (right) pull width from sets of 1000 pseudoexperiments as a function of input m_t for the combined dilepton channels. The dashed lines represent the ideal response [135].

The calibrated value of m_t from the fit to the data is shown in Figure 3.14 as well as the

measured uncertainty for m_t with the distribution of expected uncertainties in pseudoexperiments at $m_t = 175$ GeV.

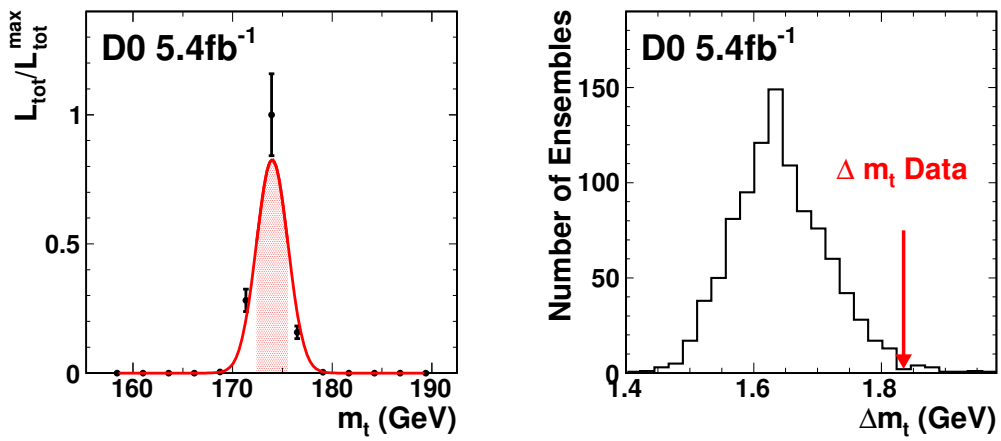

FIGURE 3.14 – (left) Calibrated likelihood for the data as a function of m_t with the best estimate as well as 68% confidence level region marked by the shaded area and (right) the expected distribution of uncertainties with the measured uncertainty indicated by the arrow [135].

The systematic uncertainties on this measurement comes either from detector modeling, from signal modeling or from the method itself. These uncertainties are summarized in Table 3.4.1.

This measurement is now not limited any more by the statistical uncertainty. The largest systematic uncertainties come from the JES related uncertainties. First the difference in detector reponse of light and b-quark jets is estimated by shifting the b jets response by 1.8 %. Further studies in the ljt channel have led to a new flavor-dependent correction factor to bring the simulation of the calorimeter response to jets into agreement with data, and thereby reduce the systematic uncertainty associated with a jet response difference in data and MC [133]. It can be anticipated that the application of this procedure to the *dil* measurement could reduce the uncertainty coming from the MC/Data b/light jet response down by a factor around 2. The second largest systematic uncertainty comes from the uncertainties in the jet energy scale of light quarks which is calibrated using γ+jets events [137]. This uncertainty, dominated by the understanding of the detector response and the showering of jets, is typically of the order of 1.5% per jet. A way to decrease this uncertainty would be to use jet energy corrections determined from the *in-situ* JES calibration in ljt events taking into account the fact that the jet multiplicity and color flow are different in *dil* and ljt events and then the possibility that the jets in these two classes of events can differ. This could further reduce the JES uncertainty by around 40 %.

The current *dil* measurement is in good agreement with the current world average [138]. Its total uncertainty of 3.1 GeV corresponds to a 1.8 % accuracy and represents the most precise measurement of m_t from dilepton $t\bar{t}$ final states.

Source	Uncertainty (GeV)
Detector modeling :	
b/light jet response	± 1.6
JES	± 1.5
Jet resolution	± 0.3
Muon resolution	± 0.2
Electron $p_T$scale	± 0.4
Muon $p_T$scale	± 0.2
ISR/FSR	± 0.2
Signal modeling :	
Higher order and hadronization	± 0.7
Color reconnection	± 0.1
b-quark modeling	± 0.4
PDF uncertainty	± 0.1
Method :	
MC calibration	± 0.1
Signal fraction	± 0.5
Total	± 2.4

TABLE 3.5 – Summary of systematic uncertainties on the measurement of m_t in dilepton events [135].

Ideogram Method

The ideogram method can be thought of as an approximation to the matrix element method. A kinematic fit is used to determine $m_t^{\rm reco}$ for each event. A per event probability density is calculated as a function of m_t by calculating the probability of observing $m_t^{\rm reco}$ assuming the true top-quark mass is m_t and knowing the resolution $\sigma_{m_t^{\rm reco}}$. All jet-parton combinations are considered for each event and each carries a weight derived from its corresponding fit chi-squared. Typically, additional weights are included that use information from b-jet identification algorithms. Like the matrix element method the event probability density is built from a signal and a background piece. The signal probability density is a convolution of a Gaussian with a Breit-Wigner while the background probability density is taken from MC simulation. The total likelihood for a given sample of events is obtained from the product of the individual event probability densities. A JES constraint can be incorporated by repeating the kinematic fits for different assumptions on the jet energy corrections scale factor. Like the matrix element method, the ideogram method offers improved statistical sensitivity since it will effectively give more weight to events whose kinematics afford a more precise estimate of $m_t^{\rm reco}$ by virtue of having a narrower event probability density. In terms of sophistication, CPU budget, and statistical sensitivity the ideogram method typically falls between the template and matrix element methods. It should be noted that since it requires a full reconstruction of the $t\bar{t}$ kinematics, this method can only be used in the ljt and had final states.

DØ has performed a measurement using this technique in the ljt channel [139]. The event probability density is factorized into the product of two separate probabilities for signal and

background each. The first probability depends on m_t and JES and provides the necessary information to constrain the jet energy corrections and to measure the top-quark mass. The second probability depends on the output of a multivariate discriminant designed to separate $t\bar{t}$ from background processes. The variables used in the discriminant are chosen and the discriminant itself is constructed to be uncorrelated with m_t and JES. This second probability helps constrain the observed $t\bar{t}$ fraction in the event sample and to de-weight events that have kinematics more consistent with having originated from background processes. MC simulation is used to account for contributions from wrong jet-parton assignments and background events. The method is calibrated using MC samples generated at various m_t values. Using 0.43 fb^{-1}, DØ measures $m_t = 173.7 \pm 4.4\ (\mathrm{stat} + \mathrm{JES})^{+2.1}_{-2.0}\ (\mathrm{syst})$ GeV. The dominant systematic uncertainty arises from uncertainties associated with calibrating the response of the calorimeter to b-quark jets and from uncertainties associated with modeling the $t\bar{t}$ signal.

The method was first used by CDF to measure m_t, which produced a result in the had channel using 310 pb^{-1} [140]. The result was limited by the uncertainties in the jet energy corrections. Subsequent m_t determinations in the had channel exploit $W \to qq'$ decays to reduce the jet energy correction systematic and also include significantly larger data sets as described above.

Using 36 pb^{-1} of 2010 LHC data, CMS used the ideogram method to measure a top quark mass of : $m_t = 173.1 \pm 2.1\ (\mathrm{stat})^{+2.8}_{-2.5}\ (\mathrm{syst})$ GeV in the ljt channel which is further combined with a measurement in the dil channel yielding : $m_t = 173.4 \pm 1.9\ (\mathrm{stat}) \pm 2.7\ (\mathrm{syst})$ GeV.

Using the $t\bar{t}$ Cross Section

As mentioned above, there is some ambiguity associated with the theoretical interpretation of the m_t parameter measured by the above techniques. Indeed beyond LO QCD, the mass of the top quark is a convention-dependent parameter. Therefore, it is important to know how to interpret the experimental result above in terms of renormalization conventions if the value is to be used as an input to the fits of electroweak precision observables (see beginning of the section). Assuming SM production and decay, an estimate of the top-quark mass can also be made by comparing the measured production $t\bar{t}$ cross section to fully inclusive theory calculations at higher-order QCD that involve an unambiguous definition of m_t (see section 3.3.1). While less precise, this method has the advantage that the m_t parameter in the predictions is theoretically well defined. This extraction also provides an important test of the mass scheme as applied in MC simulations and gives complementary information, with different sensitivity to theoretical and experimental uncertainties than the direct measurements of m_t^{MC} that rely on kinematic details of the mass reconstruction.

DØ has performed this measurement using several $t\bar{t}$ cross section as input [141, 101]. I worked on this measurement together with DØ colleagues and one of my student. The most precise extraction is using 5.4 fb^{-1} in the ljt channel [142]. The signal acceptance is estimated as a function of m_t using MC samples generated at various m_t values. The m_t dependence of the acceptance arises from the event selection lepton p_T and jet E_T requirements. This dependence is found to be weaker than the dependence of the theoretical computations of $\sigma_{t\bar{t}}$. The resulting acceptances are smoothed using the function :

$$\begin{aligned} \sigma_{t\bar{t}}(m_t^{\mathrm{MC}}) &= \frac{1}{(m_t^{\mathrm{MC}})^4}[a + b\ (m_t^{\mathrm{MC}} - m_0) \\ &+ c\ (m_t^{\mathrm{MC}} - m_0)^2 + d\ (m_t^{\mathrm{MC}} - m_0)^3]\,, \end{aligned} \tag{3.17}$$

where $\sigma_{t\bar{t}}$ and $m_t^{\rm MC}$ are in pb and GeV, respectively, $m_0 = 170$ GeV, and a, b, c, d are free parameters. For the mass extraction, the $t\bar{t}\ ljt$ cross section using b-jet identification in [143] was used asince it has the weakest dependence on $m_t^{\rm MC}$ which leads to a smaller uncertainty on the extracted m_t.

The measured cross section is compared to a pure NLO QCD [144, 74] calculation, to a calculation including NLO QCD and all higher-order soft-gluon resummations in NLL [145], to a calculation including also all higher-order soft-gluon resummations in next-to-next-to-leading logarithms (NNLL) [82, 146] and to two approximations of the NNLO QCD cross section that include next-to-next-to-leading logarithms (NNLL) relevant in NNLO QCD [147, 78]. The computations in [147] were obtained using the program documented in Ref. [83].

The most probable m_t values and their 68% C.L. bands for the pole-mass ($m_t^{\rm pole}$) and $\overline{\rm MS}$-mass ($m_t^{\overline{\rm MS}}$) conventions by computing the most probable value of a normalized joint-likelihood function :

$$L(m_t) = \int f_{\rm exp}(\sigma|m_t)\ [f_{\rm scale}(\sigma|m_t) \otimes f_{\rm PDF}(\sigma|m_t)]\ d\sigma. \tag{3.18}$$

The first term $f_{\rm exp}$ corresponds to a function for the measurement constructed from a Gaussian function with mean value given by Eq. (3.17) and with standard deviation (sd) equal to the total experimental uncertainty. The second term $f_{\rm scale}$ is a theoretical likelihood formed from the uncertainties on the renormalization and factorization scales of QCD, which are taken to be equal, and varied up and down by a factor of two from the default value. Within this range, $f_{\rm scale}$ is taken to be constant. It is convoluted with a term $f_{\rm PDF}$ that represents the uncertainty of parton density functions (PDFs), taken to be a Gaussian function, with rms equal to the uncertainty determined in the theoretical computations.

As $\sigma_{t\bar{t}}$ in the theoretical above calculations are performed as a function of $m_t^{\rm pole}$, comparing the measured $\sigma_{t\bar{t}}(m_t^{\rm MC})$ to these theoretical predictions provides a value of $m_t^{\rm pole}$. $m_t^{\rm pole}$ was extracted assuming that the definition of $m_t^{\rm MC}$ is equivalent to $m_t^{\rm pole}$, alternatively taking $m_t^{\rm MC}$ to be equal to $m_t^{\overline{\rm MS}}$ to estimate the effect of interpreting $m_t^{\rm MC}$ as any other mass definition. In that later case, the value of $m_t^{\rm MC} = m_t^{\overline{\rm MS}}$ is converted to $m_t^{\rm pole}$ using the relationship at the three-loop level [110, 148, 149] :

$$\begin{aligned} m_t^{\rm pole} &= m_t^{\overline{\rm MS}}(m_t^{\overline{\rm MS}}) \left[1 + \frac{4}{3}\frac{\overline{\alpha}_s(m_t^{\overline{\rm MS}})}{\pi} \right. \\ &+ (-1.0414 N_L + 13.4434) \left(\frac{\overline{\alpha}_s(m_t^{\overline{\rm MS}})}{\pi} \right)^2 \\ &+ \left. (0.6527 N_L^2 - 26.655 N_L + 190.595) \left(\frac{\overline{\alpha}_s(m_t^{\overline{\rm MS}})}{\pi} \right)^3 \right], \end{aligned} \tag{3.19}$$

where $\overline{\alpha}_s$ is the strong coupling in the $\overline{\rm MS}$ scheme, and $N_L = 5$ is the number of light quark flavors. The strong coupling $\overline{\alpha}_s(m_t^{\rm pole})$ is taken at the three-loop level from Ref. [150]. The resulting values of $m_t^{\rm pole}$ are summarized in Table 3.4.1. Given the uncertainties, interpreting $m_t^{\rm MC}$ as either $m_t^{\rm pole}$ or as $m_t^{\overline{\rm MS}}$ has no significant influence on the value of the extracted m_t.

Theoretical prediction	m_t^{pole} (GeV)	Δm_t^{pole} (GeV)
MC mass assumption	$m_t^{\text{MC}} = m_t^{\text{pole}}$	$m_t^{\text{MC}} = m_t^{\overline{\text{MS}}}$
NLO [144, 74]	$164.8^{+5.7}_{-5.4}$	-3.0
NLO+NLL [145]	$166.5^{+5.5}_{-4.8}$	-2.7
NLO+NNLL [82, 146]	$163.0^{+5.1}_{-4.6}$	-3.3
Approximate NNLO [147]	$167.5^{+5.2}_{-4.7}$	-2.7
Approximate NNLO [78]	$166.7^{+5.2}_{-4.5}$	-2.8

TABLE 3.6 – Values of m_t^{pole}, with their 68% C.L. uncertainties, extracted for different theoretical calculations of $\sigma_{t\bar{t}}$. The results assume that $m_t^{\text{MC}} = m_t^{\text{pole}}$ (left column). The right column shows the change Δm_t^{pole} between these results if it is assumed that $m_t^{\text{MC}} = m_t^{\overline{\text{MS}}}$ [142].

Theoretical prediction	$m_t^{\overline{\text{MS}}}$ (GeV)	$\Delta m_t^{\overline{\text{MS}}}$ (GeV)
MC mass assumption	$m_t^{\text{MC}} = m_t^{\text{pole}}$	$m_t^{\text{MC}} = m_t^{\overline{\text{MS}}}$
NLO+NNLL [82, 146]	$154.5^{+5.0}_{-4.3}$	-2.9
Approximate NNLO [147]	$160.0^{+4.8}_{-4.3}$	-2.6

TABLE 3.7 – Values of $m_t^{\overline{\text{MS}}}$, with their 68% C.L. uncertainties, extracted for different theoretical calculations of $\sigma_{t\bar{t}}$. The results assume that $m_t^{\text{MC}} = m_t^{\text{pole}}$ (left column). The right column shows the change $\Delta m_t^{\overline{\text{MS}}}$ between these results if it is assumed that $m_t^{\text{MC}} = m_t^{\overline{\text{MS}}}$ [142].

Calculations of the $t\bar{t}$ cross section [82, 146, 147] have also been performed as a function of $m_t^{\overline{\text{MS}}}$ leading to a faster convergence of the perturbative expansion [147]. Therefore, comparing the dependence of the measured $\sigma_{t\bar{t}}$ to theory as a function of m_t provides an estimate of $m_t^{\overline{\text{MS}}}$ which benefits from a higher perturbative stability compared to the extraction of m_t^{pole}. As in the case of the determination of m_t^{pole}, $m_t^{\overline{\text{MS}}}$ is extracted first assuming that the definition of m_t implemented in the MC simulation is equal to m_t^{pole} and then asumming $m_t^{\text{MC}} = m_t^{\overline{\text{MS}}}$. The results for the extracted values of $m_t^{\overline{\text{MS}}}$ are given in Table 3.4.1.

Figure 3.15 shows the measured $t\bar{t}$ cross section as a function of m_t^{pole} and $m_t^{\overline{\text{MS}}}$ together with the theoretical calculations. It has to be noticed that the Tevatron direct measurement of m_t [138] is consistent with the m_t^{pole} extraction within 2 sd while it is different by more than than 2 sd from the extracted $m_t^{\overline{\text{MS}}}$.

The same technique was used using the measured $t\bar{t}$ production cross section in the ljt by ATLAS using 35 pb^{-1}. The extraction was performed assuming $m_t^{\text{MC}} = m_t^{\text{pole}}$ and adding an uncertainty obtained by shifting m_t^{MC} by ± 1 GeV. The comparison of the predicted and the experimentally measured $t\bar{t}$ cross section as a function of m_t^{MC} is shown in Figure 3.16 as well as the summary of the extraction of m_t^{pole}.

CMS also extracted m_t^{pole} and $m_t^{\overline{\text{MS}}}$ from the $t\bar{t}$ cross section measured in the dil channel

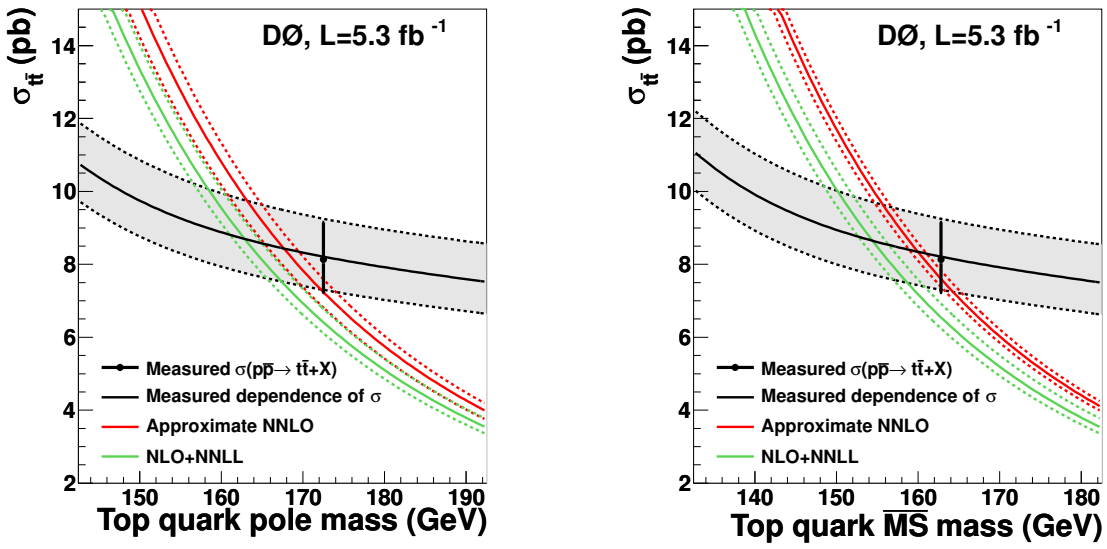

FIGURE 3.15 – Measured $\sigma_{t\bar{t}}$ with several theoretical calculations as a function of m_t^{pole} (left) and $m_t^{\overline{\text{MS}}}$ (right) asuming that $m_t^{\text{MC}} = m_t^{\text{pole}}$ [142].

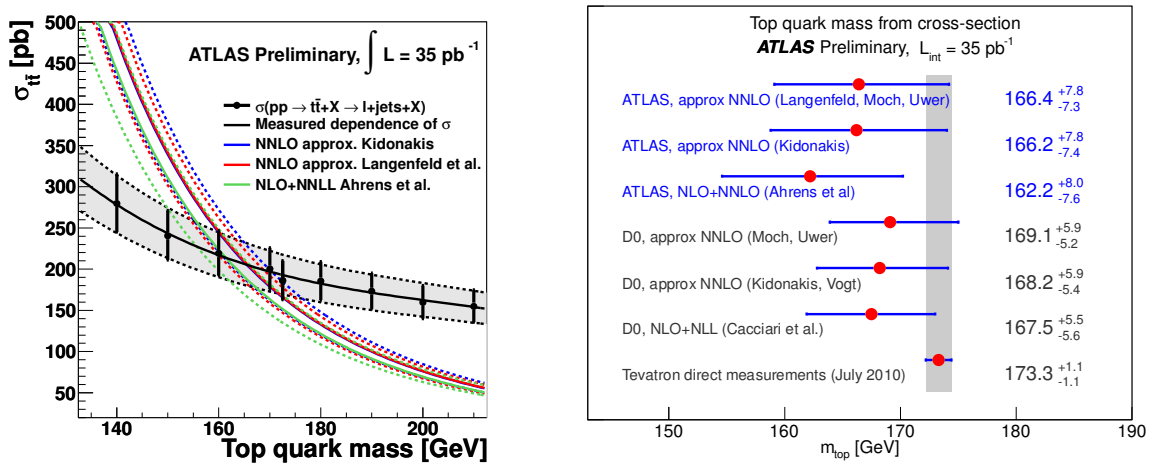

FIGURE 3.16 – (left) Predicted and measured $t\bar{t}$ production cross section as a function of m_t^{MC} in ATLAS. (right) Summary of the extraction of m_t^{pole} from the $t\bar{t}$ cross section.

with 1.14 fb^{-1}.

The precision of these results are currently limited by the uncertainty on the experimental $t\bar{t}$ cross section measurements. Further improvements on these uncertainties as well as a flatter experimental cross section dependence as a function of m_t would lead to a better precision on the mass extraction.

Combination

The world average top-quark mass is obtained from a combination of CDF and DØ most precise m_t measurements using up to 5.8 pb^{-1} of data [138]. Five measurements using data taken in an earlier run (1990-1995) and seven measurements using data from the second run (2001-2011) are used.

The combination uses the Best Linear Unbiased Estimate (BLUE) method described in [95, 96]. It consists of looking for the estimate $\hat{m}$ for the top-quark mass m that is a linear combination of the individual measurements m_i and provides an unbiased estimate of m which has the minimum possible variance σ^2 : $\hat{m} = \sum \alpha_i m_i$ with $\sum \alpha_i = 1$ where m_i are themselves unbiased ($i = 1, ..., n$). In terms of components, we can write : $\sigma^2 = \sum_i \sum_j E_{ij} \alpha_i \alpha_j$ where E_{ij} represents the variance and correlations of the i and j measurements. The BLUE technique consists of finding the n values of α_i which minimize σ^2 and satisfy $\sum \alpha_i = 1$. They can written :

$$\alpha_i = \frac{\sum_i E_{ij}^{-1}}{\sum_i \sum_j E_{ij}^{-1}}.$$

A χ^2 test can be built to measure the compatibility of the estimate $\hat{m}$ with the input measurements m_i :

$$\chi^2 = (m_i - \hat{m})^T E_{ij}^{-1} (m_j - \hat{m}).$$

Work has been performed between the two collaborations to standardize the assessment of systematic uncertainties. For the combination a detailed breakdown of the various sources of uncertainty has been established in order to properly account for correlations among the various measurements. 15 different systematic categories are used. In order to more accurately accommodate our best estimate of the relevant correlations, the jet energy scale (JES) uncertainty, for instance, is subdivided into six components (iJES, aJES, bJES, cJES, dJES and rJES). The systematic categories are shortly described below.

iJES represents the part of the JES uncertainty which originates from *in-situ* calibration procedures and is uncorrelated among the measurements. It is of statistical nature.

aJES represents the part of the JES uncertainty which originates from differences in detector electromagnetic over hadronic (e/h) response between b-jets and light-quark jets. It is correlated taken to 100% correlated among all measurements in the same experiment and same data period.

bJES contains the part of the JES uncertainty which originates from uncertainties specific to the modeling of b-jets and which is correlated across all measurements.

cJES is the part of the JES uncertainty which originates from modeling uncertainties correlated across all measurements coming from instance from modeling uncertainties associated with light-quark fragmentation and out-of-cone corrections. For DØ measurements from the second run, it is included in the dJES category since the way of estimating these uncertainties have changed.

dJES represents the part of the JES uncertainty which originates from limitations in the data samples used for calibrations and which is correlated between measurements within the same data-taking period, but not between experiments.

rJES contains the remaining part of the JES uncertainty which is correlated between all measurements of the same experiment independently from the data-taking period, but which is uncorrelated between experiments.

The **LeptPt** category contains the systematic uncertainty arising from uncertainties in the scale of lepton transverse momentum measurements. It was not considered as a source of systematic uncertainty in the Run I measurements.

The systematic uncertainty arising from uncertainties in the $t\bar{t}$ modeling which is correlated across all measurements are gathered in the **Signal** category. It contains the uncertainties from ISR/FSR, from the PDF, the systematic uncertainty associated with variations of the model for parton showers and hadronization and the uncertainty from higher order corrections. It also includes the uncertainty arising from a variation of the phenomenological description of color reconnection between final state particles.

DetMod represents the systematic uncertainty arising from uncertainties in the modeling of the detector in the MC simulation which is correlated among all measurements within the same experiment but uncorrelated between the experiments.

BGMC yields the background modeling uncertainty when it is evaluating using MC. They are correlated between all measurements in the same channel, and include uncertainties on the background composition and on normalization and shape of different components.

BGData includes uncertainties associated with the modeling of the QCD multijet or Drell-Yan background when evaluated using data. This part is uncorrelated between experiment.

Method contains the systematic uncertainty arising from any source specific to a particular fit method, including the finite Monte Carlo statistics available to calibrate each method. It is taken to be uncorrelated among the measurements.

UN/MI is specific to DØ and includes the uncertainty arising from uranium noise in the calorimeter and from the multiple interaction corrections to the JES. This was sizable only for the DØ measurements in the first run period.

MHI contains the systematic uncertainty arising from the modeling of the multiple hadron interactions, from a mismodeling of the distribution of the number of collisions per Tevatron bunch crossing.

The preliminary combined value for the top-quark mass is :

$$m_t = 173.18 \pm 0.56 \text{ (stat)} \pm 0.75 \text{ (syst) GeV},$$

which corresponds to a total uncertainty of 0.94 GeV and a relative precision of 0.54 %. The combination has a χ^2 of 8.3 for 11 degrees-of-freedom indicating good consistency among the measurements across different experiments and different decay channels. The total JES uncertainty is ± 0.49 GeV with ± 0.39 GeV coming from its statistical component and ± 0.30 GeV from the non statistical component. The largest source of systematic uncertainty comes from the uncertainty on the signal modeling : ± 0.51 GeV. The most recent CDF and DØ measurements in the ljt channel using the matrix element method carry the largest weights in the combination followed by the CDF template measurement in the *had* channel.

In the future, the statistical and *in-situ* JES related uncertainties will continue to decrease with the statistics of the data samples employed. Work is still in progress to better understand the uncertainties associated with the modeling of the $t\bar{t}$ signal from variations in MC generators and color reconnection effects. A total top-quark mass uncertainty of around 0.7-0.8 GeV is potentially achievable in the near future as can be seen in Figure 3.18.

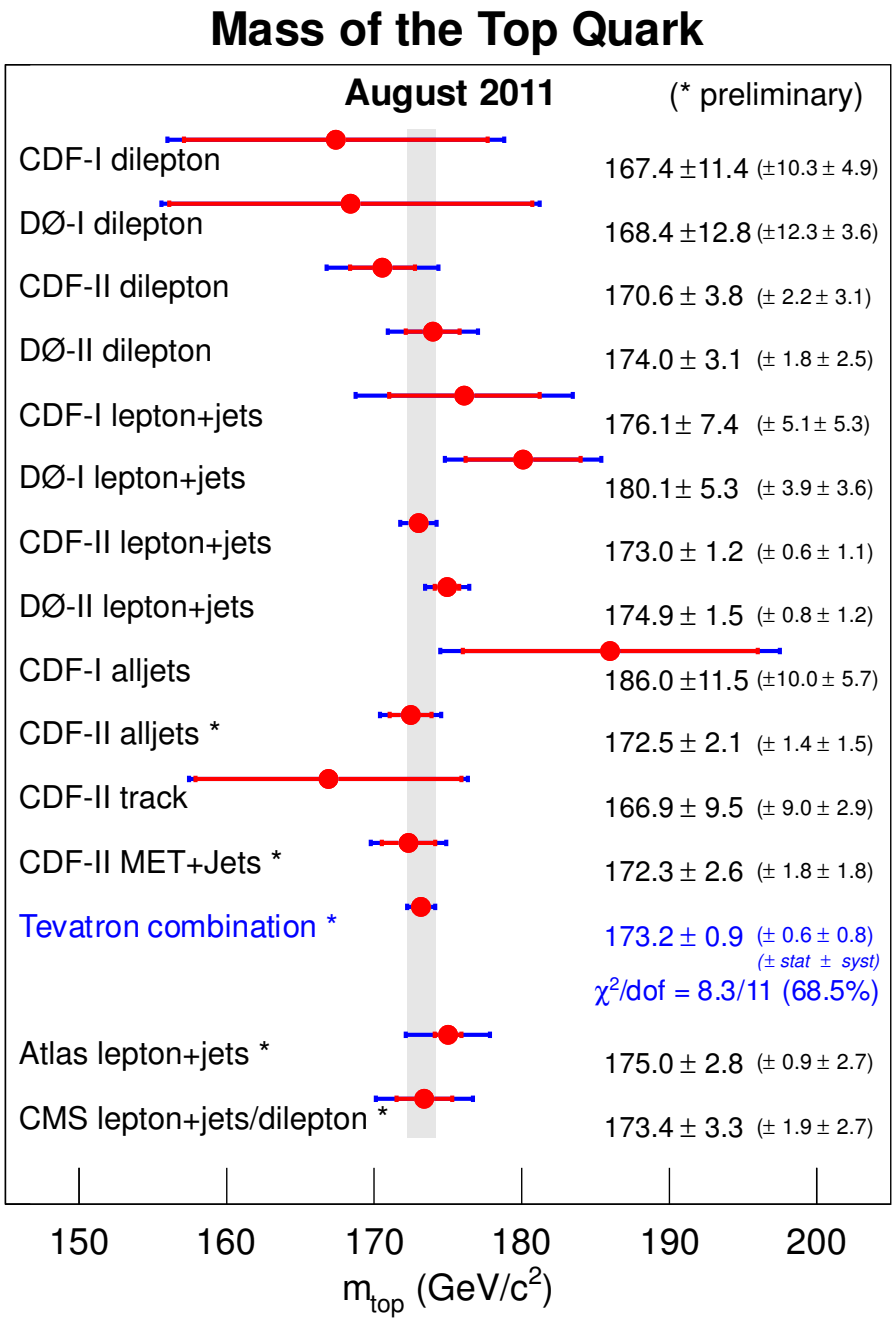

FIGURE 3.17 – Summary of the top quark mass measurements by the CDF and DØ collaborations combined to obtain the world average top quark mass [138]. The latest measurements by ATLAS and CMS are also shown.

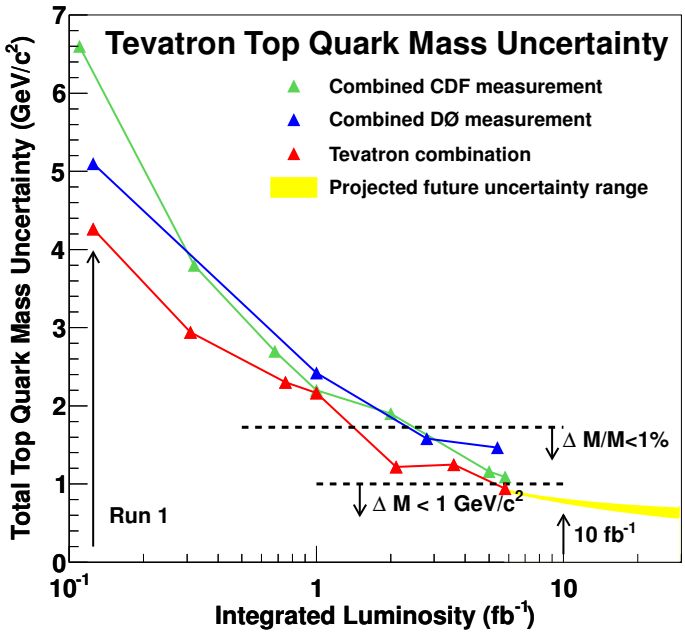

FIGURE 3.18 – Projection for the Tevatron top quark mass combined uncertainty as a function of the analyzed luminosity.

3.4.2 $t\bar{t}$ Charge Asymmetry

At lowest order in QCD, at hadron colliders the SM predicts that the top-quark pair production in $p\bar{p}$ interactions is symmetric under the exchange of t and $\bar{t}$. At NLO radiative corrections involving either virtual or real gluon emissions lead to a small charge asymmetry [151, 152, 153, 154, 155]. The dominant contribution to this asymmetry comes from the process $q\bar{q} \to t\bar{t}(g)$ from interference of the box diagram with the Born diagram (see figure 3.19) that leads to a positive asymmetry and from interference between the real emission corrections in the initial and final state (see figure 3.19) that drives the asymmetry in the opposite direction. The total asymmetry is expected to be slightly positive while the measured asymmetry depends strongly on the region of phase space being probed. So in the center of mass rest frame, the top quark is predicted to be emitted preferentially in the direction of the incoming quark while the antitop quark is rather emitted in the direction of the incoming antiquark. Similarly, the $qg \to t\bar{t}q$ process is asymmetric due to interference between amplitudes which have a relative sign under the exchange of t and $\bar{t}$. The $t\bar{t}$ production by gluon-gluon fusion $gg \to t\bar{t}$, on the other hand, is symmetric. Such asymmetry has also been observed in QED processes like $ee \to \mu\mu$ for instance, in the 80's even without any contributions from Z production.

In $p\bar{p}$ collisions at the Tevatron, top pairs are dominantly produced by quark-antiquark annihilation. Due to charge conjugation symmetry, the charge asymmetry in such collisions can also be interpreted as a top-quark forward-backward asymmetry : A_{FB}. The asymmetry A_{FB} is frame dependent and can be defined either in the $p\bar{p}$ or $t\bar{t}$ rest frame. The $t\bar{t}$ rest frame is more difficult to reconstruct but the asymmetry in the $p\bar{p}$ rest frame is predicted to

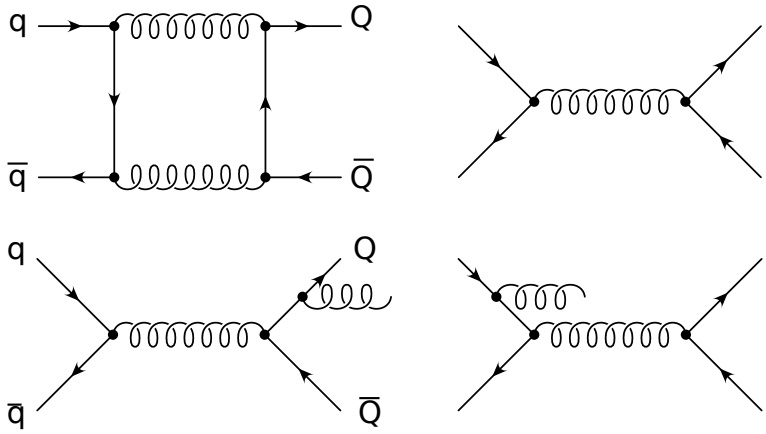

FIGURE 3.19 – (top) Feynman diagrams that interfere leading to a positive top charge asymmetry. (bottom) Feynman diagrams that interfere leading to a negative top charge asymmetry.

be ≈ 30 % smaller [156]. In the $p\overline{p}$ rest frame the asymmetry can be written as :

$$A_{FB}^{p\overline{p}} = \frac{N_t(\cos\theta > 0) - N_t(\cos\theta < 0)}{N_t(\cos\theta > 0) + N_t(\cos\theta < 0)} \tag{3.20}$$

where $\cos\theta = -Q_\ell \cdot \cos\alpha_p$, α_p is the polar angle between the top quark with the hadronic W-boson decay and the proton beam, and Q_ℓ is the lepton charge from the leptonic decaying W-boson. In the $t\overline{t}$ rest frame the asymmetry can be defined similarly except that θ^* is the production angle of the top quark in the $t\overline{t}$ rest frame. This angle is related to the rapidity, y, of the t and $\overline{t}$ in the $p\overline{p}$ frame by

$$\Delta y = y_t - y_{\overline{t}} = 2\tan^{-1}\left(\frac{\cos\theta^*}{\sqrt{1 + \frac{4m_t^2}{\hat{s} - 4m_t^2}}}\right) \tag{3.21}$$

where $\hat{s}$ is the square of the center-of-mass energy, while Δy is Lorentz invariant. So the $t\overline{t}$ rapidity difference in the $p\overline{p}$ rest frame can be used to measure the production angle θ^* in the $t\overline{t}$ rest frame. As both Δy and $\cos\theta^*$ have the same sign, the asymmetry can be written

$$A_{FB}^{t\overline{t}} = \frac{N(\Delta y > 0) - N(\Delta y < 0)}{N(\Delta y > 0) + N(\Delta y < 0)}. \tag{3.22}$$

At the LHC with 7 TeV pp collisions, the dominant mechanism for $t\overline{t}$ production is expected to be the gluon-gluon fusion process, while $t\overline{t}$ production via $q\overline{q}$ or qg is small. In addition, the directions of the initial state quark and antiquark are not known. However, because of the same asymmetry in the production via $q\bar{q}$ and qg, QCD predicts at the LHC a small excess of centrally produced antitop quarks while top quarks are produced, on average, at higher absolute rapidities. This can be understood by the fact that for $t\overline{t}$ production via $q\overline{q}$ annihilation the valence quark carries, on average, a larger momentum fraction than the anti-quark from the sea. With top quarks preferentially emitted in the direction of the initial

quarks in the $t\bar{t}$ rest frame, the boost into the laboratory frame drives the top mainly in the forward or backward directions, while antitops are kept more in the central region. In that case a possible observable at the LHC is :

$$A_C = \frac{N(\Delta|y| > 0) - N(\Delta|y| < 0)}{N(\Delta|y| > 0) + N(\Delta|y| < 0)} \tag{3.23}$$

where $\Delta|y| = |y_t| - |y_{\bar{t}}|$. The pseudorapidity η could also be used instead of the rapidity y.

Instead of looking at the asymmetry from the top quarks, it is also possible to look at the asymmetry using the lepton from the top quark decays either in the ljt or dil channels. This has the advantage that no reconstruction of the top final state is necessary but the drawback is that the asymmetry is diluted. As we will see below, a lepton based asymmetry is also sensitive to top-quark polarization effects. At the Tevatron, the leptonic based asymmetry can be defined in the ljt channel as :

$$A^{\ell}_{FB} = \frac{N(Q_\ell y_\ell > 0) - N(Q_\ell y_\ell < 0)}{N(Q_\ell y_\ell > 0) + N(Q_\ell y_\ell < 0)}, \tag{3.24}$$

or using dil events as :

$$A^{\ell\ell}_{FB} = \frac{N(\Delta\eta > 0) - N(\Delta\eta < 0)}{N(\Delta\eta > 0) + N(\Delta\eta < 0)}, \tag{3.25}$$

with $\Delta\eta = \eta_{\ell^+} - \eta_{\ell^-}$. In a similar way, at the LHC, the lepton based asymmetry can be defined with the difference in absolute values of the lepton pseudorapidity for dil events.

Within the SM, the leading order QCD contribution has been computed in [151, 152]. It is the ratio of the asymmetric $t\bar{t}$ cross section ($\sigma_A = \int_{y_t>0} \frac{d\sigma}{dy_t} - \int_{y_t<0} \frac{d\sigma}{dy_t}$) over the inclusive cross section which is symmetric ($\sigma_S = \int_{y_t>0} \frac{d\sigma}{dy_t} + \int_{y_t<0} \frac{d\sigma}{dy_t}$). As this is a NLO effect, the first non-vanishing term of σ_A is of order α_s^3 while the leading term in σ_S is of order α_s^2. The NLO computation leads to an asymmetry of around $A^{t\bar{t}}_{FB} \approx 7\%$ at the Tevatron and around $A^{\Delta y}_C \approx$ 1 % at the LHC. When evaluating using MC, the asymmetry is often normalized to the NLO cross section (i.e. with the denominator expanded one order higher in α_s than the numerator). In that case, the prediction from MC would be 1.3 lower than the SM prediction normalized to the Born cross section. In addition to the leading QCD contributions, mixed QCD and electroweak corrections to the asymmetry has been evaluated [153, 155] which can enhance SM predictions by around 20% at the Tevatron and around 13 % at the LHC. The inclusion of soft-gluon resummation affects the NLO prediction by only a few % [82, 154, 157, 158]. The small value predicted by QCD for the asymmetry within the SM makes its measurement a powerful test of QCD and a sensitive probe to new physics.

At detector level, the raw asymmetry is extracted from data after background substraction. The results by CDF [159], DØ [160] and the CMS preliminary result using 1.1 fb^{-1} are summarized on Table 3.8 using ljt events together with the prediction from MC@NLO [161]. It can be seen that the measurements are up to 2 sd higher than the MC predictions. However, because of distortions by different acceptance cuts and detector effects, these results can not be compared. The results are corrected to the parton level using unfolding techniques. The relation between a true distribution T_j and the reconstructed distribution S_i after detector simulation and event selection can be written :

$$S_i = \sum_j R_{ij} T_j \tag{3.26}$$

	Raw Asymmetry	Predictions (MC@NLO)
CDF	$A_{\mathrm{FB}}^{t\bar{t}} = 7.5 \pm 3.7\%$	$2.4 \pm 0.5\%$
DØ	$A_{\mathrm{FB}}^{t\bar{t}} = 9.2 \pm 3.7\%$	$2.4 \pm 0.7\%$
CMS	$A_C^{\Delta\eta} = -0.4 \pm 0.9\%$	-

Table 3.8 – Detector level top charge asymmetry after background substraction measured in CDF [159], DØ [160] and CMS [162] together with the predictions from MC@NLO.

	Unfolded Asymmetry	Predictions
CDF	$A_{\mathrm{FB}}^{t\bar{t}} = 15.8 \pm 7.2(\mathrm{stat}) \pm 1.7(\mathrm{syst})\%$	$A_{\mathrm{MCFM}} = 5.8 \pm 0.9\%$
DØ	$A_{\mathrm{FB}}^{t\bar{t}} = 19.6 \pm 6.0(\mathrm{stat})^{+1.8}_{-2.6}(\mathrm{syst})\%$	$A_{\mathrm{MC@NLO}} = 5.0 \pm 0.1\%$
Atlas	$A_C^{\Delta y} = -2.4 \pm 1.6(\mathrm{stat}) \pm 2.3(\mathrm{syst})\%$	$A_{\mathrm{MC@NLO}} = 0.6\%$
CMS	$A_C^{\Delta\eta} = -1.7 \pm 3.2(\mathrm{stat})^{+2.5}_{-3.6}(\mathrm{syst})\%$	$A_{\mathrm{theo}} = 1.3 \pm 0.1\%$

Table 3.9 – Top charge asymmetry corrected for acceptance and detector effects measured by CDF [159], DØ [160], ATLAS and CMS [162] together with the predictions.

where R_{ij} is the the response matrix defined as the probability to get an observed event in bin i when it is expected in bin j. The true distribution T_j can be obtained from the observed distribution S_i by inverting the response matrix. In general, unfolding histograms where the bin width is smaller than the experimental resolution is unstable with respect to statistical fluctuations in the data. Regularization techniques are employed to suppress such fluctuations by smoothing the unfolded results. Different methods to approach this matrix inversion as well as regularization are employed by the different experiments. The results in the ljt final state at the production level, i.e. after unfolding, are summarized in Table 3.9 together with the MC predictions. The Tevatron results are up to 2.4 sd higher than these predictions. It has also to be noticed that the Tevatron results which use 5.4 fb^{-1} of data are still limited statistics. The raw and unfolded $\Delta|y|$ distributions measured in ATLAS using 0.7 fb^{-1} in the $e + jets$ channel are shown in Figure 3.20.

As several variables like for instance the invariant $t\bar{t}$ mass ($m_{t\bar{t}}$), the number of jets or Δy itself can influence the asymmetry within the SM or in case new physics would be present, it is useful to measure the asymmetry as a function of these variables, in particular as a function of $m_{t\bar{t}}$. It was performed at the Tevatron in two bins of $m_{t\bar{t}}$ below and above 450 GeV at the reconstruction level and also after unfolding by CDF [159]. The results at the reconstruction level are summarized in Figure 3.21. CDF measurement discrepances at the level of 3 sd. with the prediction at high invariant mass. This difference is not observed by DØ. CMS also performed a measurement of $A_C^{\Delta\eta}$ as a function of $m_{t\bar{t}}$ at the raw level which does not show any difference with the MC prediction within the uncertainties.

DØ also pointed out in [160] that the forward-backward asymmetry can be correlated with the p_T of the $t\bar{t}$ pair and that the predicted dependence is rather different in the various MC generator or generator tunes. As the $t\bar{t}$ p_T distribution is not well modeled in DØ data by MC@NLO, a better understanding of the MC predictions would be desirable.

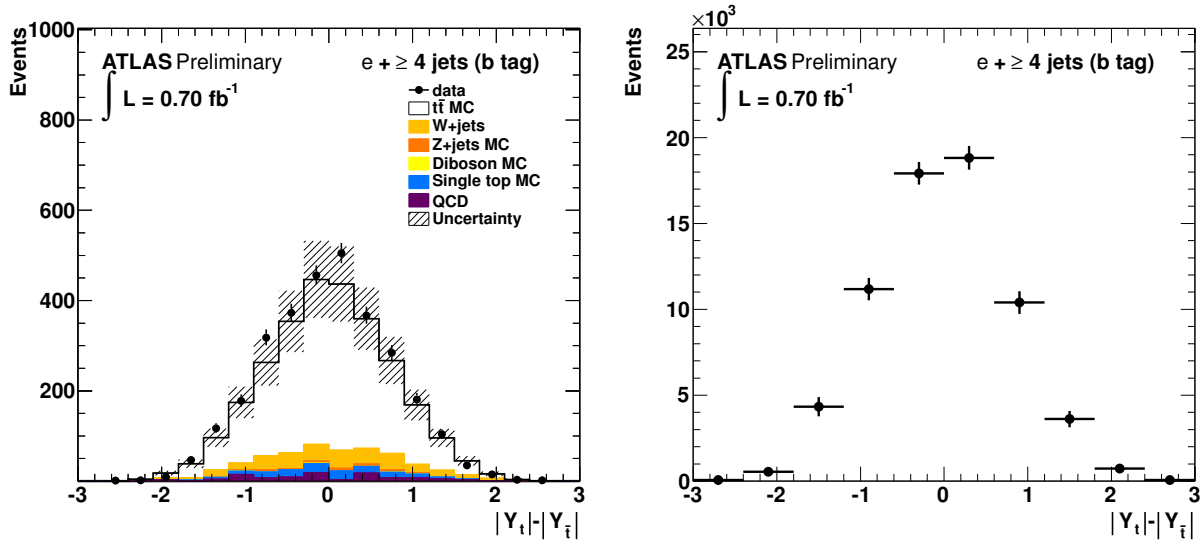

FIGURE 3.20 – $e + jets$ $\Delta|y|$ distribution before (left) and after (right) unfolding measured in ATLAS using 0.7 fb^{-1}.

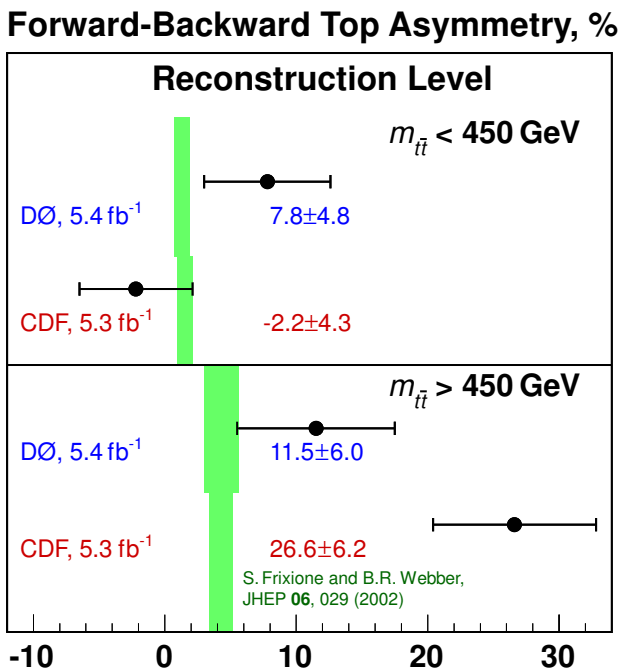

FIGURE 3.21 – Summary of the CDF [159] and DØ [160] A_{FB} measurements at the detector level in two $m_{t\bar{t}}$ bins.

As discussed above, there are currently some tensions between the SM and MC predictions on the one hand and the measurements at Tevatron on the other hand, especially with the CDF measurement for high $m_{t\bar{t}}$. Even if these predictions have some limitations as we

presented above, these discrepancies have recently led to some excitations in the community and numerous BSM scenarii to explain the observed discrepancies have been proposed [163, 164, 165, 69, 68, 166, 167, 168, 169, 170, 171].

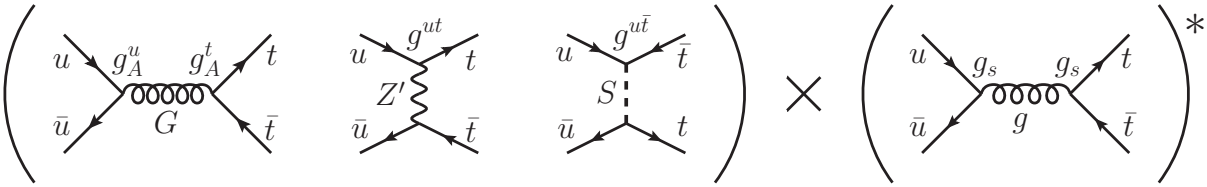

FIGURE 3.22 – Feynman diagrams for BSM processes that could lead to an enhancement of the charge asymmetry with respect to the SM prediction [172]

In addition to create a larger charge asymmetry than in the SM, all possible new physics models should preserve the agreement between predictions and measurements of the total $t\bar{t}$ cross section and of the $m_{t\bar{t}}$ distribution (up to the invariant mass observed so far). Three main classes of models, as shown in Figure 3.22, have been advertized to enhance the asymmetry value beyond the SM prediction : models that predict the s-channel exchange of a new color-octet vector particle, models where a new Z' or W' color-singlet vector bosons or a color-single scalar doublet interacts with the top quarks in the t-channel and scenarii where a color-triplet or sextet scalar is exchanged in the u-channel. We will shortly give some more details about these different possibilities in the following.

Models like chiral color which extends the QCD gauge group [173] or models with Randal-Sundrum extra-dimensions can predict the existence of new color-octet vector bosons, that are often called axigluons. Constraints on the ratio of axigluon coupling to its mass arise from $t\bar{t}$ cross section measurements. Axigluon could also affect simultaneously dijet production. The current LHC limits on dijet bounds can however be relaxed by decreasing the axigluon couplings to light quark. Light axigluons are constrained by the absence of observed $t\bar{t}$ resonance in $t\bar{t}$ production. This can be overcome by models with large width axigluons.

Heavy Z' or W' are predicted by models of topcolor-assisted technicolor for instance. Since the inteference with SM gluon is negative, large couplings are needed to achieve a large asymmetry. Strong constraints for such models arise from limit on same-sign top production at the LHC.

The exchange of new scalar fields in the u-channel could also lead to an enhancement of the charge asymmetry. Such color-tripet or color-sextet scalar appear in models with an extended Higgs sector. Dijet production at the LHC strongly limits the existence of a color-sextet scalar.

In order to accomodate a not too high $t\bar{t}$ cross section at the Tevatron and a not too large tail in the $t\bar{t}$ spectrum, it seems that Z' or W' models are rather disfavored and that axigluons must be rather heavy and strongly coupled [171, 174]. The asymmetry variation as a function of $m_{t\bar{t}}$ provides a tool to discriminant between different BSM models. It has been shown in [175] for instance that a lot of different asymmetry profiles versus $m_{t\bar{t}}$ could be created depending on the model parameters.

The leptonic asymmetries give another handle to understand the asymmetry picture. CDF measured the asymmetry in the *dil* channel using 5.1 fb^{-1} by both exploring the

lepton-based asymmetry as defined in Eq. 3.25 and reconstructing the top quark final state leading to the following preliminary result after unfolding : $A_{FB}^{t\bar{t}} = 0.42 \pm 0.15(\text{stat}) \pm 0.05(\text{syst})$. This result is around 2.3 sd higher than the SM predictions. DØ measured the lepton-based asymmetry in the ljt final state using Eq. 3.24 with 5.4 fb^{-1}. Even if, in that case, the asymmetry is diluted due to the top quark decay, this measurement is less prompt to unfolding effects. The production level asymmetry is found to be : $A_{FB}^{\ell} = 0.152 \pm 4.0(\text{stat})^{+1.0}_{-1.3}(\text{syst})$ [160] which is more than 3 sd away from the SM prediction.

Clearly the experimental measurements of the $t\bar{t}$ charge asymmetry are currently puzzling. Updated measurements with the full dataset at the Tevatron as well as with more luminosity at the LHC should be able to sort out the origin of the current discrepancy. In order to do so, several alternative observables have been proposed the increase the sensitivity at the LHC, mainly in enhancing the $q\bar{q}$ fraction in $t\bar{t}$ production at the cost of loosing some statistics. A lot of proposals exist such as looking at only forward or central rapidities [176], at central leptonic and forward hadronic top rapidities [177] or at boosted asymmetry [178]. As already noticed above, measuring the asymmetry as a function of the number of jets, versus the $t\bar{t}$ p_T or $m_{t\bar{t}}$ would help to bring useful informations. Another related measurement that could help to understand the nature of the produced asymmetry is the top-quark polarization. Indeed in many BSM scenarii, new particles that lead to large asymmetries couple only to right-handed top quarks and hence would predict a large polarization of the produced top quarks. Such effects would influence in particular the leptonic asymmetries since lepton angular distributions would carry informations from both the production asymmetry and from the top quark polarization. As QCD produces unpolarized top quarks, such observables would help to discrimination between different hypothetical BSM models [179, 180]. It was also proposed to look at the leptonic asymmetry at threshold [181] in the low $m_{t\bar{t}}$ region. Definitely asymmetry measurements would remain an exciting part of the top-quark physics program at hadron colliders in the years to come.

3.5 Conclusion and Perspectives

Owing to its large mass, the top quark offers a unique window into Beyond-the-Standard-Model physics. Using data samples with $\mathcal{O}(10^3)$ candidate $t\bar{t}$ events, the CDF and DØ experiments at the Fermilab Tevatron have pioneered numerous analyses to exploit these unique events. They have instituted a broad physics program that tests the Standard Model descriptions of the $t\bar{t}$ production mechanisms, the top-quark decay widths, and the intrinsic properties of the top quark such as its electric charge and mass. A few of the measurements are systematics limited and have reached precisions comparable to those associated with the relevant theory predictions, such as the measured production cross section and the measured top-quark mass. Numerous top quark properties have been already measured allowing to better understand this unique quark and to test the SM at the electroweak scale. These measurements are summarized in Table 3.10. With the exception of the puzzling top charge asymmetry, no deviations from the SM predictions have been observed. However only half of the Tevatron dataset has been analyzed so far. The Tevatron experiments are now concentrated on their legacy measurements ($t\bar{t}$ differential cross-section, s-channel single top cross section, $t\bar{t}$ spin correlation, $t\bar{t}$ forward-backward asymmetry and top quark mass).

With a $t\bar{t}$ cross section 20 times higher, the LHC experiments collected $t\bar{t}$ samples that are already larger that the Tevatron statistics. With these sorts of statistics most all the measurements should achieve levels of precision that more thoroughly probe the Standard Model expectations and more stringently restrict the parameter space of a wide variety of new physics models. Even for those measurements already systematics limited at the Tevatron, the LHC experiments may be able to exploit the larger statistics to identify a sub-set of events less affected by the systematics in question or to employ analysis techniques which trade statistical uncertainties for systematic uncertainties to achieve an improvement in the total uncertainty. The current LHC measurements are also summarized in Table 3.10. A lot of more precise measurements are expected when analyzing several fb^{-1} of LHC data with exciting time ahead of us.

Property		Measurement	SM	L (fb^{-1})
$\sigma_{t\bar{t}}$	$p\bar{p} \to t\bar{t}$	CDF : $7.5 \pm 0.31(\text{stat}) \pm 0.34(\text{syst}) \pm 0.15(\text{th})$ pb	$7.46^{+0.48}_{-0.67}$ pb	up to 4.6
($M_t = 172.5$ GeV)		D0 : $7.56^{+0.63}_{-0.56}$ (stat + syst + lumi) pb		5.6
	$pp \to t\bar{t}$	Atlas : $179.0 \pm 9.8(\text{stat} + \text{syst}) \pm 6.6(\text{lumi})$ pb	$164.6^{+11.4}_{-15.7}$ pb	0.7
		CMS : $166 \pm 2(\text{stat}) \pm 11(\text{syst}) \pm 8(\text{lumi})$ pb		up to 1.1
σ_{tbq}	$p\bar{p} \to t\bar{t}$	CDF : 0.8 ± 0.4 pb ($M_t = 175$ GeV)	2.26 ± 0.12 pb	3.2
($M_t = 172.5$ GeV)		D0 : 2.90 ± 0.59 pb		5.4
	$pp \to t\bar{t}$	Atlas : 90^{+32}_{-22} pb	$64.6^{+3.3}_{-2.6}$ pb	0.7
		CMS : $83.6 \pm 29.8(\text{stat} + \text{syst}) \pm 3.3(\text{lumi})$ pb		0.035
σ_{tb}	$p\bar{p} \to t\bar{t}$	CDF : $1.8^{+0.7}_{-0.5}$ pb ($M_t = 175$ GeV)	1.04 ± 0.04 pb	3.2
($M_t = 172.5$ GeV)		D0 : $0.68^{+0.38}_{-0.35}$ pb		5.4
	$pp \to tb$	Atlas : < 26.5 pb		0.7
σ_{Wt}	$pp \to t\bar{t}$	Atlas : < 39.1 pb	15.7 ± 1.4 pb	0.7
($M_t = 172.5$ GeV)		CMS : $22^{+9}_{-7}(\text{stat} + \text{sys})$ pb		2.1
$\sigma_{t\bar{t}\gamma}$	$p\bar{p} \to t\bar{t}\gamma$	CDF : $0.18 \pm 0.08(\text{stat} + \text{syst} + \text{lumi})$ pb	0.17 ± 0.03 pb	6.0
($M_t = 172.5$ GeV)	$pp \to t\bar{t}\gamma$	Atlas : $2.0 \pm 0.5(\text{stat}) \pm 0.7(\text{syst}) \pm 0.08(\text{lumi})$ pb	2.1 ± 0.4 pb	1.0
$\lvert V_{tb} \rvert$		CDF : $\lvert V_{tb} \rvert = 0.91 \pm 0.11(\text{stat} + \text{sys}) \pm 0.07(\text{th})$	1	3.2
		D0 : $\lvert V_{tb} \rvert = 1.02^{+0.10}_{-0.11}$		5.4
$\frac{B(t \to Wb)}{B(t \to Wq)}$		CDF : > 0.61 @ 95% CL	1	0.2
		D0 : 0.90 ± 0.04		5.4
$\frac{\sigma(gg \to t\bar{t})}{\sigma(p\bar{p} \to t\bar{t})}$	$p\bar{p} \to t\bar{t}$	CDF : $0.07^{+0.15}_{-0.07}$	0.18	1
M_t		Tev : 173.2 ± 0.9 GeV	-	up to 5.8
		Atlas : 175.9 ± 2.8 GeV	-	0.7
		CMS : 173.4 ± 3.3 GeV	-	0.036
$M_t - M_{\bar{t}}$		CDF : $-3.3 \pm 1.4(\text{stat}) \pm 1.0(\text{syst})$ GeV	0	5.6
		D0 : $0.8 \pm 1.8(\text{stat}) \pm 0.5(\text{syst})$ GeV		3.6
		CMS : $-1.2 \pm 1.2(\text{stat}) \pm 0.5(\text{syst})$ GeV		1.1
W helicity		Tev : $f_0 = 0.732 \pm 0.063(\text{stat}) \pm 0.052(\text{syst})$	0.7	up to 5.4
fraction		Atlas : $f_0 = 0.75 \pm 0.08(\text{stat} + \text{syst})$	0.7	0.7
Charge		CDF : -4/3 excluded @ 95% CL	2/3	5.6
		D0 : $\lvert q \rvert = 4/3$ excluded @ 92% CL		0.37
		Atlas : -4/3 excluded @ more than 5 σ		0.7
Γ_t		CDF : < 7.6 GeV @ 95% CL	1.26 GeV	4.3
		D0 : $1.99^{+0.69}_{-0.55}$ GeV		up to 2.3
Spin	$p\bar{p} \to t\bar{t}$	CDF : $C_{\text{beam}} = 0.72 \pm 0.64(\text{stat}) \pm 0.26(\text{syst})$	$0.777^{+0.027}_{-0.042}$	5.3
correlation		D0 : $C_{\text{beam}} = 0.66 \pm 0.23(\text{stat} + \text{sys})$		5.4
	$pp \to t\bar{t}$	Atlas : $C_{hel} = 0.34^{+0.15}_{-0.11}$	0.32	0.7
Charge	$p\bar{p} \to t\bar{t}$	CDF : 0.158 ± 0.074	0.06	5.3
asymmetry		D0 : 0.196 ± 0.065		5.4
	$pp \to t\bar{t}$	Atlas : $A_C^y = -0.024 \pm 0.016(\text{stat}) \pm 0.023(\text{syst})$	0.006	0.7
		CMS : $A_C^\eta = -0.017 \pm 0.032(\text{stat})^{+0.025}_{-0.036}(\text{syst})$	0.013	1.1

TABLE 3.10 – Summary of the main top quark properties (December 2011)

Conclusion

After the end of the LEP area, the last decade has been the Tevatron time. The Run II of the Tevatron from 2001 to 2011 has allowed to further and extensively test the Standard Model of particle physics. In particular during this period, the oscillation of B_S mesons and the electroweak production of the top quark were discovered. The masses of the W boson and of the top quark have been measured with the world best precision. The possible mass range for the Higgs boson has also been further constrainted for the first time after LEP. In addition, almost all what we know currently about the top quark mass is coming from the Tevatron analyses. Since 2010 the LHC is working extremely well, producing impressive results by testing possible new physics models, schrinking the allowed Higgs mass range and starting precision measurements in electroweak and top quark physics. Even if some of the top quark properties will still be complementarily measured with the $p\overline{p}$ Tevatron full dataset, as anticipated, the LHC is a top quark factory and will bring the study of the top quark at an unpreceding level in the year to come.

My scientific course in the last 10 years has followed the start-up period, the development, heights and end of Tevatron Run II. After finalizing and optimizing the reconstruction software at DØ, it has been necessary to develop tools to measure the performance of the object identification, in particular for muons. The measurement of standard candle like the $W \to \mu\nu$ inclusive cross section has enabled to verify that the full analysis chain was working properly. Certification procedures and improvements of the identification have then been necessary to increase the quality of the physics analyses. Setting up common analysis format, tools and samples have also allowed to further improve the scientific productivity of the DØ collaboration. All these tools have made the precise measurements of numerous top quark properties possible. With the increasing DØ dataset over the years and the analysis improvements, the measurements of the $t\overline{t}$ cross section and of the top quark mass in the clean dilepton channel are not limited anymore by the statistical uncertainty. For the legacy measurements using the full Tevatron dataset, work on improving the systematic uncertainties is continuing. The striking measurement of the $t\overline{t}$ forward-backward asymmetry at the Tevatron is however still statistically limited. So the analysis of the full dataset is important to help getting a final answer about the current difference between the experimental measurements and predictions from the Standard Model. With its enormous dataset and even if it is expected to be different and smaller than at the Tevatron, the LHC will bring important inputs to conclude on the current puzzling $t\overline{t}$ charge asymmetry picture.

I am looking forward for exciting discoveries in the top quark sector in the near future.

References

[1] F. Deliot (2002), Ph.D. Thesis (advisor : Claude Guyot), FERMILAB-THESIS-2002-12.

[2] S. Abachi et al. (D0 Collaboration), Nucl.Instrum.Meth. **A338**, 185 (1994).

[3] V. Abazov et al. (D0 Collaboration), Nucl.Instrum.Meth. **A565**, 463 (2006), `physics/0507191`.

[4] B. Tuchming (2010), habilitation à diriger des recherches, Université Paris-Diderot (Paris 7).

[5] V. Abazov, B. S. Acharya, G. Alexeev, G. Alkhazov, V. Anosov, et al., Nucl.Instrum.Meth. **A552**, 372 (2005a), `physics/0503151`.

[6] S. Chevalier-Thery (2010), Ph.D. Thesis (advisors : Ursula Bassler, Frederic Deliot), FERMILAB-THESIS-2010-26.

[7] M. Arthaud (2008), Ph.D. Thesis (advisors : Didier Vilanova, Frederic Deliot), FERMILAB-THESIS-2008-73.

[8] A. Mathieu et al. (D0) (2003), DØ Conference Note 4128.

[9] F. Deliot et al. (D0) (2005), DØ Conference Note 4750.

[10] G. Arnison et al. (UA1 Collaboration), Phys.Lett. **B126**, 398 (1983).

[11] M. Banner et al. (UA2 Collaboration), Phys.Lett. **B122**, 476 (1983).

[12] T. Sjöstrand, P. Eden, C. Friberg, L. Lönnblad, G. Miu, S. Mrenna, and E. Norrbin, Comput.Phys.Commun. **135**, 238 (2001), see also http ://home.thep.lu.se/ torbjorn/Pythia.html, `0010017`.

[13] G. Davidson, N. Nanava, T. Przedzinski, E. Richter-Was, and Z. Was (2010), iFJPAN-IV-2009-10 ; see also http ://wasm.home.cern.ch/wasm/goodies.html, `1002.0543`.

[14] T. Andeen et al. (D0 Run II Collaboration) (2007), FERMILAB-TM-2365.

[15] R. Hamberg, W. L. van Neerven, and T. Matsuura, Nucl. Phys. **B359**, 343 (1991).

[16] J. Pumplin, D. Stump, J. Huston, H. Lai, P. Nadolsky, and W. Tung (CTEQ), JHEP **07**, 012 (2002), see also http ://www.phys.psu.edu/ cteq, `0201195`.

[17] F. Deliot and D. A. Glenzinski (2010), `1010.1202`.

[18] S. Herb et al., Phys.Rev.Lett. **39**, 252 (1997).

[19] F. Abe et al. (CDF), Phys.Rev.Lett. **73**, 225 (1994), `9405005`.

[20] F. Abe et al. (CDF), Phys.Rev.Lett. **74**, 2626 (1995), `9503002`.

[21] S. Abachi et al. (D0), Phys.Rev.Lett. **74**, 2632 (1995), `9503003`.

[22] D. Schaile and P. Zerwas, Phys.Rev. **D45**, 3262 (1992).

[23] K. Nakamura et al. (Particle Data Group), J.Phys.G **G37**, 075021 (2010).

[24] M. Jezabek and J. Kühn, Phys.Rev. **D48**, 1910 (1993), 9302295.

[25] M. Jezabek and J. Kühn, Phys.Rev. **D48**, 4970 (1994).

[26] G. Abbiendi et al., Eur.Phys.J **C45**, 291 (2006), 0508062.

[27] C. Quigg, Ann.Rev.Nucl.Part.Sci. **59**, 505 (2009), 0905.3187.

[28] C. T. Hill and S. J. Parke, Phys. Rev. **D49**, 4454 (1994), hep-ph/9312324.

[29] H. P. Nilles, Phys. Rept. **110**, 1 (1984).

[30] H. E. Haber and G. L. Kane, Phys. Rept. **117**, 75 (1985).

[31] S. P. Martin (1997), hep-ph/9709356.

[32] D. Chung, L. Everett, G. Kane, S. King, J. Lykken, and L. Wang, Phys. Rep. **407**, 1 (2005).

[33] Y. Grossman, Nucl. Phys. **B426**, 355 (1994), hep-ph/9401311.

[34] E. Eichten and K. D. Lane, Phys. Lett. **B90**, 125 (1980).

[35] E. Eichten, I. Hinchliffe, K. D. Lane, and C. Quigg, Phys. Rev. **D34**, 1547 (1986).

[36] C. T. Hill, Phys. Lett. **B266**, 419 (1991).

[37] C. T. Hill, Phys. Lett. **B345**, 483 (1995), hep-ph/9411426.

[38] E. H. Simmons, Phys. Rev. **D55**, 1678 (1997), hep-ph/9608269.

[39] R. S. Chivukula, A. G. Cohen, and E. H. Simmons, Phys. Lett. **B380**, 92 (1996), hep-ph/9603311.

[40] D. Choudhury, R. M. Godbole, R. K. Singh, and K. Wagh, Phys. Lett. **B657**, 69 (2007), 0705.1499.

[41] I. Antoniadis, K. Benakli, and M. Quiros, Phys. Lett. **B331**, 313 (1994), hep-ph/9403290.

[42] K. R. Dienes, E. Dudas, and T. Gherghetta, Phys. Lett. **B436**, 55 (1998), hep-ph/9803466.

[43] K. R. Dienes, E. Dudas, and T. Gherghetta, Nucl. Phys. **B537**, 47 (1999), hep-ph/9806292.

[44] I. Antoniadis, K. Benakli, and M. Quiros, Phys. Lett. **B460**, 176 (1999), hep-ph/9905311.

[45] T. G. Rizzo and J. D. Wells, Phys. Rev. **D61**, 016007 (2000), hep-ph/9906234.

[46] K.-M. Cheung and G. L. Landsberg, Phys. Rev. **D65**, 076003 (2002), hep-ph/0110346.

[47] T. Appelquist, H.-C. Cheng, and B. A. Dobrescu, Phys. Rev. **D64**, 035002 (2001), hep-ph/0012100.

[48] H.-C. Cheng, K. T. Matchev, and M. Schmaltz, Phys. Rev. **D66**, 056006 (2002), hep-ph/0205314.

[49] T. G. Rizzo, Phys. Rev. **D64**, 095010 (2001), hep-ph/0106336.

[50] L. Randall and R. Sundrum, Phys. Rev. Lett. **83**, 3370 (1999), hep-ph/9905221.

[51] H. Davoudiasl, J. L. Hewett, and T. G. Rizzo, Phys. Rev. **D63**, 075004 (2001), hep-ph/0006041.

[52] H. Davoudiasl, J. L. Hewett, and T. G. Rizzo, Phys. Lett. **B473**, 43 (2000), hep-ph/9911262.

[53] Y. Grossman and M. Neubert, Phys. Lett. **B474**, 361 (2000), hep-ph/9912408.

[54] A. Pomarol, Phys. Lett. **B486**, 153 (2000), hep-ph/9911294.

[55] S. Chang, J. Hisano, H. Nakano, N. Okada, and M. Yamaguchi, Phys. Rev. **D62**, 084025 (2000), hep-ph/9912498.

[56] L. Randall and M. D. Schwartz, JHEP **11**, 003 (2001), hep-th/0108114.

[57] S. J. Huber and Q. Shafi, Phys. Rev. **D63**, 045010 (2001), hep-ph/0005286.

[58] L. Randall and M. D. Schwartz, Phys. Rev. Lett. **88**, 081801 (2002), hep-th/0108115.

[59] C. Csaki, J. Erlich, and J. Terning, Phys. Rev. **D66**, 064021 (2002), hep-ph/0203034.

[60] J. L. Hewett, F. J. Petriello, and T. G. Rizzo, JHEP **09**, 030 (2002), hep-ph/0203091.

[61] K. Agashe, A. Delgado, M. J. May, and R. Sundrum, JHEP **08**, 050 (2003), hep-ph/0308036.

[62] P. Langacker, Phys. Rept. **72**, 185 (1981).

[63] T. Han, H. E. Logan, B. McElrath, and L.-T. Wang, Phys. Lett. **B563**, 191 (2003), hep-ph/0302188.

[64] B. A. Dobrescu and C. T. Hill, Phys. Rev. Lett. **81**, 2634 (1998), hep-ph/9712319.

[65] J. A. Aguilar-Saavedra, Acta Phys. Polon. **B35**, 2695 (2004), hep-ph/0409342.

[66] G. L. Kane, G. A. Ladinsky, and C. P. Yuan, Phys. Rev. **D45**, 124 (1992).

[67] J. Cao, Z. Heng, L. Wu, and J. M. Yang, Phys. Rev. **D81**, 014016 (2010), 0912.1447.

[68] J. Shu, T. M. P. Tait, and K. Wang, Phys. Rev. **D81**, 034012 (2010), 0911.3237.

[69] K. Cheung, W.-Y. Keung, and T.-C. Yuan, Phys. Lett. **B682**, 287 (2009), 0908.2589.

[70] A. Djouadi, G. Moreau, F. Richard, and R. K. Singh (2009), 0906.0604.

[71] R. Contino and G. Servant, JHEP **06**, 026 (2008), 0801.1679.

[72] R. K. Ellis, W. J. Stirling, and B. R. Webber, vol. 8 (Cambridge University Press, 1996).

[73] P. Nason, S. Dawson, and R. Ellis, Nucl.Phys. **B303**, 607 (1988).

[74] W. Beenakker, H. Kuijf, W. L. van Neerven, and J. Smith, Phys. Rev. **D40**, 54 (1989).

[75] M. Cacciari, M. Czakon, M. L. Mangano, A. Mitov, and P. Nason (2011), 1111.5869.

[76] A. Martin, W. Stirling, R. Thorne, and G. Watt, Eur.Phys.J. **C63**, 189 (2009), 0901.0002.

[77] R. D. Ball et al. (The NNPDF Collaboration), Nucl.Phys. **B855**, 153 (2012), 1107.2652.

[78] N. Kidonakis, Phys.Rev. **D82**, 114030 (2010), 1009.4935.

[79] M. Cacciari, S. Frixione, M. L. Mangano, P. Nason, and G. Ridolfi, JHEP **09**, 127 (2008), 0804.2800.

[80] N. Kidonakis, E. Laenen, S. Moch, and R. Vogt, Phys.Rev. **D64**, 114001 (2001), hep-ph/0105041.

[81] R. Bonciani, S. Catani, M. L. Mangano, and P. Nason, Nucl.Phys. **B529**, 424 (1998), hep-ph/9801375.

[82] V. Ahrens, A. Ferroglia, M. Neubert, B. D. Pecjak, and L. L. Yang, JHEP **1009**, 097 (2010a), 1003.5827.

[83] M. Aliev, H. Lacker, U. Langenfeld, S. Moch, P. Uwer, et al., Comput.Phys.Commun. **182**, 1034 (2011), 1007.1327.

[84] V. Ahrens, M. Neubert, B. D. Pecjak, A. Ferroglia, and L. L. Yang, Phys.Lett. **B703**, 135 (2011a), 1105.5824.

[85] N. Kidonakis and B. D. Pecjak, Eur.Phys.J.C (2011), 1108.6063.

[86] R. Frederix and F. Maltoni, JHEP **01**, 047 (2009), 0712.2355.

[87] V. Abazov et al. (D0 Collaboration), Phys.Lett. **B626**, 55 (2005b), hep-ex/0505082.

[88] V. Abazov et al. (D0 Collaboration), Phys.Rev. **D76**, 052006 (2007a), 0706.0458.

[89] V. M. Abazov et al. (D0), Phys. Lett. **B679**, 177 (2009a), 0901.2137.

[90] V. M. Abazov et al. (D0 Collaboration), Phys.Lett. **B704**, 403 (2011a), 1105.5384.

[91] V. D. Barger, J. Ohnemus, and R. Phillips, Phys.Rev. **D48**, 3953 (1993), hep-ph/9308216.

[92] P. Sinervo (2003), prepared for PHYSTAT2003 : Statistical Problems in Particle Physics, Astrophysics, and Cosmology, Menlo Park, California, 8-11 Sep 2003.

[93] V. Abazov et al. (The D0 Collaboration), Nucl.Instrum.Meth. **A620**, 490 (2010), 1002.4224.

[94] T. Aaltonen et al. (CDF), Phys. Rev. Lett. **105**, 012001 (2010), 1004.3224.

[95] L. Lyons, D. Gibaut, and P. Clifford, Nucl. Instrum. Meth. **A270**, 110 (1988).

[96] A. Valassi, Nucl. Instrum. Meth. **A500**, 391 (2003).

[97] N. Cabibbo, Phys.Rev.Lett. **10**, 531 (1963).

[98] M. Kobayashi and T. Maskawa, Prog.Theor.Phys. **49**, 652 (1973).

[99] V. Abazov et al. (D0 Collaboration), Phys.Rev.Lett. **107**, 121802 (2011b), 1106.5436.

[100] G. J. Feldman and R. D. Cousins, Phys. Rev. **D57**, 3873 (1998), physics/9711021.

[101] V. M. Abazov et al. (D0), Phys. Rev. **D80**, 071102 (2009b), 0903.5525.

[102] V. M. Abazov et al. (D0), Phys. Lett. **B682**, 278 (2009c), 0908.1811.

[103] A. Abulencia et al. (CDF), Phys. Rev. Lett. **96**, 042003 (2006a), hep-ex/0510065.

[104] H. Flächer et al. (Gfitter), Eur.Phys.J. **C60**, 593 (2009), see also http ://gfitter.desy.de/, 0811.0009.

[105] G. L. Kane and S. Mrenna, Phys. Rev. Lett. **77**, 3502 (1996), hep-ph/9605351.

[106] F. Fiedler (2010), habilitation thesis at Munich University, 1003.0521.

[107] A. B. Galtieri, F. Margaroli, and I. Volobouev (CDF and D0 Collaboration) (2011), 1109.2163.

[108] I. I. Y. Bigi, M. A. Shifman, N. G. Uraltsev, and A. I. Vainshtein, Phys. Rev. **D50**, 2234 (1994), hep-ph/9402360.

[109] M. Beneke and V. M. Braun, Nucl. Phys. **B426**, 301 (1994), hep-ph/9402364.

[110] M. C. Smith and S. S. Willenbrock, Phys. Rev. Lett. **79**, 3825 (1997), hep-ph/9612329.

[111] M. Beneke, Phys.Rept. **317**, 1 (1999), hep-ph/9807443.

[112] W. A. Bardeen, A. J. Buras, D. W. Duke, and T. Muta, Phys. Rev. **D18**, 3998 (1978).

[113] A. H. Hoang and I. W. Stewart, Nucl. Phys. Proc. Suppl. **185**, 220 (2008), 0808.0222.

[114] A. Buckley, J. Butterworth, S. Gieseke, D. Grellscheid, S. Hoche, et al., Phys.Rept. **504**, 145 (2011), 1101.2599.

[115] A. H. Hoang, A. Jain, I. Scimemi, and I. W. Stewart, Phys.Rev.Lett. **101**, 151602 (2008), 0803.4214.

[116] A. Abulencia et al. (CDF), Phys. Rev. **D73**, 112006 (2006b), hep-ex/0602008.

[117] T. Aaltonen et al. (CDF), Phys. Rev. **D79**, 072005 (2009a), 0901.3773.

[118] V. M. Abazov et al. (D0), Phys. Rev. **D80**, 092006 (2009d), 0904.3195.

[119] R. H. Dalitz and G. R. Goldstein, Phys. Rev. **D45**, 1531 (1992).

[120] T. Aaltonen et al. (CDF Collaboration), Phys.Rev. **D83**, 111101 (2011a), 1105.0192.

[121] D. W. Scott (Wiley-Interscience, 1992).

[122] B. W. Silverman (Chapman and Hall, 1998).

[123] C. Loader (Springer, 1999).

[124] R. H. Dalitz and G. R. Goldstein, Proc. Roy. Soc. Lond. **A455**, 2803 (1999), hep-ph/9802249.

[125] K. Kondo, T. Chikamatsu, and S. H. Kim, J. Phys. Soc. Jap. **62**, 1177 (1993).

[126] F. A. Berends, C. G. Papadopoulos, and R. Pittau, Phys. Lett. **B417**, 385 (1998), hep-ph/9709257.

[127] P. Abreu et al. (DELPHI), Eur. Phys. J. **C2**, 581 (1998).

[128] A. Juste (1999), CERN-THESIS-99-012.

[129] V. M. Abazov et al. (D0), Nature **429**, 638 (2004), hep-ex/0406031.

[130] F. Fiedler, A. Grohsjean, P. Haefner, and P. Schieferdecker (2010), 1003.1316.

[131] G. Mahlon and S. J. Parke, Phys. Lett. **B411**, 173 (1997), hep-ph/9706304.

[132] T. Aaltonen et al. (CDF Collaboration), Phys.Rev. **D84**, 071105 (2011b), 1108.1601.

[133] V. M. Abazov et al. (The D0 Collaboration), Phys.Rev. **D84**, 032004 (2011c), 1105.6287.

[134] T. Aaltonen et al. (CDF), Phys. Rev. Lett. **102**, 152001 (2009b), 0807.4652.

[135] V. M. Abazov et al. (D0 Collaboration), Phys.Rev.Lett. **107**, 082004 (2011d), 1105.0320.

[136] F. A. Berends, H. Kuijf, B. Tausk, and W. Giele, Nucl.Phys. **B357**, 32 (1991).

[137] V. Abazov et al. (D0 Collaboration), Phys.Rev.Lett. **101**, 062001 (2008a), 0802.2400.

[138] M. Lancaster (Tevatron Electroweak Working Group, for the CDF and D0 Collaborations) (2011), 1107.5255.

[139] V. M. Abazov et al. (D0), Phys. Rev. **D75**, 092001 (2007b), hep-ex/0702018.

[140] T. Aaltonen et al. (CDF), Phys. Rev. Lett. **98**, 142001 (2007), hep-ex/0612026.

[141] V. Abazov et al. (D0 Collaboration), Phys.Rev.Lett. **100**, 192004 (2008b), 0803.2779.

[142] V. M. Abazov et al. (D0 Collaboration), Phys.Lett. **B703**, 422 (2011e), 1104.2887.

[143] V. M. Abazov et al. (D0 Collaboration), Phys.Rev. **D84**, 012008 (2011f), 1101.0124.

[144] P. M. Nadolsky et al., Phys. Rev. **D78**, 013004 (2008), 0802.0007.

[145] M. Cacciari, S. Frixione, M. Mangano, P. Nason, and G. Ridolfi, JHEP **0404**, 068 (2004), hep-ph/0303085.

[146] V. Ahrens, A. Ferroglia, M. Neubert, B. Pecjak, and L. Yang, Nucl.Phys.Proc.Suppl. **205-206**, 48 (2010b), 1006.4682.

[147] U. Langenfeld, S. Moch, and P. Uwer, Phys. Rev. **D80**, 054009 (2009), 0906.5273.

[148] N. Gray, D. J. Broadhurst, W. Grafe, and K. Schilcher, Z.Phys. **C48**, 673 (1990).

[149] K. Melnikov and T. v. Ritbergen, Phys.Lett. **B482**, 99 (2000), hep-ph/9912391.

[150] S. Bethke, Eur.Phys.J. **C64**, 689 (2009), 0908.1135.

[151] J. H. Kuhn and G. Rodrigo, Phys. Rev. **D59**, 054017 (1999), hep-ph/9807420.

[152] J. H. Kuhn and G. Rodrigo, Phys. Rev. Lett. **81**, 49 (1998), hep-ph/9802268.

[153] W. Bernreuther and Z.-G. Si (2010), 1003.3926.

[154] V. Ahrens, A. Ferroglia, M. Neubert, B. D. Pecjak, and L. L. Yang, Phys. Rev. **D84**, 074004 (2011b), 1106.6051.

[155] W. Hollik and D. Pagani (2011), 1107.2606.

[156] O. Antunano, J. H. Kuhn, and G. Rodrigo, Phys. Rev. **D77**, 014003 (2008), 0709.1652.

[157] N. Kidonakis, Phys.Rev. **D84**, 011504 (2011), 1105.5167.

[158] J. H. Kuhn and G. Rodrigo (2011), 1109.6830.

[159] T. Aaltonen et al. (CDF Collaboration), Phys.Rev. **D83**, 112003 (2011c), 1101.0034.

[160] V. M. Abazov et al. (D0 Collaboration) (2011g), 1107.4995.

[161] S. Frixione and B. Webber, JHEP **0206**, 029 (2002), see also http ://www.hep.phy.cam.ac.uk/theory/webber/MCatNLO/, 0204244.

[162] S. Chatrchyan et al. (CMS Collaboration) (2011), 1112.5100.

[163] P. Ferrario and G. Rodrigo, Phys. Rev. **D80**, 051701 (2009), 0906.5541.

[164] P. H. Frampton, J. Shu, and K. Wang, Phys. Lett. **B683**, 294 (2010), 0911.2955.

[165] S. Jung, H. Murayama, A. Pierce, and J. D. Wells, Phys.Rev. **D81**, 015004 (2010), 0907.4112.

[166] I. Dorsner, S. Fajfer, J. F. Kamenik, and N. Kosnik, Phys. Rev. **D81**, 055009 (2010), 0912.0972.

[167] B. Grinstein, A. L. Kagan, M. Trott, and J. Zupan, Phys. Rev. Lett. **107**, 012002 (2011), 1102.3374.

[168] Z. Ligeti, G. M. Tavares, and M. Schmaltz, JHEP **06**, 109 (2011), 1103.2757.

[169] S. Jung, A. Pierce, and J. D. Wells, Phys. Rev. **D83**, 114039 (2011), 1103.4835.

[170] J. A. Aguilar-Saavedra and M. Perez-Victoria, JHEP **05**, 034 (2011a), 1103.2765.

[171] J. A. Aguilar-Saavedra and M. Perez-Victoria (2011b), 1105.4606.

[172] S. Westhoff (2011), 1108.3341.

[173] P. H. Frampton and S. L. Glashow, Phys.Lett. **B190**, 157 (1987).

[174] J. Aguilar-Saavedra and M. Perez-Victoria, JHEP **1109**, 097 (2011c), 1107.0841.

[175] J. Aguilar-Saavedra and M. Perez-Victoria, Phys.Lett. **B705**, 228 (2011d), 1107.2120.

[176] J. L. Hewett, J. Shelton, M. Spannowsky, T. M. Tait, and M. Takeuchi, Phys.Rev. **D84**, 054005 (2011), 1103.4618.

[177] J.-F. Arguin, M. Freytsis, and Z. Ligeti, Phys.Rev. **D84**, 071504 (2011), 1107.4090.

[178] J. Aguilar-Saavedra, A. Juste, and F. Rubbo (2011), 1109.3710.

[179] D. Krohn, T. Liu, J. Shelton, and L.-T. Wang, Phys.Rev. **D84**, 074034 (2011), 1105.3743.

[180] E. L. Berger, Q.-H. Cao, C.-R. Chen, J.-H. Yu, and H. Zhang (2011), 1111.3641.

[181] A. Falkowski, G. Perez, and M. Schmaltz (2011), 1110.3796.